Università degli Studi di Salerno

DIPARTIMENTO DI FISICA "E.R. CAIANIELLO"

DOCTOR OF PHILOSOPHY IN PHYSICS

XIV CICLO, II SERIE

Exotic $(1/r^n)$ binary gravitational lenses

CHIARA MELCHIORRE

SUPERVISOR
DR. VALERIO BOZZA

COORDINATOR
PROF. CANIO NOCE

2013/2015

"E quindi uscimmo a riveder le stelle."
Dante Alighieri
Divina Commedia
Inferno - Canto XXXIV, 139

To my family

Contents

Introduction

A variety of observations suggests that the present universe is dominated by some unknown components. The distribution and properties of these components are the focus of modern cosmology and we are only beginning to understand them. Gravitational lensing, the bending of light in the gravitational field of a massive object, is one of the predictions of the general theory of relativity. Especially with recent and coming advances in observational data, the gravitational lensing is regarded as one of the most effective tools for probing a number of interesting phenomena of the universe. Some of these phenomena are the existence of various astrophysical objects like black holes, super-dense neutron stars, exotic matter, wormholes, naked singularities etc. The detection of these objects may eventually shed light on the possible connection between the quantum theory and gravity. Inspired by the latest result in the Sloan Digital Sky Survey Quasar Lens Search (SQLS) there are a lot of theoretical works concerning exotic objects. With some violation of the energy conditions, it is possible to combine scalar fields or other types of matter so as to build metrics that fall as $1/r^n$ asymptotically. This thesis aims at exploiting the existing gravitational lensing theory for non-Schwarzschild metrics to study a lensing system composed of two objects whose gravitational potential asymptotically falls as $1/r^n$, whether ordinary ($n < 1$) or exotic ($n > 1$).

Plan of Thesis

The light bending is of theoretical importance, in particular for studying the null structure of a spacetime. Starting from the Schwarzschild solution of Einstein's field equations that describes the geometry of space-time outside a spherically symmetric matter distribution, in Chapter 1 are shown other solutions able to represent physical particles in pure geometrical terms of spacetime. These solutions should be singularity-free, in order to avoid the divergence problem of particles in classical field theory. This Chapter provides a characterization of traversable wormholes and exotic objects describ-

ing furthermore the implication of non-Schwarzschild metric from the point of view of the energy-momentum tensor. A brief historical introduction to the regimes of gravitational lensing (microlensing, weak lensing and strong lensing) and the basic concepts are presented in Chapter 2. The deflection of light by massive bodies gives rise to many interesting phenomena that can modify how the sources of radiation are seen by an observer. In addition to magnifying the source, gravitational lensing amplifies the luminosity of the source, enabling the observation of objects too distant or intrinsically too faint to be observed without lensing. In the following chapters we discuss gravitational lensing effects by metrics falling as $1/r^n$. We need to distinguish two regimes, depending on whether n is smaller or larger than 1. The first case corresponds to galactic haloes, and the second case to exotic objects violating energy conditions. Chapter 3 describes some interesting results on the physical problem of gravitational lensing by this kind of metrics, in particular linked to the defocusing effect. What is asserted allows us to think that gravitational demagnification of light occurs because modified lenses could act as an effectively negative mass on a particular light ray. Then, a gravitational demagnification of light might be used for hunting a clue of exotic matter and energy. Chapter 4 introduces the binary lens equation for $1/r^n$ objects and investigates the properties of critical curves and caustics of this lens in all ranges of parameters. Main results with suggestions for further research are contained in the conclusions.

Chapter 1

From Schwarzschild to exotic metrics

1.1 The Schwarzschild solution

In 1916 Karl Schwarzschild discovered the first exact solution of Einstein's field equations [1]. This solution describes the geometry of space-time outside a spherically symmetric matter distribution. The most general spherically symmetric metric is

$$ds^2 = \alpha(r,t)dt^2 - \beta(r,t)dr^2 - \gamma(r,t)d\Omega^2 - \delta(r,t)drdt \tag{1.1}$$

where $d\Omega^2 = d\theta^2 + sin^2\theta d\phi^2$. We are using spherical polar coordinates. This metric is isotropic, therefore invariant under rotations. The invariance group of general relativity is formed by the group of general transformations of coordinates of the form $x'^{\mu} = f^{\mu}(x)$. This yields four degrees of freedom. Two of these degrees have been used when adopting spherical coordinates. The trasformations that do not break the central symmetry are $r' = f_1(r,t)$ and $t' = f_2(r,t)$. With the two available degrees of freedom, we can choose two metric coefficients. The other two are determined by Einstein's equations. Some possibilities are

Standard gauge

$$ds^2 = c^2A(r,t)dt^2 - B(r,t)dr^2 - r^2d\Omega^2$$

Synchronous gauge

$$ds^2 = c^2dt^2 - F^2(r,t)dr^2 - R^2d\Omega^2$$

Isotropic gauge

$$ds^2 = c^2 H^2(r,t)dt^2 - K^2(r,t)\left[dr^2 + r^2(r,t)d\Omega^2\right]$$

Adopting a static configuration, that means a no dependence of the metric coefficients on t, and the standard gauge, we can get equations for the coefficients A and B of the standard metric

$$ds^2 = c^2 A(r)dt^2 - B(r)dr^2 - r^2 d\Omega^2 \tag{1.2}$$

Since we are interested in the solution outside the spherical mass distribution, we only need to require the Ricci tensor to vanish: $R_{\mu\nu} = 0$. According to the definition of the curvature tensor and the Ricci tensor, we have

$$R_{\mu\nu} = \partial_\nu \Gamma^\sigma_{\mu\sigma} - \partial_\sigma \Gamma^\sigma_{\mu\nu} + \Gamma^\rho_{\mu\sigma}\Gamma^\sigma_{\rho\nu} - \Gamma^\rho_{\mu\nu}\Gamma^\sigma_{\rho\sigma} = 0$$

and the affine connection depends on the metric as

$$\Gamma^\sigma_{\mu\nu} = \frac{1}{2} g^{\rho\sigma}(\partial_\nu g_{\rho\mu} + \partial_\mu g_{\rho\nu} - \partial_\rho g_{\mu\nu})$$

We have to solve a set of differential equations for the components of the metric $g_{\mu\nu}$. The metric coefficients are

$$\begin{aligned}
g_{00} &= A(r) \\
g_{11} &= -B(r) \\
g_{22} &= -r^2 \\
g_{33} &= -r^2 sin^2\theta \\
g^{00} &= 1/A(r) \\
g^{11} &= -1/B(r) \\
g^{22} &= -1/r^2 \\
g^{33} &= -1/r^2 sin^2\theta
\end{aligned}$$

Only 9 of the 40 independent connection coefficients are different from zero and they are

$$\begin{aligned}
\Gamma^1_{01} &= A'/(2A) \\
\Gamma^1_{22} &= -r/B \\
\Gamma^2_{33} &= -sin\theta cos\theta \\
\Gamma^1_{00} &= A'/(2B) \\
\Gamma^1_{33} &= -(rsin^2\theta/B) \\
\Gamma^3_{13} &= 1/r \\
\Gamma^1_{11} &= B'/(2B) \\
\Gamma^2_{12} &= 1/r \\
\Gamma^3_{23} &= cot\theta
\end{aligned}$$

Replacing in the expression for $R_{\mu\nu}$:

$$\begin{aligned}
R_{00} &= -\frac{A''}{2B} + \frac{A'}{4B}\left(\frac{A'}{A} + \frac{B'}{B}\right) - \frac{A'}{rB} \\
R_{11} &= \frac{A''}{2A} - \frac{A'}{4A}\left(\frac{A'}{A} + \frac{B'}{B}\right) - \frac{B'}{rB} \\
R_{22} &= \frac{1}{B} - 1 + \frac{r}{2B}\left(\frac{A'}{A} - \frac{B'}{B}\right) \\
R_{33} &= R_{22}sin^2\theta
\end{aligned}$$

For the region of empty space, Einstein's field equations become

$$R_{00} = R_{11} = R_{22} = 0$$

and the fourth equation has no additional information. Multiplying the first equation by B/A and adding the result to the second equation we get

$$A'B + AB' = 0$$

from which $AB = constant$. We can write $B = \alpha A^{-1}$. Going to the third equation and replacing B we obtain $A + rA' = \alpha$ or

$$\frac{d(rA)}{dr} = \alpha$$

The solution of this equation is

$$A(r) = \alpha\left(1 + \frac{k}{r}\right)$$

with k another integration constant.
For B we obtain

$$B(r) = \left(1 + \frac{k}{r}\right)^{-1}$$

Now we consider the Newtonian limit

$$\frac{A(r)}{c^2} = 1 + \frac{2\Phi}{c^2}$$

with $\Phi = -GM/r$ the Newtonian gravitational potential. We conclude that $k = -2GM/c^2$ and $\alpha = c^2$.
The Schwarzschild solution for a static mass M can be written in spherical coordinates (t, r, θ, ϕ) as:

$$ds^2 = \left(1 - \frac{2GM}{rc^2}\right) c^2 dt^2 - \left(1 - \frac{2GM}{rc^2}\right)^{-1} dr^2 - r^2(d\theta^2 + sin^2\theta d\phi^2) \quad (1.3)$$

This solution corresponds to the vacuum region exterior to the spherical object of mass M. Inside the object, space-time will depend on the peculiarities of the physical object. Now we analyze the properties of this metric. We assume that the mass M is concentrated at $r = 0$. There are two singularities at which the metric diverges, one at $r = 0$ and the other at $r = r_s$, the *Schwarzschild radius*

$$r_s = \frac{2GM}{c^2}$$

For a point mass, the Schwarzschild radius is in the vacuum region and space-time has the structure given by Eq. (1.3). In general, we can write

$$r_s \sim 3\frac{M}{M_\odot} Km$$

Some interesting things occur close to the Schwarzschild radius.

For the proper time we get

$$d\tau = \left(1 - \frac{2GM}{rc^2}\right)^{1/2} dt \quad (1.4)$$

or

$$dt = \left(1 - \frac{2GM}{rc^2}\right)^{-1/2} d\tau \quad (1.5)$$

When $r \to \infty$, t is interpreted as the proper time measured from an infinite distance. As the system with proper time τ approaches to r_s, dt tends to

infinity according to Eq. (1.5). The object never reaches the Schwarzschild surface when seen by an infinitely distant observer. The closer the object is to the Schwarzschild radius, the slower it moves for the external observer.

A direct consequence of the difference introduced by gravity in the local time with respect to the time at infinity is that the radiation that escapes from a given radius $r > r_s$ will be redshifted when received by a distant and static observer. Since the frequency, and hence the energy of the photon depends on the time interval, we can write, from Eq. (1.5)

$$\lambda_\infty = \left(1 - \frac{2GM}{rc^2}\right)^{-1/2} \lambda \tag{1.6}$$

But, since the redshift is

$$z = \frac{\lambda_\infty - \lambda}{\lambda} \tag{1.7}$$

then

$$1 + z = \left(1 - \frac{2GM}{rc^2}\right)^{-1/2} \tag{1.8}$$

As we see, when $r \to r_s$ the redshift becomes infinite. A photon needs infinite energy to escape from inside the region determined by the Schwarzschild radius. Events that occur at $r < r_s$ are disconnected from the rest of the universe. We call the surface determined by $r = r_s$ an *event horizon*. Whatever crosses the event horizon will never return. This is the origin of the expression *black hole*, introduced by John A. Wheeler in the mid 1960s. The black hole is the region of space-time inside the event horizon. We can see in Figure 1.1 what happens with the light cones as an event is closer to the horizon of a Schwarzschild black hole. The shape of the cones can be calculated from the metric (1.3) imposing the null condition $ds^2 = 0$. Then

$$\frac{dr}{dt} = \pm \left(1 - \frac{2GM}{r}\right) \tag{1.9}$$

with c = 1. Notice that when $r \to \infty$, $dr/dt \to \pm 1$, as in Minkowski space-time. When $r \to 2GM$, $dr/dt \to 0$, and light moves along the surface $r = 2GM$, which is consequently a null surface. For $r < 2GM$, the sign of the derivative is inverted. The inward region of $r = 2GM$ is time-like for any physical system that has crossed the boundary surface.

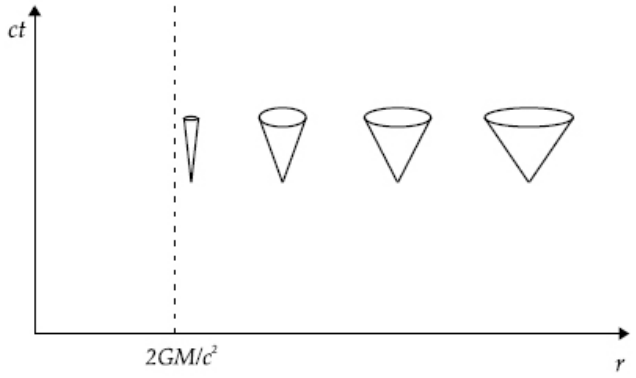

Figure 1.1: Space-time diagram in Schwarzschild coordinates showing the light cones of events at different distances from the event horizon.

1.2 Birkhoff's Theorem

If we consider the isotropic but not static line element

$$ds^2 = c^2 A(r,t)dt^2 - B(r,t)dr^2 - r^2 d\Omega^2$$

and substitute it into Einstein's empty-space field equations $R_{\mu\nu} = 0$ to obtain the functions $A(r,t)$ and $B(r,t)$, the result would be exactly the same

$$A(r,t) = A(r) = \left(1 - \frac{2GM}{rc^2}\right)$$
$$B(r,t) = B(r) = \left(1 - \frac{2GM}{rc^2}\right)^{-1}$$

This result is known as Birkhoff's theorem:

The space-time geometry outside a general spherically symmetric matter distribution is the Schwarzschild geometry.

Birkhoff's theorem implies that strictly radial motions do not perturb the spacetime metric. In particular, a pulsating star, if the pulsations are strictly radial, do not produce gravitational waves. The converse of Birkhoff's theorem is not true. If the region of space-time is described by the metric given by expression (1.3), then the matter distribution that is the source of the metric does not need to be spherically symmetric [2].

1.3 Wormholes and exotic objects

The first paper on wormhole solutions of Einstein's field equations was published in 1935 by Einstein himself and Nathan Rosen [3]. Einstein and Rosen used the word "bridge" to describe their solution. They were looking for solutions able to represent physical particles in pure geometrical terms of spacetime. These solutions should be singularity-free, in order to avoid the divergence problem of particles in classical field theory.
A wormhole is a region of space-time with non-trivial topology. It has two mouths connected by a throat. The mouths are not hidden by event horizons and there is no singularity to avoid the passage of particles, or travelers, from one side to the other. Wormholes are holes in space-time, i.e. their existence implies a multiple-connected space-time. There are many types of wormhole solutions of Einstein's field equations. Now we see the desired properties of traversable wormholes and a general metric for the wormhole as shown by Morris and Thorne in 1988 [4]:

(1) *The metric should be both spherically symmetric and static (time indipendent).*

(2) *The solution must everywhere obey the Einstein field equations.*

(3) *To be a wormhole the solution must have a throat that connects two asymptotically flat regions of spacetime; i.e., an equatorial embedding diagram must have qualitatively the form of Figure 1.2.*

(4) *There should be no horizon, since a horizon, if present, would prevent two-way travel through the wormhole.*

(5) *The tidal gravitational forces experienced by a traveler must be bearably small.*

(6) *A traveler must be able to cross through the wormhole in a finite and reasonably small proper time (e.g., less than a year) as measured not only by herself, but also by observers who remain behind or who await her outside the wormhole.*

(7) *The matter and fields that generate the wormhole's spacetime curvature must have a physically reasonable stress-energy tensor.*

(8) *The solution should be perturbatively stable(especially as a spaceship passes through).*

(9) *It should be possible to assemble the wormhole. For instance, the assembly should require both much less than the mass of the universe and much less than the age of the universe.*

The starting ansatz for the wormhole metric is

$$ds^2 = -e^{2\Phi}c^2dt^2 + \frac{dr^2}{1-b/r} + r^2(d\theta^2 + sin^2\theta d\phi^2) \tag{1.10}$$

where $\Phi = \Phi(r)$ is the *redshift function* and $b = b(r)$ is the *shape function*. The metric is spherically simmetric and static. When imposing condition that the metric must satisfy Einstein equations in every point of spacetime, we obtain the relation between the functions $\Phi(r)$, $b(r)$ and the stress-energy tensor that produces the wormhole spacetime geometry. Outside the wormhole, the spacetime is considered asymptotically flat and has a line element given by Schwarzschild metric (Eq. (1.3)). The junction conditions that follow from the theory of general relativity are the continuity of the metric components and the extrinsic curvature across the surface of juncture. To obtain specific solutions, in wormhole studies it is usual to fix a spacetime geometry and then use the Einstein equations to derive the matter distribution needed to obtain the respective metric. The embedding diagram (an embedding is an immersion of a given manifold into a manifold of lower dimensionality that preserves the metric properties) for this metric is given in Figure 1.2. In contrast to the Schwarzschild metric, which is time-dependent inside the horizon, the wormhole metric is static everywhere. Thus the embedding diagram gives the properties at all times. An observer can travel throught the trhoat and emerge at the other side in a finite time. The spacetime has no horizon: a radial light ray can always escape to infinity. There are two region where the curvature tends to zero at large distances from the wormhole. There is no restriction on travel between the two regions. In theory, we can join spacetime creating a shorter route through the wormhole, how we can see in Figure 1.2(b). Notice that the radial coordinate r has special geometric significance: $2\pi r$ is the circumference of a circle centered on the wormhole's throath, and thus r is equal to the embedding-space radial coordinate. A spacetime of special interest has the form

$$ds^2 = -c^2dt^2 + dl^2 + (b_0^2 + l^2)(d\theta^2 + sin^2\theta d\phi^2) \tag{1.11}$$

where the coordinates have the ranges $-\infty < t < +\infty$, $-\infty < l < +\infty$, $0 \leq \theta \leq \pi$, $0 \leq \phi \leq 2\pi$ and b_0 is a constant. In this case the functions $\Phi(r)$

and $b(r)$ are $\Phi = 0$, $b = b_0^2/r$. In this specific wormhole solution, the radial coordiante l is related to r by

$$l = \pm(r^2 - b_0^2)^{1/2} \tag{1.12}$$

with + in the upper universe and − in the lower.

Then, r is non-monotonic:

- decreases from $+\infty$ to a minimum value, b_0, as one moves through the lower universe of Figure 1.2 toward the wormhole and into the throath,

- increases from b_0 back to $+\infty$ as one moves out of the throath and into the upper universe.

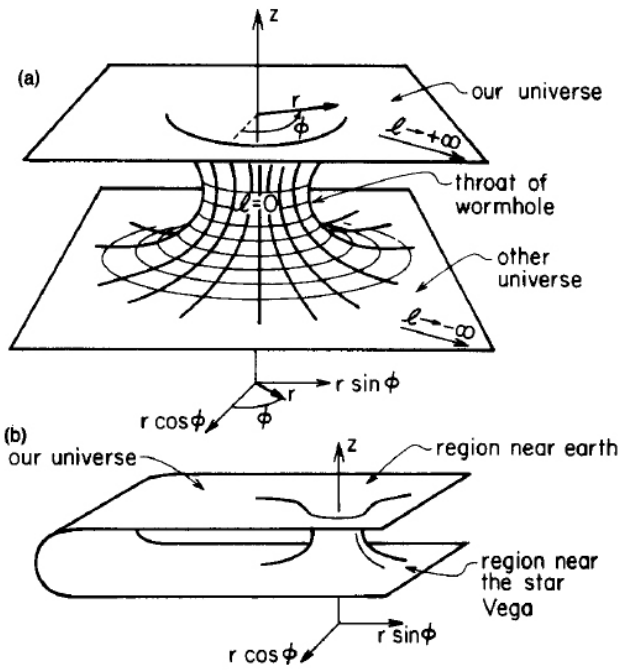

Figure 1.2: (a) Embedding diagram for a wormhole that connects two different universes. (b) Embedding diagram for a wormhole that connects two distant regions of our universe. Each diagram depicts the geometry of an equatorial ($\theta = \pi/2$) slice through space at a specific moment of time ($t = const$). M. S. Morris and K. S. Thorne [4].

The geometry of three-dimensional space at a fixed moment of time is very interesting. Since geometry is spherically simmetric, we can confine attention to an equatorial slice $\theta = \pi/2$, without significant loss of information.
The line element is obtained by setting $t = const$, $\theta = \pi/2$ in Eq. (1.10)

$$ds^2 = \frac{dr^2}{1 - b/r} + r^2 d\phi^2 \tag{1.13}$$

We wish to visualize this slice as removed from spacetime and embedded in Euclidean space. We introduce cylindrical coordinates z, r and ϕ. The Euclidean metric of the embedding space has the form

$$ds^2 = dz^2 + dr^2 + r^2 d\phi^2 \tag{1.14}$$

The embedded surface is axially symmetric and can be described by the single function $z = z(r)$. On that surface, the line element is

$$ds^2 = \left[1 + \left(\frac{dz}{dr}\right)^2\right] dr^2 + r^2 d\phi^2 \tag{1.15}$$

This line element is the same as that of our equatorial slice through the wormhole (Eq. (1.13)) if we identify the coordinates of the embedding space (r, ϕ) with the (r, ϕ) of the wormhole's spacetime, and if we require that the function $z(r)$, which describes the embedded surface satisfy

$$\frac{dz}{dr} = \pm\left(\frac{r}{b(r)} - 1\right)^{-1/2} \tag{1.16}$$

The last equation describes how the function $b = b(r)$ shapes the wormhole's spatial geometry. The surface $z = z(r)$ is pictured in Figure 1.2 (a).

Every wormhole must have a minimus radius, the wormhole throat, $r = b_0$ at which its embedded surface is vertical. This means that the expression (1.16) is divergent and that $b(r) = r$. We denote the common value of r and b at this throat by b_0. There exists a minimum radius $r = b_0$ in the wormhole and at $r = b_0$, $b = b_0$. The radial coordinate r is bad behaved near the throat, but proper radial distance $l(r)$ must be well behaved everywhere

$$l(r) = \pm \int_{b_0}^{\tau} \frac{dr}{[1 - b(r)/r]^{1/2}} \tag{1.17}$$

We must require that $l(r)$ is finite throughout spacetime, which implies that $1 - b/r \geq 0$ throughout spacetime. As we said, far from the throat, in both radial directions, space must become asymptotically flat. From Eq. (1.16), $b/r \to 0$, as $l \to \pm\infty$. Equations (1.16) and (1.17) imply that for the embedded wormhole

$$\begin{aligned} \frac{dz}{dl} &= \pm\sqrt{\frac{b}{r}} \\ \frac{dr}{dl} &= \pm\sqrt{1 - \frac{b}{r}} \end{aligned} \tag{1.18}$$

Figure 1.3 depicts a general wormhole shape and the geometrical meaning of equations (1.18).

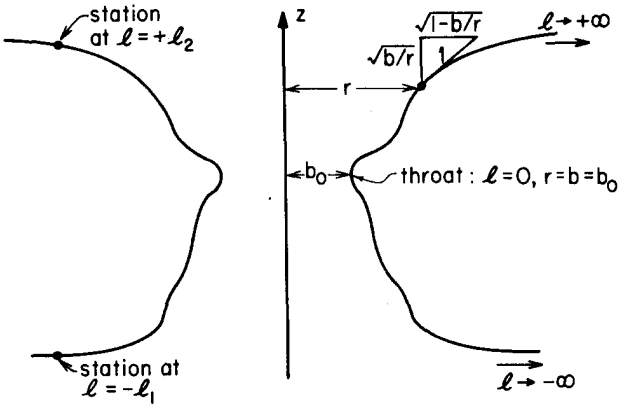

Figure 1.3: The embedding diagram for a general wormhole as seen in profile. The diagram must be rotated around the vertical axis z to make it complete (Figure 1.2). M. S. Morris and K. S. Thorne [4].

Our traversable wormholes do not posses any horizons. They are the physically nonsingular surfaces at which $g_{00} \equiv -e^{2\Phi} \to 0$, vanishing proper time lapse during any finite coordinate time.

1.4 Ellis wormhole

In 1973 Homer Ellis finds a way to force open the Schwarzschild singularity and then to connect on an additional chunk of space-time [5]. He replaces the singularity with a special hole, the *drainhole*.

"The rationale for this name is that on the space-time manifold containing the hole there is a vector field that can be interpreted as a velocity field for an "ether" draining through the hole. The existence of the hole permits this ether to be conserved in the sense that its streamlines, which are timelike geodesics, never abruptly terminate".

The hypothetical ether provides a universal system of inertial observers: every observer or test particle drifting with the ether, following its flow, is absolutely unaccelerated. The ether, pervading all of space-time, is more than a mere inert medium for the propagation of electromagnetic waves.
In this frame, mass particles appear as sinks or sources of this flowing ether.

The general line element takes the spherically symmetric form

$$\begin{aligned} d\tau^2 &= dt^2 - [d\rho - f(\rho)dt]^2 - r^2(\rho)[d\theta^2 + sin^2\theta d\varphi^2] \\ &= dt^2 - [d\rho - f(\rho)dt]^2 - r^2(\rho)d\Omega^2 \end{aligned} \tag{1.19}$$

in which the function f with domain A and the nonnegative function r with domain B are to be determined by the field equations. The coordinate ranges are supposed given by

$$-\infty < t < \infty, -\infty < \rho < \infty, 0 < \theta < \pi, -\pi < \varphi < \pi \tag{1.20}$$

and $\rho \in \mathrm{A} \cap \mathrm{B} - r^{-1}(0)$. Since $r^{-1}(0)$ is excluded from the range of ρ, the line element is regular for all values of the coordinates.
When the functions f and r have been specified, the line element may be considered to lie upon a manifold $\mathfrak{M}$. Note that the metric (1.19) is independent of t. This means that all translation of $\mathfrak{M}$ along the t curves are isometries. Now we consider the cross section of $\mathfrak{M}$ on which the time coordinate is constant: Σ_t. In Σ_t, the Riemannian line element is given by

$$d\sigma^2 = d\rho^2 + r^2(\rho)d\Omega^2 \tag{1.21}$$

If $r(\rho) = \rho$, the line element is of Euclidean 3-space E^3. An interesting case has $r(\rho) = (\rho^2 + n^2)^{1/2}$, where n is a positive constant and is the radius of the drainhole. The equatorial cross section of Σ_t is showed in Figure 1.4.

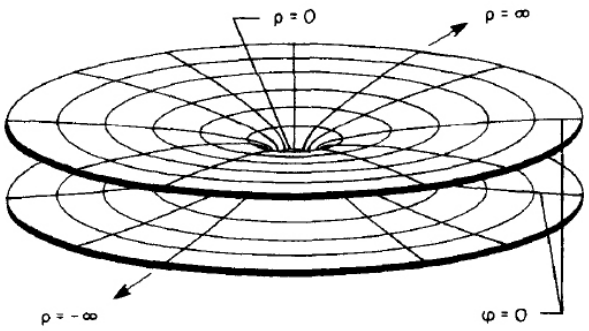

Figure 1.4: The equatorial cross section of the typical spatial cross section Σ_t of the space-time manifold $\mathfrak{M}$ in a special case. The line element of this surface is given by $d\sigma^2 = d\rho^2 + (\rho^2 + n^2)d\varphi^2$. The surface is isometric to the catenoid $\{[x, y, z]|(x^2 + y^2)^{1/2} = ncosh(z/n)\}$ in E^3. The radius of the central hole, where $\rho = 0$, is n. The surface is asymptotic to E^2, both as $\rho \to \infty$ and as $\rho \to -\infty$. H. G. Ellis [5].

It is isometrically embeddable as a catenoid in E^3

$$\{[x, y, z]|(x^2 + y^2)^{1/2} = ncosh(z/n)\} \tag{1.22}$$

The surface is asymptotic to E^2, both as $\rho \to \infty$ and as $\rho \to -\infty$. To open up the Schwarzschild singularity, Ellis introduces a device: a scalar field ϕ. This field satisfy the scalar wave equation

$$\Box\phi = 0 \tag{1.23}$$

and is coupled to the metric of the manifold through the field equations

$$R_{\mu\nu} = 2\phi_{,\mu}\phi_{,\nu} \tag{1.24}$$

If $\phi = \alpha(\rho)$, the wave equation (1.23) is equivalent to

$$[r^2(f^2 - 1)\alpha']' = 0 \tag{1.25}$$

and the field equations (1.24) are equivalent to

$$r''/r = \alpha'^2 \tag{1.26}$$

$$[r^2(f^2/2)']' = 0 \tag{1.27}$$

$$[(r^2/2)'(1 - f^2)]' = 1. \tag{1.28}$$

The equations (1.25)-(1.28) allow to obtain the following relations for r and α

$$r^2(\rho) = |\rho^2 + n^2 - m^2| e^{(2m/n)\alpha(\rho)} \tag{1.29}$$

$$\alpha' = -\frac{n}{\rho^2 + n^2 - m^2} \tag{1.30}$$

where n is nonnegative. Requiring the boundary condition

$$\lim_{\rho\to\infty} \phi \equiv \lim_{\rho\to\infty} \alpha(\rho) = 0 \tag{1.31}$$

the line element, re-written in an appropriate coordinate system, is asymptotic to a Schwarzchild vacuum line element with mass parameter m.
This boundary condition doesn't reduce the set of solution manifolds within isometric equivalence: it has no effect on α' and only α' appears in the field equations. In each manifold there is one side of the drainhole asymptotic to a Schwarzschild manifold with positive mass parameter m and the other side asymptotic to a Schwarzschild manifold with negative mass parameter $\overline{m}$. The two-sided particle attracts matter on the one side and repels it on the other. This model provides that $-\overline{m} > m$. The asymmetry between the positive and the negative mass is expressed by

$$\frac{\overline{m}}{m} = -exp\left[\frac{m\pi}{(n^2 - m^2)^{1/2}}\right] \tag{1.32}$$

e.g. if m is of the order of a proton mass $1.2\times10^{-52}cm$ and n is of the order of Planck's length $1.6\times10^{-33}cm$, then $-\overline{m}/m \sim 1+10^{-19}$. If n is of the order of the classical electron radius $\sim 2.8\times10^{-13}cm$, then $-\overline{m}/m \sim 1+10^{-39}$. The ratios of total scalar field energy to m in these cases are 10^{19} and 10^{39}. Here, the universe expands because it contains more negative mass than positive.

The first physicist that investigated the effects of negative mass was Sir Hermann Bondi in 1957 [6]. Bondi pointed out that when General Relativity is considered purely as a theory of gravity, mass never actually appears. It first appears when the equations are solved in a way devised by K. Schwartzschild. Then mass appears as a constant of integration. Bondi noticed that this mass constant could be made either positive or negative. He was able to show that when m is made negative, both the inertial and the gravitational mass effects are reversed. The results of Bondi's calculations can be summarized as follows: a positive mass attracts all nearby masses whether positive or negative; a negative mass repels all nearby masses whether positive or negative.

But, there is an interesting corollary of this result. Consider a pair of equal and opposite positive and a negative masses placed close to each other. The negative mass is attracted to the positive mass, while the positive mass is repelled by the negative mass. Thus the two masses will experience equal forces and accelerations in the same direction (in violation of Newton's third law) and the system of two particles will accelerate. The negative mass will chase the positive mass with constant acceleration. Bondi doesn't speak directly about the mass-energy of a negative mass, but the answer is implied by his calculations. A negative mass will have negative mass-energy. The net mass-energy of equal positive and negative masses will be zero.
Nowadays, negative mass provides a possible explanations for the dark energy, which has antigravity element and is considered as the source of the universe expansion and acceleration. It is also a valid explanation for dark matter that generates the additional effect of centripetal force on objects within galaxy and shows to become clustered outside galaxy.

1.5 The Stress-Energy Tensor

The search for the wormholes by studying the mirror images formed due to the gravitational lensing is one of the most charming ways to prove the existence of the exotic matter in nature. The idea that wormholes can act as gravitational lenses and induce a microlensing signature on a background source was first suggested by Kim and Cho [7]. Cramer et al. [8] carried out more detailed analysis of negative mass wormholes and considered the effects they can produce on background point sources, at non-cosmological distances. The generalization to a cosmological scenario was carried out by Torres et al. [9], although lensing of point sources was still used. The first and only bound on the possible existence of negative masses, imposed using astrophysical databases, was given by Torres et al. [10]. These authors showed that the effective gravitational repulsion of light rays from background gamma-ray emitting AGNs creates two bursts, which are individually asymmetric under time reversal. Then Anchordoqui et al. [11] searched in existent gamma-ray bursts databases for signatures of wormhole microlensing. Although they detected some interesting candidates, no conclusive results were obtained. Peculiarly asymmetric gamma-ray bursts (Romero et al. [12]), although highly uncommon, might be probably explained by more conventional hypothesis, like precessing jets.

Now we try to understand what kind of matter we need in order to create the curvature of the wormhole metric. First of all, we must derive the Einstein field equations. Then we calculate the Riemann and Einstein tensor for the metric (Eq. (1.10)). We rewrite the metric in the form

$$ds^2 = g_{\alpha\beta}dx^\alpha dx^\beta,\ x^0 = ct,\ x^1 = r,\ x^2 = \theta,\ x^3 = \phi \tag{1.33}$$

and we obtain the Christoffel symbols (connection coefficients) $\Gamma^\alpha_{\beta\gamma}$ and the components of the Riemann curvature tensor $R^\alpha_{\beta\gamma\delta}$ as

$$\Gamma^\alpha_{\beta\gamma} = \frac{1}{2}g^{\alpha\lambda}(g_{\lambda\beta,\gamma} + g_{\lambda\gamma,\beta} - g_{\beta\gamma,\lambda}) \tag{1.34}$$

$$R^\alpha_{\beta\gamma\delta} = \Gamma^\alpha_{\beta\delta,\gamma} - \Gamma^\alpha_{\beta\gamma,\delta} + \Gamma^\alpha_{\lambda\gamma}\Gamma^\lambda_{\beta\delta} - \Gamma^\alpha_{\lambda\delta}\Gamma^\lambda_{\beta\gamma} \tag{1.35}$$

where the comma denotes a partial derivative

$$g_{\alpha\beta,\gamma} = \frac{\partial g_{\alpha\beta}}{\partial x^\gamma} \tag{1.36}$$

The 24 nonzero components of the Riemann tensor are

$$\begin{aligned}
R^t_{rtr} &= -R^t_{rrt} = (1-b/r)^{-1}e^{-2\Phi}R^r_{ttr} \\
&= -(1-b/r)^{-1}e^{-2\Phi}R^r_{trt} \\
&= -\Phi'' + (b'r-b)[2r(r-b)]^{-1}\Phi' - (\Phi')^2, \\
R^t_{\theta t\theta} &= -R^t_{\theta\theta t} = r^2e^{-2\Phi}R^\theta_{tt\theta} = -r^2e^{-2\Phi}R^\theta_{t\theta t} \\
&= -r\Phi'(1-b/r), \\
R^t_{\phi t\phi} &= -R^t_{\phi\phi t} = r^2e^{-2\Phi}sin^2\theta R^\phi_{tt\phi} \\
&= -r^2e^{-2\Phi}sin^2\theta R^\phi_{t\phi t} \\
&= -r\Phi'(1-b/r)sin^2\theta, \\
R^r_{\theta r\theta} &= -R^r_{\theta\theta r} = -r^2(1-b/r)R^\theta_{rr\theta} \\
&= r^2(1-b/r)R^\theta_{r\theta r} \\
&= (b'r-b)/2r, \\
R^r_{\phi r\phi} &= -R^r_{\phi\phi r} = -r^2(1-b/r)sin^2\theta R^\phi_{rr\phi} \\
&= r^2(1-b/r)sin^2\theta R^\phi_{r\phi r} \\
&= (b'r-b)sin^2\theta/2r, \\
R^\theta_{\phi\theta\phi} &= -R^\theta_{\phi\phi\theta} = sin^2\theta R^\phi_{\theta\phi\theta} = -sin^2\theta R^\phi_{\theta\theta\phi} \\
&= (b/r)sin^2\theta.
\end{aligned}$$

Here, the prime denotes a derivative with respect to the radial coordinate r and the basis vector $(\mathbf{e}_t, \mathbf{e}_r, \mathbf{e}_\theta, \mathbf{e}_\phi)$ are associated with the coordinate system ct, r, θ, ϕ. The components of the Riemann tensor can be simplified by choosing the *proper reference frame*. In this frame a set of observers remains always at rest in the coordinate system (r, θ, ϕ constant)

$$\begin{aligned}\mathbf{e}_{\hat{t}} &= e^{-\Phi}\mathbf{e}_t, \mathbf{e}_{\hat{r}} = (1-b/r)^{1/2}\mathbf{e}_r,\\ \mathbf{e}_{\hat{\theta}} &= r^{-1}\mathbf{e}_\theta, \mathbf{e}_{\hat{\phi}} = (rsin\theta)^{-1}\mathbf{e}_\phi.\end{aligned}$$

The 24 nonzero components take the form

$$\begin{aligned}R^{\hat{t}}_{\hat{r}\hat{t}\hat{r}} &= -R^{\hat{t}}_{\hat{r}\hat{r}\hat{t}} = R^{\hat{r}}_{\hat{t}\hat{t}\hat{r}} = -R^{\hat{r}}_{\hat{t}\hat{r}\hat{t}}\\ &= (1-b/r)\{-\Phi'' + (b'r-b)[2r(r-b)]^{-1}\Phi' - (\Phi')^2\},\\ R^{\hat{t}}_{\hat{\theta}\hat{t}\hat{\theta}} &= -R^{\hat{t}}_{\hat{\theta}\hat{\theta}\hat{t}} = R^{\hat{\theta}}_{\hat{t}\hat{t}\hat{\theta}} = -R^{\hat{\theta}}_{\hat{t}\hat{\theta}\hat{t}} = -(1-b/r)\Phi'/r,\\ R^{\hat{t}}_{\hat{\phi}\hat{t}\hat{\phi}} &= -R^{\hat{t}}_{\hat{\phi}\hat{\phi}\hat{t}} = R^{\hat{\phi}}_{\hat{t}\hat{t}\hat{\phi}} = -R^{\hat{\phi}}_{\hat{t}\hat{\phi}\hat{t}} = -(1-b/r)\Phi'/r,\\ R^{\hat{r}}_{\hat{\theta}\hat{r}\hat{\theta}} &= -R^{\hat{r}}_{\hat{\theta}\hat{\theta}\hat{r}} = R^{\hat{\theta}}_{\hat{r}\hat{\theta}\hat{r}} = -R^{\hat{\theta}}_{\hat{r}\hat{r}\hat{\theta}} = (b'r-b)/2r^3,\\ R^{\hat{r}}_{\hat{\phi}\hat{r}\hat{\phi}} &= -R^{\hat{r}}_{\hat{\phi}\hat{\phi}\hat{r}} = R^{\hat{\phi}}_{\hat{r}\hat{\phi}\hat{r}} = -R^{\hat{\phi}}_{\hat{r}\hat{r}\hat{\phi}} = (b'r-b)/2r^3,\\ R^{\hat{\theta}}_{\hat{\phi}\hat{\theta}\hat{\phi}} &= -R^{\hat{\theta}}_{\hat{\phi}\hat{\phi}\hat{\theta}} = R^{\hat{\phi}}_{\hat{\theta}\hat{\phi}\hat{\theta}} = -R^{\hat{\phi}}_{\hat{\theta}\hat{\theta}\hat{\phi}} = b/r^3.\end{aligned}$$

Now we can contract the Riemann tensor to calculate the Ricci tensor $R_{\hat{\mu}\hat{\nu}}$ and the scalar curvature R from the standard formulas

$$\begin{aligned}R_{\hat{\mu}\hat{\nu}} &= R^{\hat{\alpha}}_{\hat{\mu}\hat{\alpha}\hat{\nu}}\\ R &= g^{\hat{\mu}\hat{\nu}}R_{\hat{\mu}\hat{\nu}}\end{aligned} \tag{1.37}$$

and we can compute the Einstein tensor that gets into the Einstein field equations

$$G_{\hat{\mu}\hat{\nu}} = R_{\hat{\mu}\hat{\nu}} - \frac{1}{2}Rg_{\hat{\mu}\hat{\nu}} \tag{1.38}$$

The nonzero components of the Einstein tensor are

$$\begin{aligned}&G_{\hat{t}\hat{t}} = b'/r^2,\\ &G_{\hat{r}\hat{r}} = -b/r^3 + 2(1-b/r)\Phi'/r,\\ &G_{\hat{\theta}\hat{\theta}} = G_{\hat{\phi}\hat{\phi}} = \left(1-\frac{b}{r}\right)\left(\Phi'' - \frac{b'r-b}{2r(r-b)}\Phi' + (\Phi')^2 + \frac{\Phi'}{r} - \frac{b'r-b}{2r^2(r-b)}\right).\end{aligned} \tag{1.39}$$

The stress-energy tensor is proportional to the Einstein Tensor. Then $T_{\hat{\mu}\hat{\nu}}$ must have the same algebraic structure as the $G_{\hat{\mu}\hat{\nu}}$ end the only nonzero

components must be

$$\begin{aligned} T_{\hat{t}\hat{t}} &= \rho(r)c^2 \\ T_{\hat{r}\hat{r}} &= -\tau(r) \\ T_{\hat{\theta}\hat{\theta}} &= T_{\hat{\phi}\hat{\phi}} = p(r) \end{aligned} \tag{1.40}$$

where $\rho(r)$ is the *total density of mass-energy*, $\tau(r)$ is the *tension* per unit area measured in the radial direction and $p(r)$ is the *pressure* measured in lateral directions (directions orthogonal to radial). An ordinary perfect fluid has a stress-energy tensor that is a special case of equations (1.40): $-\tau = p$.

The Einstein field equations

$$G_{\hat{\alpha}\hat{\beta}} = 8\pi G c^{-4} T_{\hat{\alpha}\hat{\beta}} \tag{1.41}$$

allow us to get three differential equations

$$b' = 8\pi G c^{-2} r^2 \rho \tag{1.42}$$

$$\Phi' = (-8\pi G c^{-4} \tau r^3 + b)/[2r(r-b)] \tag{1.43}$$

$$\tau' = (\rho c^2 - \tau)\Phi' - 2(p+\tau)/r \tag{1.44}$$

relating five unknown function of r: b, Φ, ρ, τ and p. To solve these equations, we would be to assume some specific type of matter or field for the source of stress-energy tensor. After that, we can derive from the physics of this source, the equations of state for the radial tension τ and for the lateral pressure p as a function of mass-energy density: $\tau = \tau(\rho)$, $p = p(\rho)$.
Now, we have five equations for five unknown functions of r: the last two plus the three field equations. Since we desire solutions with specific properties, we must let the relationships between ρ, τ, and p fixed by the field equations and we control the functions $b(r)$ and $\Phi(r)$. We can rewrite equations (1.42)-(1.44) in order to obtain ρ, τ and p with a suitable choice of b and Φ

$$\rho = b'/[8\pi G c^{-2} r^2] \tag{1.45}$$

$$\tau = [b/r - 2(r-b)\Phi']/[8\pi G c^{-4} r^2] \tag{1.46}$$

$$p = (r/2)[(\rho c^2 - \tau)\Phi' - \tau'] - \tau \tag{1.47}$$

Therefore, the constraints on the wormhole's shape function $b(r)$ produces constraints on the mass density ρ, radial tension τ and lateral pressure p.

The requirement that the wormhole be connectible to asymptotically flat spacetime implies that, at the throat, the embedding surface flares outward (see Figs. 1.2 (a), and 1.3). This constraint allows to find the *flaring-out condition*, at or near the throat:

$$\tau_0 > \rho_0 c^2 \tag{1.48}$$

where

$$\tau_0 = \frac{1}{8\pi G c^{-4} b_0^2} \tag{1.49}$$

is the tension in throat. This condition says that in the throat the tension must be so large as to exceed the total density of mass energy $\rho_0 c^2$.
Suppose that the observer is moving through the throat with radial velocity close to the speed of light, $\gamma \gg 1$, where γ is the usual relativistic gamma factor, $\gamma = (1 - v^2/c^2)^{-1/2}$. This observer sees an energy density (the projection of the stress-energy tensor (Eqs. (1.40)) on her time basis vector $e_{\hat{0}'} = \gamma e_{\hat{t}} \mp \gamma(v/c) e_{\hat{r}}$) given by

$$\begin{aligned} T_{\hat{0}'\hat{0}'} &= \gamma^2 T_{\hat{t}\hat{t}} \mp 2\gamma^2 (v/c)^2 T_{\hat{t}\hat{r}} + \gamma^2 (v/c)^2 T_{\hat{r}\hat{r}} \\ &= \gamma^2(\rho_0 c^2 - \tau_0) + \tau_0 \end{aligned} \tag{1.50}$$

So, if the observer moves sufficiently fast, the observer will see a negative density of mass-energy. But the *weak energy condition* requires that no observer should ever be able to measure negative energy density. Then, in the wormhole spacetimes, the weak energy condition is violated. We call material with a negative energy density ($\tau > \rho c^2 > 0$) *exotic matter*. Clearly, it means that the matter threading the wormhole must exert gravitational repulsion in order to stay stable against collapse. Although there are known violations of the energy conditions (e.g. the Casimir effect [13]), it is far from clear at present whether large macroscopic amounts of exotic matter exist in nature. If natural wormholes exist in the universe, then there should be observable electromagnetic signatures of such objects. The observational data allow to establish an upper bound on the total amount of exotic matter under the form of wormholes of $\sim 10^{-36} g cm^{-3}$. The production of this kind of matter in the laboratory is completely out of the current technical possibilities.

1.6 Alternative to Schwarzschild in the weak field limit

The Ellis wormhole has provided the first example of a non-Schwarzschild object within General Relativity. The drainhole model has in common with the Schwarzschild manifold, the ability to reproduce the external gravitational field of a massive, nonrotating, spherically symmetric body. While in the Schwarzschild model the spatial cross sections Σ_t are flat, and the capture effects can be attributed only to the gravitational field, in the drainhole model some of the credit must go to the curvature of space around the drainhole. Note that Ellis wormhole does not asymptotize to Schwarzschild metric: the deviations from Minkowski space do not fall as $1/r$ far from the object, but decay as $1/r^2$. V. Bozza and A. Postiglione [14] investigate particularly the implication of non-Schwarzschild metric from the point of view of the energy-momentum tensor. They examine a more general metric that fall asymptotically as $1/r^q$ in the weak field limit. They introduce a spherically symmetric metric in the form

$$ds^2 = A(r)c^2dt^2 - B(r)dr^2 - r^2C(r)(d\theta^2 + sin^2\theta d\phi^2) \tag{1.51}$$

and take for the functions $A(r)$, $B(r)$ and $C(r)$ the slowest decaying term in a form of power-law as follows

$$A(r) = 1 - \frac{\alpha}{r^q} + o\left(\frac{1}{r^q}\right) \tag{1.52}$$

$$B(r) = 1 + \frac{\gamma}{r^q} + o\left(\frac{1}{r^q}\right) \tag{1.53}$$

$$C(r) = 1 + \frac{\beta}{r^q} + o\left(\frac{1}{r^q}\right). \tag{1.54}$$

This metric is equivalent to the Schwarzschild metric and to the Ellis wormhole with a suitable choice of the parameters q, α, β and γ

Schwarzschild metric	$q = 1, \alpha = \gamma = 0, \beta = 0$
Ellis wormhole	$q = 2, \alpha = \gamma = 0, \beta = a^2$.

To simplify the analysis they use a trasformation for the radial coordinate

$$\tilde{r} = r\left(1 + \frac{\xi}{r^q}\right) \tag{1.55}$$

and set $\beta = \gamma$. It is important to understand now, how this metric is linked to the components of the energy-momentum tensor.

Putting the metric (Eq. (1.51)) in Einstein equations, the only non-zero components at highest power in r that dominate at infinity are

$$G_t^t = \frac{q(1-q)\gamma}{r^{q+2}} = \kappa\rho \tag{1.56}$$

$$G_r^r = \frac{q(\gamma-\alpha)}{r^{q+2}} = -\kappa p_r \tag{1.57}$$

$$G_\theta^\theta = G_\phi^\phi = \frac{q^2(\alpha-\gamma)}{2r^{q+2}} = -\kappa p_t \tag{1.58}$$

with $\kappa = 8\pi G/c^4$. Then, the nonzero components of the energy-momentum tensor are

the energy density	$\rho = T_t^t$
the radial pressure	$p_r = -T_r^r$
the tangential pressure	$p_t = -T_\theta^\theta = -T_\phi^\phi$.

Note that the empty Minkowski space, characterized by $\rho = p_r = p_t = 0$, is obtained for $q = 0$ and the Schwarzschild metric for $q = 1$ and $\alpha = \gamma$, which corresponds to the only other possible vacuum solution: $\rho = p_r = p_t = 0$. As we can see, all components of the energy-momentum tensor must be in linear relation each other. Since the ratios of equations (1.56)-(1.58) are all independent of the radial coordinate r and they can be used to derive equations of state in the form $p_r = \omega_r\rho$, $p_t = \omega_t\rho$ with

$$\omega_r = \frac{\gamma-\alpha}{\gamma(q-1)}, \quad \omega_t = \frac{q(\alpha-\gamma)}{2\gamma(q-1)} \tag{1.59}$$

The Figure 1.5 shows a graphical representation of the whole parameter space by projecting the values of ρ, p_r and p_t at a given radial coordinate to a unit sphere. The unit sphere with the dashed circles corresponding to different asymptotic behaviours r^{-q}. Therefore, the only degeneracy arises in the case $q = 1$, which necessarily implies that (Eq. (1.56)) the energy density is null: the circle at $q = 1$ collapses to a line with $\rho = 0$ on the plane (p_r, p_t).
Bozza and Postiglione have identified several interesting families of solutions imposing one property on the metric or on the source equations of state and derived the costraints on the other variables by Einstein equations. In the Table 1.1 I summarize the zoology of these results.

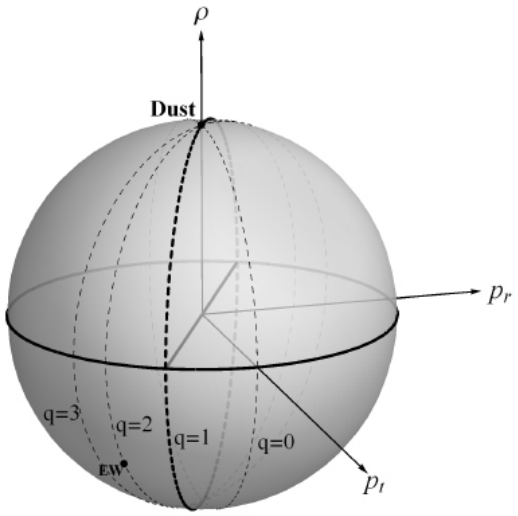

Figure 1.5: Graphical representation of the parameter space of generic metrics depending on the asymptotic ratios of energy density, radial and tangential pressures. Dashed circles corresponding to different asymptotic behaviours r^{-q} of the metric are shown. **Dust** ($p_r = p_t = 0$) is on top of the sphere, Ellis Wormhole ($p_r = p_t = \rho$) is shown as **EW**. As noted in the text, the circle q = 1 actually collapses to a line on the plane ($p_r = p_t = \rho = 0$). V. Bozza and A. Postiglione [14].

FAMILY	q	α	γ	ρ	p_r	p_t	**METRIC**
EMPTY	0	$\forall$	$\forall$	0	0	0	Minkowski
PF (a)	$0 < q < 1$	$\alpha = \gamma$	$\gamma > 0$	$\rho > 0$	0	0	dust halo
PF (b)	$q > 1$	$\alpha = \gamma$	$\gamma > 0$	$\rho < 0$	0	0	exotic dust
PF (c)	$q > 1$	$\alpha = \gamma$	$\gamma < 0$	$\rho > 0$	0	0	void
PF (d)	$0 < q < 1$	$\alpha = \gamma$	$\gamma < 0$	$\rho < 0$	0	0	exotic void
PF (e)	-2	$\forall$	$\gamma < 0$	$\rho > 0$	$\rho(\alpha - \gamma)/3\gamma$	p_r	FRW, $\kappa > 0$
PF (f)	-2	$\forall$	$\gamma > 0$	$\rho < 0$	$\rho(\alpha - \gamma)/3\gamma$	p_r	FRW, $\kappa < 0$
AS	1	$\forall$	$\forall$	0	$\forall$	$-p_r/2$	anis. stress
$\boldsymbol{\rho = 0}$	$\forall$	$\forall$	0	0	$\forall$	$-qp_r/2$	no curvature
$\boldsymbol{\alpha = 0}$	$\forall$	0	$\forall$	$\forall$	$\rho/(q-1)$	$-qp_r/2$	no redshift
NL	$\forall$	$\forall$	$\gamma = -\alpha$	$\forall$	$2\rho/(q-1)$	$-qp_r/2$	no lensing

Table 1.1: The zoology of non-Schwarzschild asymptotic solutions. Perfect Fluid **PF** includes the cases: $q = 0$, equivalent to Minkowski metric; $\alpha = \gamma$ Extended Dust Distribution; the weak field limit with $q = -2$, equivalent to Friedmann-Robertson-Walker (FRW) metric with curvature. Pure Anisotropic stress family **AS** is the case $q = 1$. This metric at large radii decays as $1/r$ as in Schwarzschild. Schwarzschild is included in this family for the case $\alpha = \gamma$. Zero spatial curvature, imposing $\gamma = 0$ has vanishing energy density $\boldsymbol{\rho = 0}$. Zero potential family is defined by $\boldsymbol{\alpha = 0}$. This family contains Ellis Wormhole for $q = 2$. Zero lensing family **NL** has $\alpha = -\gamma$. When $\alpha > 0$, for an attractive potential, γ is negative and the energy density can be kept positive, with $q > 1$.

As we can see something exotic must happen: the energy density ρ can be negative. In fact, in their asymptotic solution they have investigated about energy conditions and found that these energy conditions allow a lot of permissible space in the spherically symmetric asymptotic limits of General Relativity. In particular, the positivity of the energy density is expressed by the relation

$$q(1-q)\gamma \geq 0 \tag{1.60}$$

With positive energy density and with the spatial curvature $\gamma > 0$, the exponent q can take values between 0 and 1. When $q > 1$, the energy density must have positive or negative values as $\gamma < 0$ or $\gamma > 0$ respectively. This is the case, for example of the Ellis Wormhole. In isotropic coordinates, EW has: $q = 2$, $\alpha = 0$ and $\gamma = a^2/2$. Its source has negative energy density with equations of state: $p_r = \rho$ and $p_t = -\rho$ (Eqs. (1.56), (1.59)). The weak energy condition expressed by $\rho + p_r \geq 0$ and $\rho + p_t \geq 0$ becomes

$$q(\alpha - q\gamma) \geq 0 \tag{1.61}$$

$$q[2\gamma - q(\alpha + \gamma)] \geq 0 \tag{1.62}$$

The weak energy condition is satisfied if and only if the energy density is positive and $\alpha \geq q\gamma$ (Eq. (1.61)).
Any asymptotic behavior r^{-q} for the weak field metric, can be obtained by a minimally coupled scalar field with a self-interaction potential **SF** of the form $V(\varphi) = V_0\varphi^n$, with $n = 4/q + 2$. They start from the action

$$S = \int d^4x\sqrt{-g}\left[\frac{R}{2\kappa} + \epsilon\left(\frac{1}{2}\partial_\mu\varphi\partial^\mu\varphi - V(\varphi)\right)\right] \tag{1.63}$$

with $\epsilon = \pm 1$ allowing for a change in the sign of the scalar field lagrangian density. For a static spherically symmetric configuration, φ is a function of the radial coordinate r and the energy-momentum tensor gives

$$\rho = \epsilon\left[\frac{\varphi'^2}{2}\left(1 - \frac{\gamma}{r^q}\right) + V(\varphi)\right] \tag{1.64}$$

$$p_r = \epsilon\left[-\frac{\varphi'^2}{2}\left(1 - \frac{\gamma}{r^q}\right) + V(\varphi)\right] \tag{1.65}$$

$$p_t = -\rho \tag{1.66}$$

where $\varphi' \equiv \partial\varphi/\partial r$. The effective equation of states can be obtained from the energy-momentum tensor making the ansatz $\varphi(r) = \varphi_0/r^m$ with $m > 0$

$$p_r = \frac{n}{2} - 1, \quad p_t = -1 \tag{1.67}$$

The exponent n assumes all possible values. These equations of state describe the circle labelled by **SF** in Figure 1.6. The Ellis Wormhole is included in this family with $\epsilon < 0$ and $n = 4$.
For the strong energy condition instead, it is necessary to impose that the trace of the tidal tensor $(T_{\mu\nu} - g_{\mu\nu}T/2)X^\mu X^\nu$ should be non negative, where X^μ is any future pointing timelike vector. But, $X^\mu = (1, 0, 0, 0)$ and this condition gives the relation

$$f \equiv (T_{00} - g_{00}T/2) = \frac{1}{2}(\rho + p_r + 2p_t) \geq 0 \tag{1.68}$$

that becomes

$$f = \frac{1}{4}q(1-q)(\alpha + \gamma) \geq 0 \tag{1.69}$$

using Einstein equations (1.56)-(1.58). Therefore, when $q > 1$, the strong energy condition is valid only if $\alpha + \gamma < 0$.

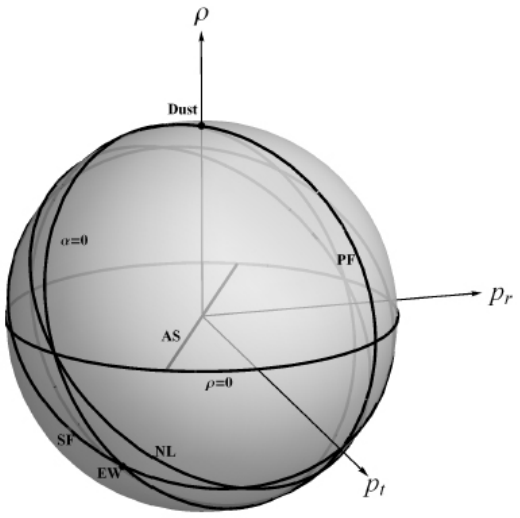

Figure 1.6: Families of metrics with generic asymptotic behaviour projected on the unit sphere in the space (p_r, p_t, ϱ). **EW** is the Ellis wormhole, **PF** stands for perfect fluid, $\boldsymbol{\rho = 0}$ is the family with vanishing energy density, **AS** is the pure anisotropic stress family corresponding to the degenerate $q = 1$ slice, $\boldsymbol{\alpha = 0}$ is the family with vanishing Newtonian potential, **NL** is the family with vanishing gravitational lensing, **SF** is the slice obtained with minimally coupled scalar fields. V. Bozza and A. Postiglione [14].

Chapter 2

Gravitational Lensing

2.1 Early history of gravitational lensing

Gravitational lensing is a direct consequence of general relativity. In 1915, Einstein [15] calculated the deflection angle of a light ray by a massive compact object. If a photon passes near a compact massive object of mass M, at an impact parameter u, the local curvature of space-time will cause the photon to be deflected by an angle

$$\hat{\alpha} = \frac{4GM}{c^2 u} \tag{2.1}$$

where G is Newton's gravitational constant and c is the speed of light, as illustrated in Figure 2.1. Light from a distant star that just grazes the Sun's

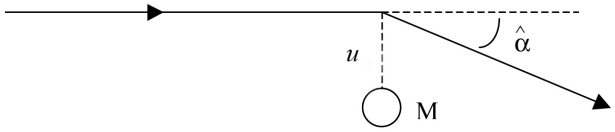

Figure 2.1: Deflection of light by a massive compact object.

surface such that its impact parameter is equal to the radius of the Sun, $R_\odot$, should be deflected by an angle

$$\hat{\alpha} = \frac{4GM_\odot}{c^2 R_\odot} = 1.75\ arcsecond^1 \tag{2.2}$$

[1] 1 arcsecond = 1 as = 1/60th of an arcminute, or 1/3600th of a degree
$M_\odot = 1.99 \times 10^{30} kg$, $R_\odot = 6.96 \times 10^5 km$

In 1919, after Einstein predicted a deflection of this magnitude, an eclipse expedition led by Arthur Eddington photographed stars in the vicinity of the Sun. The circular inset in Figure 2.2 shows that the expected apparent stellar positions are farther from the lens than they would be in the absence of lensing. Comparison of the eclipse photographs with photographs of the same star field taken six months earlier revealed that the positions of the stars were deflected by the amount that Einstein predicted.

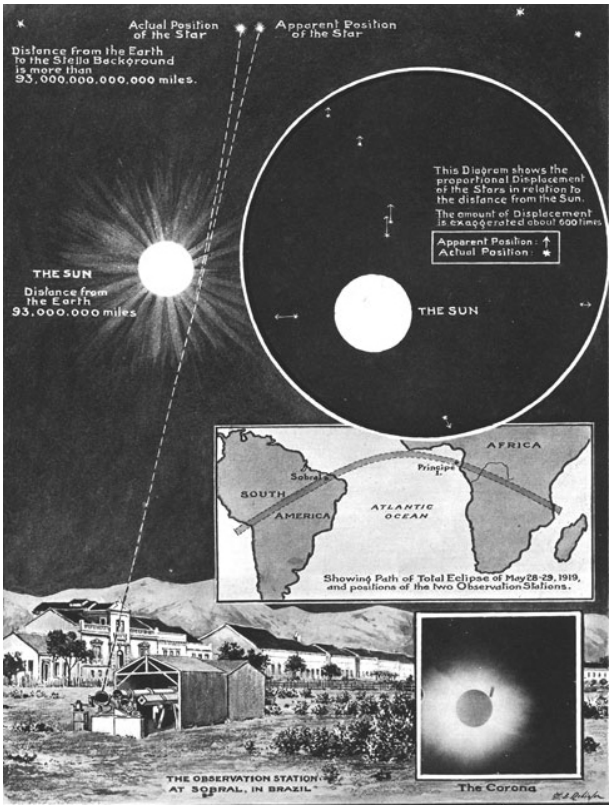

Figure 2.2: Graphical explanation of Eddington's experiment as it appeared in Illustrated London News of November 22, 1919.

This result brought experimental support to the theory of general relativity and it was the first observed example of *gravitational lensing*. This deflection angle has since been repeatedly confirmed with high-precision VLBI measurements in the radio regime [16]. Einstein's notebooks contain calculations of the magnification of images and of the possibility of double images from a single source. In Figure 2.3, the light deflection due to lens galaxy between an observer and a light source is illustrated. In the frame of the observer, the wavefront propagates slower in the gravitational potential of the galaxy

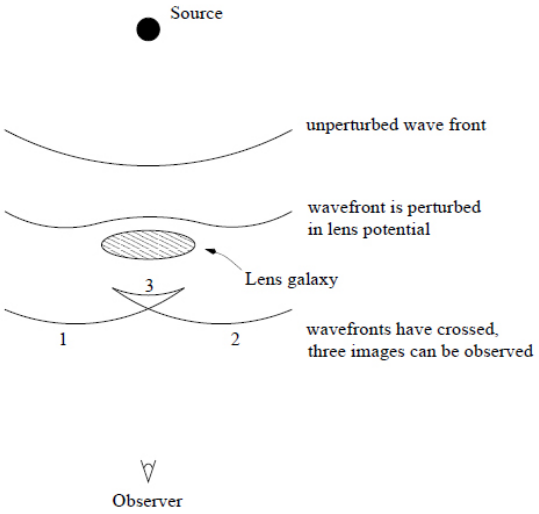

Figure 2.3: Wavefront propagation in a galaxy potential.

than outside. The central part lags behind, and the wavefronts on both sides of the galaxy may even cross if the potential well of the galaxy is massive enough. If the observer is close enough to the optical axis defined by source and galaxy centre, three images of the same source may be seen: two images from the wavefronts on either side, and a very weak (highly demagnified) image in the middle coming from a wavefront that developed when the other two parts of the wavefront crossed. Exactly on the optical axis, the source would even appear as a so-called *Einstein ring*. The gravitational potential of the galaxy acts as a medium with varying refractive index. The observer would see the three images at positions on the sky that are shifted with respect to the original source position without a lens. The light deflection from the straight path is given by Einstein's formula (2.1). In observed lensing systems, the galaxy is normally not circularly symmetric. In this case, five different wavefronts can arrive at an observer close to the optical axis, of which four images are observed while the fifth is usually too faint to be detected. Lensing can produce multiple images in the *strong lensing regime*. Lensing can also amplify the light curves of stars due to *microlensing*, or it can lead to small distortions at the level of a few percent in the shapes of distant galaxies in *weak lensing*. The distinction between these regimes depends on the relative positions of the source, lens, and observer.

2.2 Strong and weak lensing

Gravitational lensing effects can be divided into two regimes, strong and weak lensing, depending on the alignment of the lens and source (Figure 2.4). Strong lensing occurs when the line of sight from the observer to source is very close to the lens, a situation that gives rise to high magnifications, multiple images, arcs and rings in the lens plane. Weak lensing occurs when the lens is located further away from the line of sight, resulting in small magnifications and mild image distortions. Weak lensing is extremely common in the cosmos (at some level, every single light source is affected) but inconspicuous, and can only be detected statistically by studying a large number of lensed light sources. Strong lensing effects, on the other hand, are rare but dramatic, and can readily be spotted in individual sources.

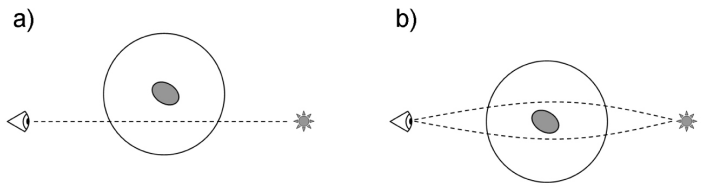

Figure 2.4: Weak and strong lensing. a) Weak lensing occurs when the lens (here illustrated by a gray elliptical galaxy surrounded by a dark matter halo) lies relatively far from the line of sight between the observer (eye) and the background light source (star). In this case, only a single image is produced, subject to mild magnification and distortion. The signatures of this are only detectable in a statistical sense, by studying the weak lensing effects on large numbers of background light sources. b) Strong lensing can occur when the dense central region of the lens is well-aligned with the line of sight. The light from the background light source may then reach the observer along different paths, corresponding to separate images in the sky. This case is also associated with high magnifications and strong image distortions. The angular deflection in this figure, as in all subsequent ones, has been greatly exaggerated for clarity.

Strong lensing has traditionally been divided into subcategories, depending on the typical angular separation of the multiple images produced: macrolensing ($\gtrsim$ 0.1 arcseconds), millilensing ($\sim 10^{-3}$ arcseconds), microlensing ($\sim 10^{-6}$ arcseconds), nanolensing ($\sim 10^{-9}$ arcseconds) and so on. When large galaxies ($\mathrm{M} \sim 10^{12} M_{\odot}$) or galaxy clusters ($\mathrm{M} \sim 10^{14} \div 10^{15} M_{\odot}$) are respon-

sible for the lensing, the image separation typically falls in the macrolensing range, whereas individual solar-mass stars give image separations in the microlensing regime. Since all objects with resolved multiple images due to gravitational lensing have image separations of $\gtrsim 0.1$ arcseconds, the term strong lensing is often used synonymously with macrolensing.
The first strong lensing observation was of the doubly imaged quasar QSO 0957+561 by Walsh, Carswell, and Weymann (1979). The quasar was one of many quasar candidates found in a survey of radio sources made using the MkIA radio telescope at Jodrell Bank. A pair of blue objects separated by ~ 6 arcseconds was found within the field of the quasar in Palomar Observatory Sky Survey (POSS) images. The two blue objects were found to have nearly identical spectra in subsequent observations using the 2.1 m telescope at Kitt Peak National Observatory (KPNO). Observations from Mauna Kea and Palomar showed a luminous galaxy almost in front of one quasar image and a surrounding cluster that might also contribute to the lensing. The quasar is at redshift z = 1.41 while the lensing galaxy is at redshift z = 0.355. An optical image of QSO 0957+561 taken by HST's WFPCII camera is shown in Figure 2.5. The magnification produced by strong lensing affects

Figure 2.5: HST image of QSO 0957+561.

the observable properties of active galaxies, quasars, and any other lensed sources. Strong lensing also may provide information for cosmology. Lensing statistics are sensitive to cosmological parameters, with the frequency of multiple imaging giving constraints on the cosmological constant and the distribution of image splitting probing the amount of structure on galaxy and cluster scales (Mollerach and Roulet 2002 [17], Dodelson 2003 [18]).

2.3 The lens equation

The geometry of lensing is the same in all metric theories of gravity in which light travels along null geodesics, but the relation to the sources of the metric depends on the particular theory. Many of the applications of gravitational lensing concern light from discrete sources bent in the gravitational fields of other discrete bodies. Some interesting and advanced mathematics is needed to properly determine information on the numbers of images and their magnifications. Images formed by galaxies or clusters will be of more distant galaxies, and both, sources and lenses, will be at cosmological distances. In these cases the lenses themselves are small compared with those distances, and are thus often approximated as *thin*, i.e. lying in a plane. These cosmological scales also imply that the comparison spacetime should be curved, FLRW models being the first to study. Indeed, this effect is important in inferring the spatial curvature from CMB observations. Cases involving strong curvatures may require the rigorous approach, which writes spacetime position on the geodesic as a function of the observer's proper time, angles on the observer's celestial sphere and a radial distance. But for many cases, less accurate approximation treatments are adequate.

In a gravitational lens system, the distances to the source and the gravitational lens play an important role. In the standard cosmological model, distances are calculated by integrating over the line element ds in the so called Robertson-Walker metric

$$ds^2 = c^2dt^2 - R^2(t)\left[\frac{dr^2}{1-\kappa r^2} + r^2(d\theta^2 + sin^2\theta d\phi^2)\right] \tag{2.3}$$

It is the metric of a space with spatially constant, but time-dependent curvature $K(t) = \kappa/R^2(t)$, where κ may be taken to belong to the set $\{-1, 0, +1\}$ (for negative, zero, and positive curvature respectively) and $R(t)$ is the curvature radius that scales the spatial part of the metric. As always, (r, θ, ϕ) are the spherical coordinates, t is the time and c is the speed of light.
If light is emitted it also expands with the universe, so that light with a wavelength λ_e from a distant source that has been emitted at the time t_e is redshifted by the expansion of the universe and has the wavelength λ_0, when it is observed at the time t_0. This is expressed by the redshift z

$$1 + z = \frac{\lambda_0}{\lambda_e} = \frac{R(t_0)}{R(t_e)} \tag{2.4}$$

The redshift z can be used to denote the time of emission t_e and is also often used as a measure of the distance of the source.

There are several ways one can calculate distances with the Robertson-Walker metric. For the use in gravitational lensing, the relation between the separation of two sources that subtends a specific angle and the distance of the objects needs to be equal to the Euclidean formula

$$separation \ = \ angle \ \times \ distance \tag{2.5}$$

Distances for which this relation holds are called angular-diameter distances. The angular-diameter distances will be given here only for a homogeneous $\Omega = 1$ (the total density parameter), $\Lambda = 0$ (the cosmological constant) universe (for more general universes see [19] chapter 4 section 5).
In gravitational lensing the quantities that depend on the cosmology are summed up in the normalization of the lensing masses (when we define the critical density Eq. (2.40)). The angular-diameter distance of a source at a redshift of z is given as a solution of the *Dyer-Roeder* equation [20]

$$D = \frac{2}{(1+z)^2}\frac{c}{H_0}(1+z-\sqrt{1+z}) \tag{2.6}$$

The angular-diameter distance between two objects at redshifts z_1 and z_2, with $z_1 \leq z_2$, along the same line of sight takes the form

$$D_{12} = \frac{2c}{H_0}(1+z_1)[R_1(z_2)R_2(z_1) - R_1(z_1)R_2(z_2)] \tag{2.7}$$

where

$$R_1(z) = \frac{1}{1+z} \ , \ R_2(z) = \frac{\sqrt{1+z}}{(1+z)^2} \tag{2.8}$$

so that in general $D_{12} \neq D_2 - D_1$. Another distance measure is the luminosity distance D_L, defined such that the observed flux $\mathcal{F}$ from an isotropic source with intrinsic luminosity $\mathcal{L}$ is $\mathcal{F} = \mathcal{L}/(4\pi D_L^2)$. The measured flux from a source in an expanding universe is reduced compared to a static Euclidean space. In the expanding universe fewer photons with less energy arrive at the detector in a given time. If the total flux of a source is to be calculated, one has to use the corrected luminosity distance D_L to calculate the area of the hypersphere the luminosity of the source is passing through. Then D_L will be equal to $(1+z)^2$ times the angular-diameter distance.
So that, in a curved spacetime and hence in a cosmological applications of gravitational lensing, the angular and luminosity distances do not coincide and then their differences have to be taken into account.

The geometry of a typical gravitational lens system with a single lens is shown in Figure 2.6. The simplest situation corresponds to a point-like mass M (the lens) located close to the line of sight to a source S. The angle θ is the angle of the apparent (observed) position of the source image I and β describes the actual (unobservable) position of the source with respect to the optical axis, chosen along the lens direction. A light ray from the source

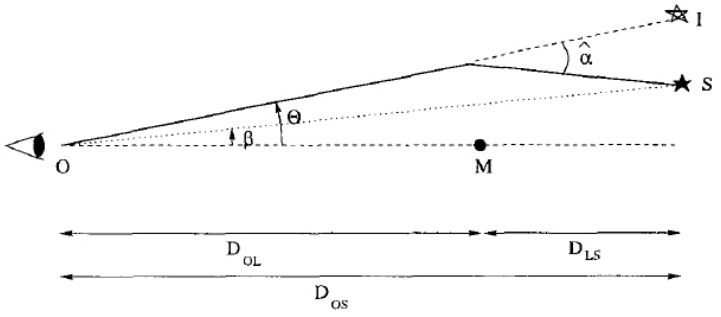

Figure 2.6: Diagram of a point-like lens system. Explanation of symbols is given in the text. S. Mollerach, E. Roulet [17].

is deflected by the gravitational lens at the distance D_{OL} from the observer by the angle $\hat{\alpha}$

$$\theta D_{OS} = \beta D_{OS} + \hat{\alpha} D_{LS}. \tag{2.9}$$

Then, introducing the deflection angle as seen by the observer

$$\alpha = \frac{D_{LS}}{D_{OS}} \hat{\alpha} \tag{2.10}$$

one obtains the *lens equation* in the simple form

$$\beta = \theta - \alpha. \tag{2.11}$$

This is the fundamental equation of gravitational lensing. This relation connects the source position β with the image position θ and the deflection angle α. According to Eq. (2.1) and using that the minimal distance of the light ray to the lens is $u = \theta D_{OL}$, the reduced deflection angle becomes

$$\alpha = \frac{D_{LS}}{D_{OS} D_{OL}} \frac{4GM}{c^2 \theta}. \tag{2.12}$$

In this case, the lens equation takes the form

$$\theta^2 - \beta\theta - \theta_E^2 = 0 \tag{2.13}$$

where θ_E is the *Einstein angle* defined as

$$\theta_E \equiv \sqrt{\frac{D_{LS}}{D_{OS}D_{OL}}\frac{4GM}{c^2}}. \tag{2.14}$$

Thus, clusters of galaxies at cosmological distance ($\sim Gpc^2$) with $M \sim 10^{15}M_\odot$, can result in lensing with Einstein radii of tens of arcseconds. For lensing by single galaxies or groups of galaxies, with masses ranging from $10^{12} \div 10^{15}M_\odot$, the Einstein radii would be correspondingly smaller, on the order of 10 arcseconds or less. For a given source position and deflection field, you may have multiple image solutions. When the lens and the source are perfectly aligned ($\beta = 0$), due to the symmetry of the lens configuration, the image is a ring of angular radius θ_E, as shown in Figure 2.7.

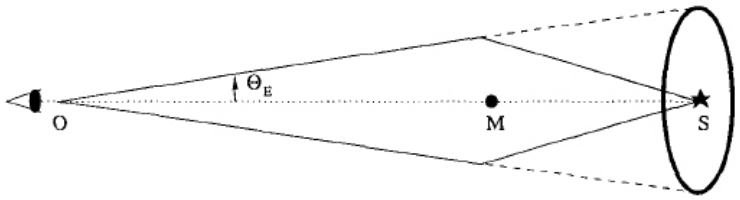

Figure 2.7: Einstein ring due to the gravitational lensing of a source perfectly aligned with the lens. S. Mollerach, E. Roulet [17].

These kind of images are called *Einstein rings*. For a generic position of the source, there will be two images with angular positions

$$\theta_\pm = \frac{\beta}{2} \pm \theta_E\sqrt{1 + \frac{\beta^2}{4\theta_E^2}}. \tag{2.15}$$

As depicted in Figure 2.8, they lie both along the line in the sky determined by the source and the lens positions and at opposite sides of the lens.
The angular separation between the two images is given by

$$\Delta\theta = \theta_+ - \theta_- = 2\theta_E\sqrt{1 + \frac{\beta^2}{4\theta_E^2}}. \tag{2.16}$$

When $\beta < \theta_E$, the source departure from the optical axis is small compared to the Einstein angle, and then the separation of the images is approximately

[2] $1\ pc = 3.086 \times 10^{16}m$

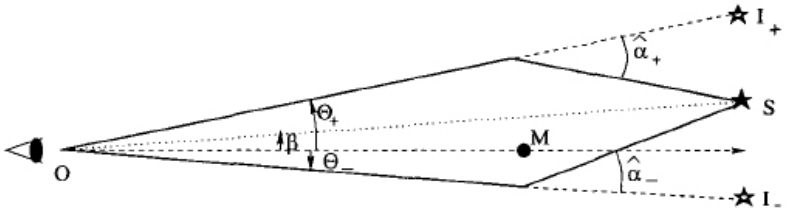

Figure 2.8: Position of the two images of a point-like lens. S. Mollerach, E. Roulet [17].

twice the Einstein angle. When we consider the case of lensing by stars within the Galaxy, the Einstein angle is of order of *mas* and the separation among the images is unresolvable with the present optical telescope. When lensing of quasars by individual stars in foreground galaxy is considered, the distances involved are cosmological and the angular separations become of order of μas. This is the case of microlensing: the separation between the images is not resolved and only a change in the apparent source brightness can be observed. Sources closer than θ_E to the optical axis experience strong lensing in the sense that they are significantly magnified. Sources well outside the Einstein radius are magnified very little.

If the lens is an extended object, the generalized lens equation becomes vectorial. The extent of the lens in the direction of the optical axis is usually much smaller than the distances between observer and lens D_{OL}, and between lens and source D_{LS}. It can be assumed that the lens is thin when compared with the whole light path. The mass distribution of the lens can be replaced by the projected surface mass distribution on a plane, called the *lens plane*. The surface mass density $\Sigma(\overrightarrow{\xi})$ corresponds to the projection of the mass distribution ρ on a plane passing through its center and orthogonal to the light ray direction

$$\Sigma(\overrightarrow{\xi}) = \int dz \rho(\overrightarrow{\xi}, z) \tag{2.17}$$

where $\overrightarrow{\xi}$ is the two dimensional vector indicating the positions in the lens plane and z is the coordinate in the ortogonal direction. The gravitational effect of the lens can be calculated by integrating over the surface elements $d^2\xi$, with the surface mass density Σ in the lens plane using Einstein's result from equation (2.1) for the individual deflection angles (see Figure 2.9).
For an extended mass distribution, the deflection angle $\overrightarrow{\hat{\alpha}}$ at the position $\overrightarrow{\xi}$

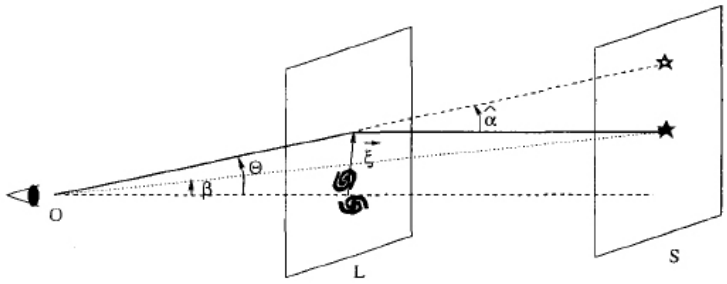

Figure 2.9: Extended lensing distribution. S. Mollerach, E. Roulet [17].

is given by the following generalization of Eq. (2.1)

$$\overrightarrow{\hat{\alpha}}(\overrightarrow{\xi}) = \frac{4G}{c^2}\int \frac{(\overrightarrow{\xi} - \overrightarrow{\xi'})\Sigma(\overrightarrow{\xi'})}{|\overrightarrow{\xi} - \overrightarrow{\xi'}|^2} d^2\xi' \tag{2.18}$$

The plane parallel to the lens plane at the distance D_{OS} of the source from the observer is called the *source plane*. For small angles we have

$$\overrightarrow{\theta}\, D_{OS} = \overrightarrow{\beta}\, D_{OS} + \overrightarrow{\hat{\alpha}}\, D_{LS} \tag{2.19}$$

where $\overrightarrow{\theta} \equiv \overrightarrow{\xi}/D_{OL}$. Note that the small-angle approximation is valid in the known cases of gravitational lensing (even in galaxy clusters the deflection angles are only of the order of 30 as). Then again, introducing the deflection angle as seen by the observer

$$\overrightarrow{\alpha} = \frac{D_{LS}}{D_{OS}}\overrightarrow{\hat{\alpha}} \tag{2.20}$$

the *lens equation* reads

$$\overrightarrow{\beta} = \overrightarrow{\theta} - \overrightarrow{\alpha}. \tag{2.21}$$

Now we consider a rescaled projected gravitational potential

$$\Psi \equiv \frac{2}{c^2}\frac{D_{LS}}{D_{OS}D_{OL}}\psi \tag{2.22}$$

where the projected potential is

$$\psi(\overrightarrow{\xi}) = 2G\int d^2\xi' \Sigma(\overrightarrow{\xi}')ln|\overrightarrow{\xi} - \overrightarrow{\xi}'| \tag{2.23}$$

Using the deflection angle (see Eq. (2.18))

$$\overrightarrow{\hat{\alpha}} = \frac{2}{c^2}\overrightarrow{\nabla}_{\xi}\psi(\overrightarrow{\xi}) \tag{2.24}$$

that shows the relation with the gradient of the projected gravitational potential, we obtain that:

$$\overrightarrow{\alpha} = \overrightarrow{\nabla}_{\theta}\Psi. \tag{2.25}$$

Here the gradient is taken with respect to the angular variables. In this frame the lens equation can be written as

$$\overrightarrow{\beta} = \overrightarrow{\theta} - \overrightarrow{\nabla}_{\theta}\Psi(\overrightarrow{\theta}) \tag{2.26}$$

For each image position $\overrightarrow{\theta}$ there is a unique source position $\overrightarrow{\beta}$ that satisfies the lens equation. But this equation is non-linear in $\overrightarrow{\theta}$ and for some source positions it might be possible to find multiple solutions of the lens equations. When the formation of multiple images appears, we are in the so called *strong lensing regime*.

2.4 Amplification

The gravitational lensing preserves surface brightness. This is due to *Liouville's theorem*. The surface brightness $I(\nu)$ is defined as the flux of energy of a certain frequency ν, crossing a unit area perpendicular to the direction of propagation, per unit time, per unit solid angle and per unit frequency interval

$$I(\nu) = \frac{dE}{dt\ dA\ d\Omega\ d\nu}. \tag{2.27}$$

We consider the radiation emitted by a source as a flux of photons. This source is characterized by a phase-space density

$$f(\overrightarrow{x}, \overrightarrow{p}, t) = \frac{dN}{d^3\overrightarrow{x}\ d^3\overrightarrow{p}} \tag{2.28}$$

which sets the number of photon in a given phase-space volume. The individual photon energy satisfy $E_\gamma = h\nu = cp$, where $p \equiv |\overrightarrow{p}|$ is the photon momentum, and then the beam energy is $dE = E_\gamma dN$. Using that $d^3\overrightarrow{x} = dAcdt$ and that $d^3\overrightarrow{p} = p^2 dp d\Omega$, we can write the phase-space density like

$$f(\overrightarrow{x}, \overrightarrow{p}, t) = \frac{dE}{hcp^3\ d\nu\ d\Omega\ dA\ dt} = \frac{I(\nu)}{hcp^3}. \tag{2.29}$$

The *Liouville's theorem*, applied to the photon beam requires that f be unchanged during the photon propagation if no absorption or emission of photon takes place [21]. This means that the ratio $I(\nu)/p^3$ has to be constant along the trajectory and is not affected by the gravitational deflection of light. The momentum of the photon emitted by a source p_S at redshift z_S is related to the observed photon momentum p_O through the relation, $p_S = (1 + z_S)p_O$. Consequently, the surface brightness conservation in the expanding Universe takes the form

$$I_O(\nu_O) = \frac{I_S(\nu_S)}{(1 + z_S)^3} \tag{2.30}$$

where $\nu_S = (1 + z_S)\nu_O$. If the expansion of the Universe can be neglected, the photon momentum will be conserved as the photon propagates. This also implies that the surface brightness will be conserved.
The flux received from a source is the product of its surface brightness and the solid angle it subtends. Since the surface brightness is conserved, but the differential deflection of light rays changes the shape and the solid angle that the source subtends on the sky, the source luminosity will be amplified by the effect of gravitational lensing by the term

$$A = \frac{d\Omega}{d\Omega_0} \tag{2.31}$$

where $d\Omega$ is the observed solid angle and $d\Omega_0$ is the corresponding solid angle in the absence of lensing (many derivations in this section follow the book *Gravitational Lensing and Microlensing* by Mollerach and Roulet [17]). As seen, for a point-like lens, a source with angular position $\overrightarrow{\beta}$ has two images located at angular positions $\theta_\pm$ given by Eq. (2.15). A source element dS, subtending a solid angle $d\Omega_0 = dS/D_{OS}^2 = \beta d\phi d\beta$, is observed in the image positions subtending a solid angle $d\Omega_\pm = dS_\pm/D_{OL}^2 = \theta_\pm d\phi d\theta_\pm$, as shown in Figure 2.10. The amplification of each of the images can be written as

$$A_\pm = \frac{d\Omega_\pm}{d\Omega_0} = \frac{\theta_\pm d\theta_\pm}{\beta d\beta}. \tag{2.32}$$

From Eq. (2.15) we obtain that

$$A_\pm = \frac{1}{2} \pm \frac{\beta^2 + 2\theta_E^2}{2\beta\sqrt{\beta^2 + 4\theta_E^2}}. \tag{2.33}$$

The image at θ_- has $d\Omega_-/d\Omega_0$ negative, meaning that the image is inverted, and it is said to have negative parity. If the separation of the images is large enough, they can be resolved and the relative amplification A_+/A_-

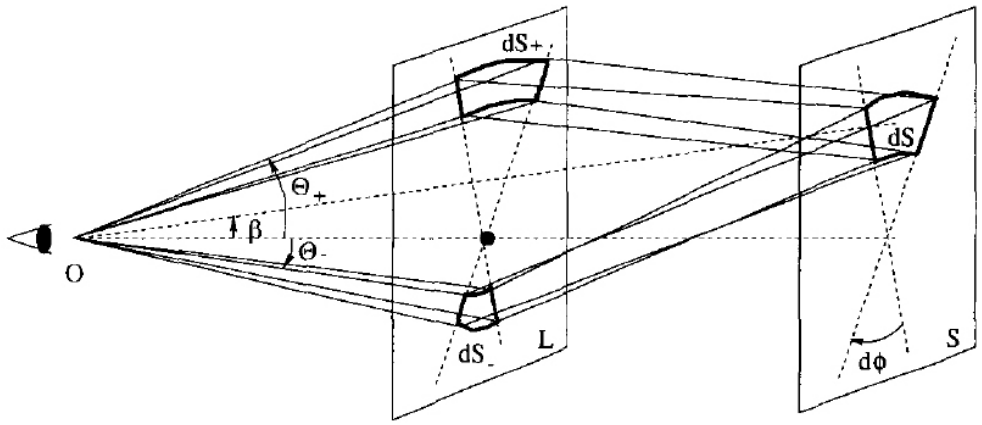

Figure 2.10: Light ray trajectories from a surface element of the source dS in the presence of a point-like lens. The corresponding surface elements of the images in the lens plane are $dS_{\pm}$. S. Mollerach, E. Roulet [17].

of the images can be measured. If the images can not be resolved, we can observe only the total flux received from the source. In this case, its overall amplification is obtained by adding the absolute values of the magnification of two images

$$A = A_+ + |A_-| = \frac{\beta^2 + 2\theta_E^2}{\beta\sqrt{\beta^2 + 4\theta_E^2}}. \tag{2.34}$$

In general, the original source flux is not known and the measure of this amplification from a single observation is not possible. However, if the lens is moving with respect to the line of sight to the source, the amplification will change with time and then, we can measure the variation of the luminosity of the images. For an extended lensing mass distribution with no axis of symmetry, the lens equation (2.21) involves the two-dimensional vectorial deflection $\overrightarrow{\alpha}$. This equation can be interpreted as a two-dimensional *mapping* between the positions of the images $\overrightarrow{\theta}$ and the actual source positions in the sky $\overrightarrow{\beta}$. By defining the Jacobian of this mapping

$$J = det\frac{\partial\overrightarrow{\beta}}{\partial\overrightarrow{\theta}} \tag{2.35}$$

we can relate a differential element of solid angle in the image plane, $d\Omega = d\overrightarrow{\theta_1} \wedge d\overrightarrow{\theta_2}$, with the corresponding one in the source plane, $d\Omega_0 = d\overrightarrow{\beta_1} \wedge$

$d\overrightarrow{\beta_2}$, through the relation $d\Omega = J^{-1}d\Omega_0$. So that the magnification of the corresponding image is given by

$$A = J^{-1}. \tag{2.36}$$

From equation (2.26) we can write the matrix of the mapping between the angular coordinates as

$$\mathcal{T}_{ij} \equiv \frac{\partial \beta_i}{\partial \theta_j} = \left(\delta_{ij} - \frac{\partial^2 \Psi}{\partial \theta_i \partial \theta_j}\right) \tag{2.37}$$

in which the second right-hand term of the equation represents the *Hessian* of the rescaled projected gravitational potential Ψ. Using the *Poisson equation*, the projected gravitational potential can be related to the surface mass density distribution through

$$\nabla^2_{\xi}\psi\big(\overrightarrow{\xi}\big) = 4\pi G\Sigma\big(\overrightarrow{\xi}\big) \tag{2.38}$$

and then we can write

$$Tr\frac{\partial^2 \Psi}{\partial \theta_i \partial \theta_j} = \nabla^2_{\theta}\psi = 2\frac{\Sigma\big(\overrightarrow{\theta}\big)}{\Sigma_{crit}} \equiv 2\kappa\big(\overrightarrow{\theta}\big) \tag{2.39}$$

where we have denoted the critical surface density[3] by

$$\Sigma_{crit} = \frac{c^2}{4\pi G}\frac{D_{OS}}{D_{OL}D_{LS}} \tag{2.40}$$

and the *convergence* by

$$\kappa\big(\overrightarrow{\theta}\big) \equiv \frac{\Sigma\big(\overrightarrow{\theta}\big)}{\Sigma_{crit}}. \tag{2.41}$$

To describe the mapping two additional indipendent combinations of the second derivatives of Ψ are necessary

$$\begin{aligned} \gamma_1 &= \frac{1}{2}\left(\frac{\partial^2 \Psi}{\partial \theta_1^2} - \frac{\partial^2 \Psi}{\partial \theta_2^2}\right) \\ \gamma_2 &= \frac{\partial^2 \Psi}{\partial \theta_1 \partial \theta_2} = \frac{\partial^2 \Psi}{\partial \theta_2 \partial \theta_1} \end{aligned} \tag{2.42}$$

[3]The critical surface density $\Sigma_{crit}(\frac{D_{OL}D_{LS}}{GpcD_{OS}}) = 1.66 \times 10^3 \frac{M_{\odot}}{pc^2} = 0.35\frac{g}{cm^2}$ is a quantitative idea of matter column density required to produce multiple images.

Note that γ_1, γ_2 and κ are functions of $\overrightarrow{\theta}$. The matrix of the mapping can be rewritten as

$$\mathcal{T} = \begin{pmatrix} 1-\kappa-\gamma_1 & -\gamma_2 \\ -\gamma_2 & 1-\kappa+\gamma_1 \end{pmatrix} \tag{2.43}$$

The convergence κ changes the size of the image of a source without modifying its shape. The part of the matrix formed by γ_1 and γ_2 terms is called the *shear* and it is the one responsible for the distortions in the image shape. The matrix $\mathcal{T}$ is symmetric and then is no rotation of the image. By introducing the modulus of the shear $\gamma \equiv \sqrt{\gamma_1^2+\gamma_2^2}$, we can write the amplification as

$$A = (det\mathcal{T})^{-1} = \frac{1}{(1-\kappa)^2-\gamma^2}. \tag{2.44}$$

The amplification has two contributions: one comes from an isotropic focusing due to the local matter density in the lens plane, described by the convergence κ, and the other one from an anisotropic focusing due to the tidal gravitational effects, described by the modulus of the shear γ. The eigenvalues of the mapping matrix are: $1-\kappa-\gamma$ and $1-\kappa+\gamma$. The mapping $\mathcal{T}$ is diagonal when we choose a coordinate system coinciding with the principal axes of the shear at $\overrightarrow{\theta}$ (the principal axes of the shear are obtained by rotating the original ones by an angle ϕ, that satisfies: $tan(2\phi) = \gamma_2/\gamma_1$). We find that the image is streched by a factor $(1-\kappa-\gamma)^{-1}$ in one direction and by $(1-\kappa+\gamma)^{-1}$ in the other. If one of the factors has negative value (negative partial parity), the image is inverted in that direction, and if both eigenvalues are negative, the total parity of the image is positive and hence it will not be inverted, but appears as if rotated by 180°. The amplification for images having both partial parities positive is larger then one. Since for these images both κ and γ are positive, we know that $1 > 1-\kappa > \gamma$, and then $1 > (1-\kappa)^2-\gamma^2 > 0$, which implies that $A > 1$. Notice that, the presence of the lens affects the metric, reducing the area of the observer's sphere and keeping constant the total flux across it. We can also deduce that the light from the images for which both partial parities are negative have passed through a region with $\Sigma > \Sigma_{cr}$. Indeed for them $1-\kappa < -\gamma < 0$ and hence $\kappa > 1$. When multiple images appear, at least one of them has a negative parity. A sufficient condition in order that a lensing distribution be able to produce multiple images is that the surface density, at some point in the lens plane, exceeds the critical value

$$\Sigma(\overrightarrow{\theta}) > \Sigma_{cr} \tag{2.45}$$

(i.e. $\kappa(\overrightarrow{\theta}) > 1$). However, this condition is not actually a necessary one. For the lens to be capable of forming multiple images it is enough that:

$\kappa > 1 - \gamma$. Now we calculate the total amplification of the image for a circularly symmetric system. It is convenient to use polar coordinates with the origin in the symmetry axis of the lens. From equations (2.24) and (2.38), we have that the modulus of the deflection angle is

$$\hat{\alpha}(\xi) = \frac{4GM(\xi)}{c^2 \xi} \tag{2.46}$$

where $M(\xi)$ is the mass enclosed inside a circle of radius ξ

$$M(\xi) = 2\pi \int_0^{\xi} d\xi' \; \xi' \Sigma(\xi) \tag{2.47}$$

Consequently, the deflection angle only depends on the total mass enclosed inside the impact parameter ξ, but not on its radial profile. According to equation (2.46), the lens equation becomes

$$\beta = \theta - \frac{M(\theta)}{\pi D_{OL}^2 \theta \Sigma_{cr}} \tag{2.48}$$

The Einstein angle, specifying the radius of the circular image of a source at $\beta = 0$, has to satisfy the relation

$$M(\theta_E) = \pi (D_{OL} \theta_E)^2 \Sigma_{cr}. \tag{2.49}$$

This means that the average surface density inside the Einstein ring is just the critical density Σ_{cr}. If the density is monotonically decreasing from the center, the condition in order that the formation of the Einstein ring be possible in the circularly symmetric potential (and hence also that multiple images could be formed) is then that the density in the center should exceed the critical density.
The mapping matrix for the symmetric lens is $\mathcal{T} = \text{diag}\,(d\beta/d\theta, \beta/\theta)$, i.e.

$$\mathcal{T} = \begin{pmatrix} 1 - \dfrac{1}{\pi D_{OL}^2 \Sigma_{cr}} \dfrac{\partial}{\partial \theta} \left[\dfrac{M(\theta)}{\theta} \right] & 0 \\ 0 & 1 - \dfrac{M(\theta)}{\pi D_{OL}^2 \Sigma_{cr} \theta^2} \end{pmatrix} \tag{2.50}$$

The radial and tangential magnification of the image are given by

$$A_r \equiv \left(\frac{d\beta}{d\theta} \right)^{-1} \tag{2.51}$$

$$A_t \equiv \left(\frac{\beta}{\theta} \right)^{-1} \tag{2.52}$$

so that the factor A_r describes the change in the radial dimension of the source due to the lensing, and the factor A_t describes the tangential magnification of the image, as a tangential length of the source $\beta\delta\phi$ is stretched in the image to $\theta\delta\phi$. The total amplification of the image is

$$A = A_r A_t = \frac{\theta}{\beta}\frac{d\theta}{d\beta}. \tag{2.53}$$

For a point-like lens, $\partial M/\partial\theta = 0$ and the mapping matrix becomes $\mathcal{T} = \text{diag}\,(1-\gamma, 1+\gamma)$, where the shear is $\gamma = -M/(\pi D_{OL}^2 \Sigma_{cr}\theta^2)$. Since the space around a point-like lens is empty, the convergence vanishes and then a point-like lens is a pure shear system outside the central singular point.

2.5 Critical lines and caustics

The amplification factor is a function of $\overrightarrow{\theta}$, determined by the deflection law $\overrightarrow{\beta}(\overrightarrow{\theta})$. The determinant of the Jacobian matrix may have either sign. The images of the source for which the determinant is positive (negative) are said to possess positive (negative) parity. A source can also have images for which the determinant vanishes. Formally, one could assign the parity 0 to such *critical* images. The parity of an image determines its circulation (orientation) relative to that of the unperturbed image. In the images of positive parity, the direction of curvature is preserved, whereas in negative parity images it is reversed. Regions in the lens plane where the Jacobian determinant has opposite sign are separated by curves on which the latter vanishes. These curves are termed *critical curves*. On these curves, the amplification factor diverges. However, this divergence does not mean that the image of a source is actually infinitely bright, because two additional facts must be taken into account. First, real sources are extended. For such sources, the amplification is a weighted mean of Eq. (2.36) over the source. This always leads to finite amplifications. Second, even if a source were point-like, the amplification would still not be infinite either, because of wave-optics. The critical curves of a deflection mapping are of great importance for a qualitative understanding of its properties. Consider the images of the critical curves under the lens mapping. These curves in the source plane are called *caustics*. Given the positions of observer and lens, the number of images in general varies with the source position. *The number of images changes by two if, and only if, the source crosses a caustic.* Depending on the direction of crossing, two images with opposite parity merge into one on the critical curve and then disappear, or vice versa. Shortly before their fusion, or after their creation, the images are very bright, since they are in the vicinity

of the corresponding critical curve in the lens plane. If the locations of the caustics are known, it is easy to determine the dependence of the number of images on the position of the source, just by using the previous property. The only additional information required is that *for any transparent* [4] *matter distribution with finite mass, the number of images of a point source is one if the source is sufficiently misaligned with the lens.* Transparency of the lens excludes mass distributions that have points of infinite surface density. In addition, from these arguments one can infer the validity of the odd-number theorem: *the total number of images produced by transparent lenses has to be odd*, a result known as *Burke's theorem* [22]. When the lens is singular, Burke's theorem does not necessarily hold. For instance, for the point-like lens there are always two images, with opposite parities, for any source position. For non-singular lenses it is usually very hard to observe all the images. Generally, one of them appears very demagnified and it is located near the center of the lensing distribution, where a galaxy typically lies. This demagnified central image is actually the one that would be missing in the limit in which the lensing potential becomes singular.
The lens equation can also be expressed by *Fermat's principle*. We rewrite the lens equation (Eq. (2.26)) as

$$\overrightarrow{\theta} - \overrightarrow{\beta} - \overrightarrow{\nabla}_\theta \overrightarrow{\Psi} = \overrightarrow{\nabla}_\theta \left[\frac{1}{2} (\overrightarrow{\theta} - \overrightarrow{\beta})^2 - \Psi \right] = 0 \tag{2.54}$$

where the second term in the parenthesis is proportional to the gravitational time delay. In fact, the projected gravitational potential is also useful to express the gravitational time delay (or *Shapiro* delay [23]) caused by a given mass distribution

$$\delta t_{grav}(\overrightarrow{\xi}) = -\frac{2}{c^3} \psi(\overrightarrow{\xi}). \tag{2.55}$$

We can also find that the geometrical time delay coming from the increment in the path length of the deflected ray with respect to the straight path, that it would have followed in the absence of lenses, is given by

$$\delta t_{geom} = \frac{D_{OS} D_{OL}}{2 c D_{LS}} (\overrightarrow{\theta} - \overrightarrow{\beta})^2. \tag{2.56}$$

The total time delay will be given by the sum of the geometrical and gravitational delays. Both of them are produced in the neighborhood of the lens and hence when the distance to the lens is large, one has to take into account that during the photon travel from the lens to the Earth, the Universe has expanded by a factor $(1 + z_L)$, where z_L is the redshift of the lens. The delay

[4] so that no images are obscured

measured by an observer will then be stretched by the same factor, and from Eqs. (2.22), (2.55) and (2.56) is

$$\delta t = \frac{1+z_L}{c}\frac{D_{OL}D_{OS}}{D_{LS}}\left[\frac{1}{2}\left(\overrightarrow{\theta}-\overrightarrow{\beta}\right)^2-\Psi\right]. \tag{2.57}$$

It follows from the lens equation (Eq. (2.54)) that

$$\overrightarrow{\nabla}_\theta(\delta t)=0 \tag{2.58}$$

For a fixed source position $\overrightarrow{\beta}$, the images will appear along those directions $\overrightarrow{\theta}$ for which the time delay has an extreme, and hence the geometrical optics approach used so far is actually equivalent to Fermat's principle. When multiple images are formed, the light travel time for each image is in general different. Variations in the source intensity would arrive to the observer at different times and these time delays are in principle measurable. They can be exploited to infer the expansion rate of the Universe. Since the angular-diameter distances for known redshifts scale with H_0, if one has a theoretical model $\psi\left(\overrightarrow{\theta}\right)$ for the system, the measurement of a time-delay between the images of a multiple image gravitational lens system determines the Hubble constant H_0 [24].
One model for the mass distribution in galaxies assumes that the stars and other mass components behave like particles of an ideal gas, confined by their combined, spherically symmetric gravitational potential. This mass distribution, called a *singular isothermal sphere*, can be written as

$$\rho(r)=\frac{\sigma^2}{2\pi G r^2} \tag{2.59}$$

where ρ is the mass density distribution, σ is the velocity dispersion of the stars, and r is the radius of the sphere. Notice that, since $\rho \propto r^{-2}$, the mass $M(r)$, increases with r. Therefore the circular velocity is

$$v_c^2(r)=\frac{GM(r)}{r}=2\sigma^2=constant. \tag{2.60}$$

This simple model approximately produces the observed flat rotation curves of galaxies. In the case of the circularly symmetric lens, the origin can be shifted to the center of symmetry, reducing the problem to one dimension. Projecting along the line of sight, the surface mass density is

$$\Sigma(\theta)=\frac{\sigma^2}{2GD_{OL}\theta} \tag{2.61}$$

and the mass enclosed inside a circle of angular radius θ is then

$$M(\theta) = \frac{\pi\sigma^2 D_{OL}\theta}{G}. \tag{2.62}$$

Narayan and Bartelmann [25] show that the deflection angle corresponding to this mass distribution is

$$\hat{\alpha}(\theta) = \frac{4\pi\sigma^2}{c^2} \tag{2.63}$$

The resulting Einstein radius of the singular isothermal sphere is

$$\theta_E = \frac{4\pi\sigma^2 D_{LS}}{c^2 D_{OS}} = \frac{D_{LS}}{D_{OS}}\hat{\alpha} = \alpha. \tag{2.64}$$

Therefore, due to circular symmetry, the lens equation for the singular isothermal sphere is one-dimensional. Multiple images are obtained only if the source lies inside the Einstein ring, when $\beta < \theta_E$. When this condition is satisfied, the lens equation has two solutions

$$\theta_\pm = \beta \pm \theta_E. \tag{2.65}$$

The images at $\theta_\pm$, the source, and the lens lie on a straight line. Computing the reduced projected potential for this lens one obtains

$$\Psi(\overrightarrow{\theta}) = \theta_E|\overrightarrow{\theta}|. \tag{2.66}$$

The amplification of the images is given by

$$A_\pm = \frac{\theta_\pm}{\beta} = 1 \pm \frac{\theta_E}{\beta}. \tag{2.67}$$

Consider a circular galaxy behind a large lensing mass density with the observer out of the page as shown in Figure 2.11a. Since the light rays are deflected by the lensing mass, we do not observe a circular image. The light rays originating from the bottom of the source (the ones closer to the lens) are bent more than those farther from the lens. The light rays are bent such that the bottom appears farther away from the lens. Note that rays are bent toward the lens, so that as you extrapolate backward, the more a ray is bent toward the lens, the farther away the source appears to be. Images will therefore be distorted as in Figure 2.11b. The net effect is to turn a circular galaxy into the arc shown in Figure 2.11c (Dodelson 2003 [18]).
The location of an arc in a cluster provides a simple way to estimate the projected cluster mass within a circle traced by the arc. For a circularly symmetric lens, the radius of the circle traced by the arc gives an estimate

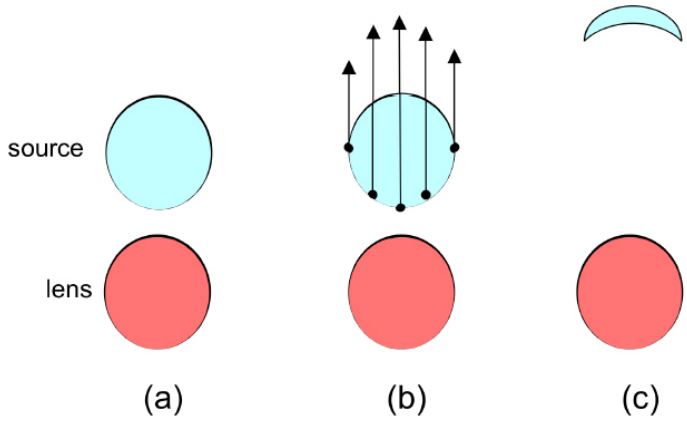

Figure 2.11: Arc formation.(a) The circular source galaxy (blue) is located behind the lens (red). The observer is out of the page so that the foreground lens is between the observer and the source. (b) Light rays from the source are deflected as they pass near the lens. Rays traveling closest to the lens get deflected the most. (c) The resulting image is an arc.

of the Einstein radius. It follows that, for a softened isothermal sphere, with mass distribution given by

$$\rho(r) = \frac{\sigma^2}{2\pi G(r^2 + r_c^2)} \tag{2.68}$$

where r_c is the core radius, the mass enclosed inside a circle of radius θ, can be estimated by

$$M(\theta) = \frac{\pi\sigma^2 D_{OL}}{G}(\sqrt{\theta^2 + \theta_c^2} - \theta_c) \tag{2.69}$$

with $\theta_c \equiv r_c/D_{OL}$. The lens equation can be written as:

$$\overrightarrow{\beta} = \overrightarrow{\theta}\left[1 - \frac{\theta_0}{\theta^2}\left(\sqrt{\theta^2 + \theta_c^2} - \theta_c\right)\right] \tag{2.70}$$

where the angle θ_0 would correspond to the Einstein angle in the limit of negligible core radius, Eq. (2.64). Critical lines are present whenever multiple images can form. One critical line corresponds to the Einstein ring, having an angular radius

$$\theta_E = \theta_0\sqrt{1 - \frac{2\theta_c}{\theta_0}} \tag{2.71}$$

and being the image of a source located at the point-like caustic at $\beta = 0$. Another critical line forms when $d\beta/d\theta = 0$ and has angular radius

$$\theta_R = \sqrt{\theta_0 \theta_c}\left[1 - \frac{\theta_c}{2\theta_0}\left(1 + \sqrt{1 + \frac{4\theta_0}{\theta_c}}\right)\right]^{1/2} \tag{2.72}$$

which is smaller than the Einstein radius. The corresponding caustic is a circle with angular radius $\beta_R = \beta(\theta_R)$. The condition for the existence of both critical lines is clearly that the central surface density be larger than the critical density. The position of the images is obtained by solving the lens equation (2.70), which can be rewritten as a cubic equation

$$\theta^3 - 2\beta\theta^2 + [\beta^2 - \theta_0(\theta_0 - 2\theta_c)]\theta - 2\beta\theta_0\theta_c = 0. \tag{2.73}$$

This equation has one or three solutions (images) depending on the location of the source. Sources located outside the circular caustic ($\beta > \beta_R$) have just one image while those located inside have three images. The additional images of extended sources located in the vicinity of this caustic will look elongated in the radial direction, since being $d\beta/d\theta \simeq 0$ in this case means that the radial extent of the image is much larger than that of the source, and this is why this caustic is named the *radial caustic*. Images of sources close to the origin, near the point-like caustic, appear tangentially elongated, forming large arcs near the location of the Einstein ring. This is illustrated in Figure 2.12. The shapes of the image(s) of a circular source are drawn for different source positions. In the limit of small core radius all the results of the singular model are recovered. Indeed, in this limit one has $\theta_E \to \theta_0$. The radial critical line collapses to a point, according to $\theta_R \simeq \sqrt{\theta_E \theta_c}$, and hence for small core radii the third image is lost, leaving only two images for $\beta < \beta_R \simeq \theta_E$. The reduced projected gravitational potential in the softened isothermal sphere model is given by

$$\Psi(\overrightarrow{\theta}) = \theta_0[\sqrt{\theta^2 + \theta_c^2} - \theta_c ln(\sqrt{\theta^2 + \theta_c^2} + \theta_c)]. \tag{2.74}$$

Notice that in this example, the mass distribution has no singularities and the number of images is odd, as expected from Burke's theorem.
Since each image direction corresponds to a unique position in the source plane, the mapping from the image to the source plane is single valued. When multiple images of source are formed, the mapping from the source plane to the image plane becomes multiply valued. In order to visualize the properties of multiply imaged system, we consider now the observer's sky, the *image plane*, as if it were a deformable sheet, the *sky sheet*. The mapping from the image plane to the source plane will transform this sheet, stretching

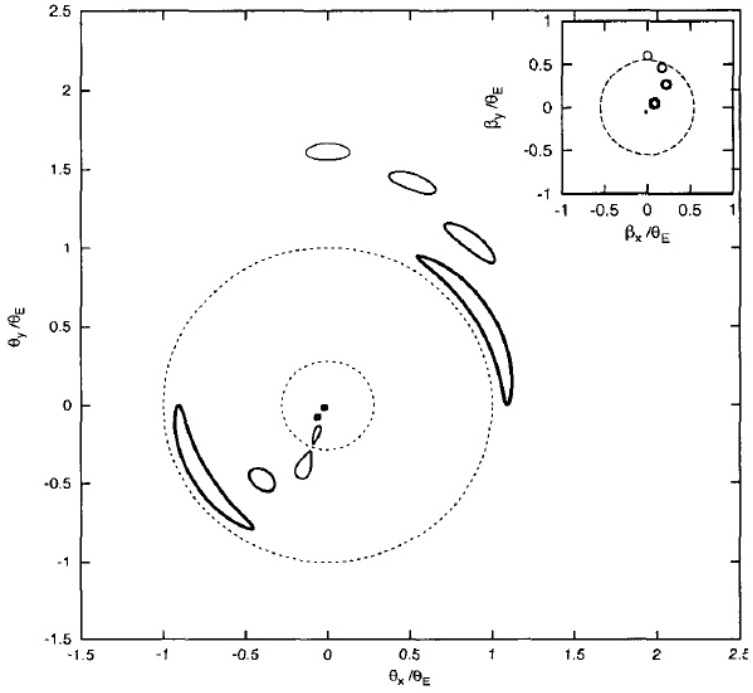

Figure 2.12: Images of a circular source lensed by a non-singular isothermal sphere, for four different source locations, indicated in the smaller panel. The source in the vertical is just outside the caustic (indicated with dashed lines) and it has one image, also appearing along the vertical. The other sources have three images. The one just inside the caustic has two new images radially elongated, which are close to the radial critical line (smaller circle in the main panel). As the source approaches the origin (the point-like caustic) two of the images become very elongated tangentially around the location of the Einstein ring (the bigger circle), while the third image is near the center and very demagnified. S. Mollerach, E. Roulet [17].

and eventually, if multiple imaging occurs, folding it but as long as the lenses are nonsingular, without tearing it. Figure 2.13 shows a folded sheet in a one dimensional example. For a given source position, the number of times the

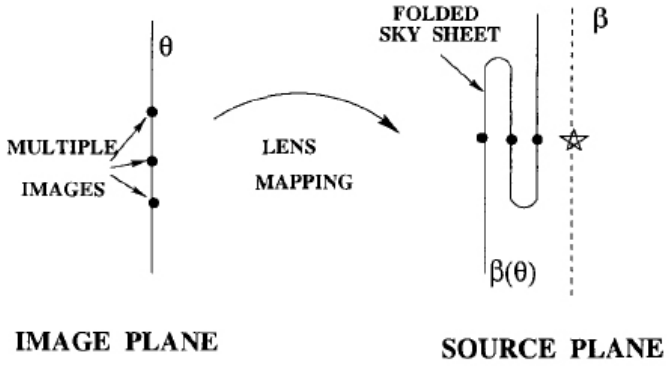

Figure 2.13: Folded sheet representing the observer's sky projected back into the source plane in a strong lensing situation. S. Mollerach, E. Roulet [17].

sky sheet is folded on top of the source location will determine the number of images of the source. If no folds are present, just one image will be seen. Every fold will add an additional pair of images, one of which will be inverted. The mapping among these sheets can be performed by considering light rays which arrive to the observer along directions forming a regular grid (in $\overrightarrow{\theta}$) and following them back to the source plane. The original grid defines the two-dimensional observer's sky (θ_1,θ_2). The image of this grid defines the sheet projected into the source plane (β_1,β_2). The folds in the projected surface will hence define the caustics, and these will be closed lines in the source plane which can be smooth or can eventually contain cusps where two folds merge.

2.6 The binary lens

A natural generalization of the Schwarzschild lens is a lens consisting of two point masses. This model can be used to describe microlensing by binary stars or planetary systems. Furthermore, this lens model is sufficiently simple that one can derive many properties analytically. The deflection angle of the light rays is given by the superposition of the vectorial deflections produced by the two individual lenses. If lenses are point-like, with masses M_A and M_B, and are located in the lens plane forming angles $\overrightarrow{\theta}_A$ and $\overrightarrow{\theta}_B$, with

respect to the chosen optical axis, the lens equation can be written as

$$\overrightarrow{\beta} = \overrightarrow{\theta} - \mu_A(\overrightarrow{\theta} - \overrightarrow{\theta}_A)\frac{\theta_E^2}{|\overrightarrow{\theta} - \overrightarrow{\theta}_A|^2} - \mu_B(\overrightarrow{\theta} - \overrightarrow{\theta}_B)\frac{\theta_E^2}{|\overrightarrow{\theta} - \overrightarrow{\theta}_B|^2} \qquad (2.75)$$

where $\mu_{A,B} = M_{A,B}/M$, are the reduced masses, with $M = M_A + M_B$, the total mass. The Einstein angle θ_E is obtained from the Eq. (2.14), using the total mass M. As seen in the previous section, the presence of the second lens component breaks the axial symmetry of the system. But, the resulting lensing effect is much different from the case of a single lens. First of all, the lens becomes astigmatic. This results into a completely different magnification pattern on the source plane and in the appearance of extended caustics. In fact, caustics are lines that separate regions with different image multiplicities. When the source crosses a caustic during its motion relative to the lens, new images are created or destroyed. As in the case of a single point mass, the image separations are too small to allow to see them, but the light curves are generally much more complicated and exhibit multiple peaks, asymmetries, etc. Figure 2.14 shows how the projection of the image plane into the source plane would appear for an asymmetric binary system, with reduced masses $\mu_A = 0.25$, $\mu_B = 0.75$, and for different values, in decreasing order, of the distance between the lenses.

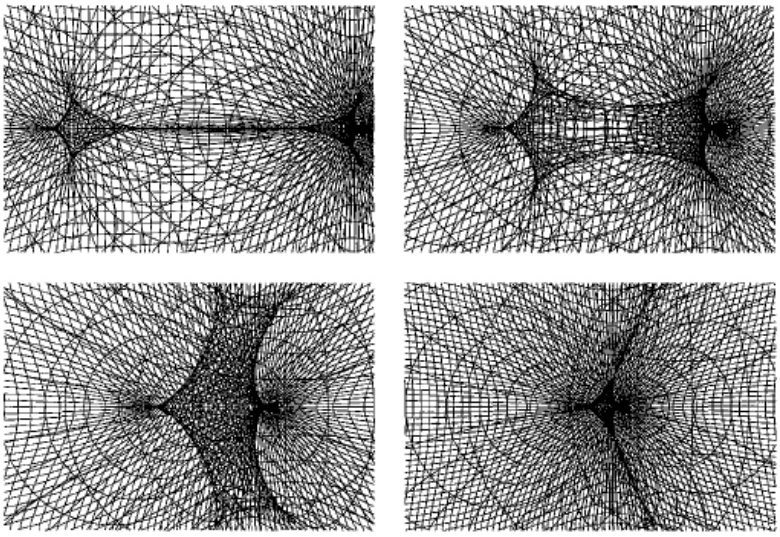

Figure 2.14: Sky sheet for a point-mass binary lens for decreasing values of the distance between the lenses. S. Mollerach, E. Roulet [17].

In the first panel, in which the separation among the lenses is large, there

are two diamond shaped caustics with four cusps (*wide binary topology*), one associated to each lens. They can be interpreted as being the point-like caustics of each lens which have been distorted by the shear induced by the presence of the other lens. As the lenses are taken as point-like, the sky sheet has a hole associated to each lens, and this has been stretched to infinity. Far from the lenses a source would have three images (two of them very demagnified) and inside the diamonds it would have five. In the second panel (top right), the lenses get closer. The two cusps which are closer to the center, one from each diamond, approach each other and merge, leading to a six cusp caustic (*intermediate binary topology*). For smaller values of the lens separation, the six cusp caustic is stretched in the direction orthogonal to the lens separation, as displayed in the third panel. Finally, in the last panel, for even closer lenses, two pairs of fold caustics touch each other and break apart, so that the six cusp caustic separates into a four cusp caustic and two small triangular caustics (*close binary topology*). The changes in the caustic shapes, which occur as the distance between the lenses changes, can also be interpreted in the context of *catastrophe theory*. For instance, the transition from two opposed cusps that merge leaving two folds, as happened between the first and second panels or between the third and fourth ones, is known as a beak-to-beak transition in this context. The lens separation is considered

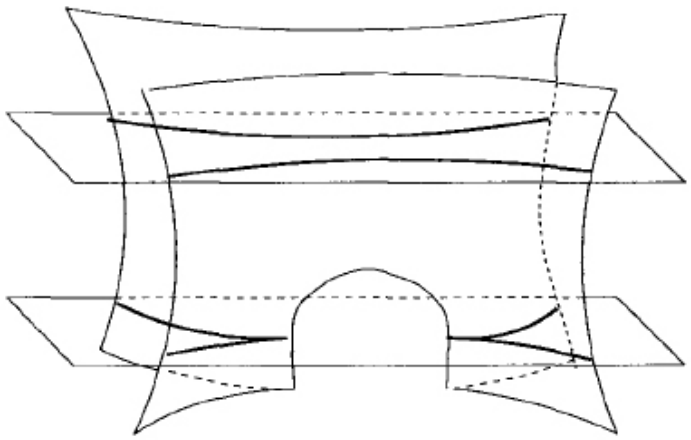

Figure 2.15: Beak to beak transition. S. Mollerach, E. Roulet [17].

as a third control parameter, in addition to the two source coordinates β_1 and β_2, and in this three dimensional space the fold caustics in Figure 2.14 will sweep a surface and the cusps will follow lines as the lens separation is varied. This is schematically illustrated in Figure 2.15, where the horizontal

planes correspond to fixed lens separations and they are displaced vertically as this separation is varied. From this theory arises the property that *cusps appear and disappear in pairs or their number is preserved.* So that, a general property of the caustics produced by a lens is that *the total number of cusps has to be even.*

Now we consider the critical curves and caustics associated with a system with two point-like lenses, where the angular variables are defined in the complex lens plane, and normalized in terms of the Einstein angle θ_E associated to the total mass $M = M_A + M_B$. We introduce source coordinates

$$\zeta \equiv \frac{\beta_x + i\beta_y}{\theta_E} \tag{2.76}$$

and image coordinates

$$z \equiv \frac{\theta_x + i\theta_y}{\theta_E} \tag{2.77}$$

The lens equation (Eq. (2.75)) becomes

$$\zeta = z - \frac{\mu_A}{\bar{z} - \bar{z}_A} - \frac{\mu_B}{\bar{z} - \bar{z}_B} \tag{2.78}$$

where $\mu_j \equiv M_j/M$ and z_j are the location of the lenses, with $j = A, B$. The amplification of an image is given by

$$A_i = J^{-1}|_{z_i} \tag{2.79}$$

where z_i is the position of the image and J is the Jacobian of the mapping from the image to the source plane, and it is equivalent to

$$J(z, \bar{z}) = det \begin{pmatrix} \partial\zeta/\partial z & \partial\zeta/\partial\bar{z} \\ \partial\bar{\zeta}/\partial z & \partial\bar{\zeta}/\partial\bar{z} \end{pmatrix} = \left|\frac{\partial\zeta}{\partial z}\right|^2 - \left|\frac{\partial\zeta}{\partial\bar{z}}\right|^2. \tag{2.80}$$

From Eq. (2.78), $\partial\zeta/\partial z = 1$, and the Jacobian can be rewritten as

$$J = 1 - \left|\frac{\partial\zeta}{\partial\bar{z}}\right|^2 \tag{2.81}$$

with

$$\frac{\partial\zeta}{\partial\bar{z}} = \frac{\mu_A}{(\bar{z} - \bar{z}_A)^2} + \frac{\mu_B}{(\bar{z} - \bar{z}_B)^2}. \tag{2.82}$$

As we know the vanishing of the Jacobian of the mapping determines the critical curves. From Eq. (2.81), this condition can be written as

$$\frac{\partial\zeta}{\partial\bar{z}} = e^{i\varphi}, \quad 0 \leq \varphi < 2\pi \tag{2.83}$$

For simplicity, we put the origin of the coordinates at the midpoint between the two lenses, so that $z_A = -z_B$ and the real axis along the line joining the lenses. Combining the last two equations, we can get a quartic equation for the points defining the critical lines

$$z^4 - z^2(2\bar{z}_A^2 + e^{i\varphi}) - z\bar{z}_A 2(\mu_A - \mu_B)e^{i\varphi} + \bar{z}_A^2(\bar{z}_A^2 - e^{i\varphi}) = 0. \tag{2.84}$$

The four solutions of this equation give us the critical lines. By applying the lens equation (2.78), from the critical lines, one can get the caustics. The shape of the caustics depends on the mass ratio $q = \mu_A/\mu_B$ and on the lens separation in units of the Einstein angle, $d \equiv |z_A - z_B| = 2|z_A|$. Thanks to the large number of parameters involved, the analytical derivation of the critical lines and caustics of binary lens systems is very complicated. Qualitatively, we can find the three regimes (*wide, intermediate, close*), which are illustrated in Figure (2.16) for a binary lens system with mass parameter $\mu_A = 0.25$. When the two lenses are widely separated, they act like single lenses which slightly feel the perturbation of the companion. The point caustic becomes an asymmetric astroid with four cusps. The corresponding critical line becomes an oval (top panel, *wide*). Once the separation of the two lenses decreases, the critical lines and the corresponding caustics merge together. They first touch in one point, then, for further decreasing separations, there is one single critical line and one single caustic, which is characterized by six cusps (middle panel, *intermediate*). For even closer lens position, two regions inside the critical line detach and the caustic breaks down into three parts. These are a central diamond-shaped and two triangular-shaped caustics. By reducing further the separation between the two components, the two triangular caustics move away from the central one, which also shrink (bottom panel, *close*). If the source is inside the caustic, it produces five images: three are inside the critical line and two are outside it. When the source crosses the caustic, two or three images merge together and disappear. During the transition the images assume the usual arc-like shape. Their size increases and therefore they are highly magnified. As the critical lines are the set of points where $J = 0$, at the merging points also the gradient of J has to vanish. The relation between the critical lens separation and the associated mass ratio can be obtained, solving the system of equations $J = 0$ and $\partial J/\partial\bar{z} = 0$. From $J = 0$, the equation (2.81) gives us the condition $|\partial\zeta/\partial\bar{z}| = 1$ and from $\partial J/\partial\bar{z} = 0$, we obtain that $\partial^2\zeta/\partial\bar{z}^2 = 0$. This brings us to the relation between the critical value of $\bar{z}$ and μ_A, μ_B and z_A

$$\bar{z} + z_A = 2z_A\left[1 - \left(-\frac{\mu_A}{\mu_B}\right)^{1/3}\right]^{-1}. \tag{2.85}$$

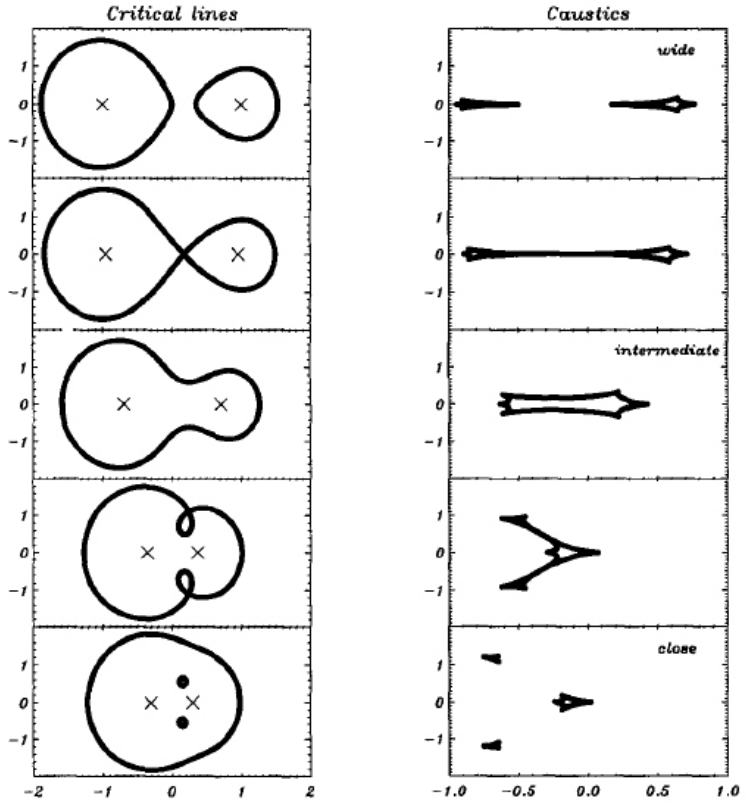

Figure 2.16: The critical lines (left) and caustics (right) for a binary lens system with mass parameter $\mu_A = 0.25$. The crosses indicate the position of the lenses, with the heavier one being to the left. The lens separations are taken in decreasing value from top to bottom, with the second panels corresponding to $d = d_{WI}$ and the fourth ones to $d = d_{IC}$. S. Mollerach, E. Roulet [17].

From this last equation, we get three different values for $\bar{z}$. Inserting these solutions into Eq. (2.82) and requiring that $J = 0$, we can obtain the final expression for the lens separation at the transition points. The transition from wide to intermediate lens systems (corresponding to the -1 root) occurs at a separation

$$d_{WI} = 2z_{A(WI)} = (\mu_A^{1/3} + \mu_B^{1/3})^{3/2}. \tag{2.86}$$

The other two roots, correspond to the two critical points in the transition from the intermediate to close binary systems taking place at the separation

$$d_{IC} = 2z_{A(IC)} = (\mu_A^{1/3} + \mu_B^{1/3})^{-3/4}. \tag{2.87}$$

In the limit of small mass ratios ($q << 1$), as would be the case for planetary systems, one has $d_{WI} \simeq 1 + 1.5\, q^{1/3}$ and $d_{IC} \simeq 1 - 0.75\, q^{1/3}$. This means that both transitions occur for angular separations among the binary lenses are very close to the Einstein angle θ_E. By solving the lens equation (2.78), we can determine the image positions for a given source location ζ. Replacing $\bar{z}$ from the conjugate of the lens equation, we obtain a fifth order equation in z

$$\begin{aligned}&(z^2 - z_A^2)[z + z_A(\mu_A - \mu_B) + (z^2 - z_A^2)(\bar{\zeta} + z_A(\mu_A - \mu_B))] - \\ &(z - \zeta)[(\bar{\zeta}(z^2 - z_A^2) + z + z_A(\mu_A - \mu_B))^2 - z_A^2(z^2 - z_A^2)^2] = 0\end{aligned} \tag{2.88}$$

where the five solutions of this equation corresponds to the five images of the source. A source outside the caustics has only three images, meaning that two solutions of this equation will be spurious. These two solutions correspond to complex values of θ_x and θ_y. We can eliminate these spurious solutions using the lens equation (Eq. (2.78)) as a check.

2.7 Lensing by Binary Galaxies

The problem of lensing by binary galaxies has been studied by E.M. Shin and N.W. Evans [31]. They consider a system of binary galaxies idealized as two isothermal spheres and provide a theoretical treatment like a natural extension of the problem of lensing by binary point masses (Schneider and Weiss [32]). The singular isothermal sphere provides a limiting case for the $1/r^n$ objects obtained when n tends to zero. Binary isothermal spheres differ qualitatively from the case of two point masses by having additional critical curves and caustics and hence also different multiple-imaging properties.
The model is constructed as follows. They use dimensionless source plane

$\boldsymbol{\xi} = (\xi, \eta)$ and lens plane coordinates $\boldsymbol{x} = (x, y)$. The two isothermal spheres are centred on the x-axis at $\pm a$. The deflection potential is defined as

$$\psi(x,y) = E_1[r_{c_1}^2 + (x+a)^2 + y^2]^{1/2} + E_2[r_{c_2}^2 + (x-a)^2 + y^2]^{1/2} \qquad (2.89)$$

with r_{c_1} and r_{c_2} the core radii of the isothermal spheres. If the core radii vanish, Eq. (2.89) reduces to the potential of two singular isothermal spheres with Einstein radii E_1 and E_2. Without loss of generality they take $E_1 \leq E_2$ and $a > 0$. The convergence κ is

$$\kappa(\boldsymbol{x}) = \frac{E_1}{2}\frac{2r_{c_1}^2 + r_1^2}{(r_{c_1}^2 + r_1^2)^{3/2}} + \frac{E_2}{2}\frac{2r_{c_2}^2 + r_2^2}{(r_{c_2}^2 + r_2^2)^{3/2}} \qquad (2.90)$$

and the shear components γ_1 and γ_2 are

$$\gamma_1(\boldsymbol{x}) = \frac{E_1}{2}\frac{y^2 - (a+x)^2}{(r_{c_1}^2 + r_1^2)^{3/2}} + \frac{E_2}{2}\frac{y^2 - (a-x)^2}{(r_{c_2}^2 + r_2^2)^{3/2}} \qquad (2.91)$$

$$\gamma_2(\boldsymbol{x}) = E_2\frac{(a-x)y}{(r_{c_2}^2 + r_2^2)^{3/2}} - E_1\frac{(a+x)y}{(r_{c_1}^2 + r_1^2)^{3/2}} \qquad (2.92)$$

where $r_1^2 = (a+x) + y^2$ and $r_2^2 = (a-x) + y^2$. The Jacobian of the lens mapping can be found from (see Section 2.4)

$$det\boldsymbol{A}(\boldsymbol{x}) = [1 - \kappa(\boldsymbol{x})]^2 - \gamma(\boldsymbol{x})^2 \qquad (2.93)$$

where $\gamma(\boldsymbol{x}) = \sqrt{\gamma_1(\boldsymbol{x})^2 + \gamma_2(\boldsymbol{x})^2}$ is the magnitude of the shear. For an isolated singular isothermal sphere $\gamma = \kappa$ and then $det\boldsymbol{A} = 1 - 2\kappa$. In the binary singular case we have

$$det\boldsymbol{A} = 1 - 2\kappa + 4E_1E_2\frac{a^2y^2}{r_1^3r_2^3}. \qquad (2.94)$$

Therefore on the axis of two singular isothermal spheres $det\boldsymbol{A} = 1 - 2\kappa$. This model can be used to describe lensing by two elliptical galaxies. A fiducial elliptical galaxy lens has parameters: velocity dispersion $\sigma = 250 kms^{-1}$, core radius $r_{c_1} = r_{c_2} = 100pc$ and redshift $z_l = 0.46$. They also take for the source redshift $z_s = 2.15$ and use a ΛCDM concordance cosmology. The corresponding dimensionless Einstein radius is $E \approx 7.11$ (with the lens scale of 1 kpc). The two fiducial isothermal spheres are placed at $(-a, 0)$ and $(a, 0)$. Numerical simulations of critical curves and caustics are shown in Fig. 2.17. They found four configurations for the critical curves and caustics from *Type 0* to *Type 3* as the parameter a is made smaller.

Type 0. When a is large (top-most panels of Fig. 2.17), the critical curves and caustics of the two lenses are disjoint. The outer tangential critical curves are not circular (as they would be for a single such lens in isolation) and the corresponding caustics are distorted astroids with four cusps. There are small radial critical curves around each lens that map to large roundish caustics.
Type 1. For $a = 10.0$, the tangential critical curves have merged into a single outer critical curve, and the corresponding caustics have merged to form a single six-cusp caustic.
Type 2. The six-cusp caustic elongates along the y-axis as a decreases further, and two small three-cusp caustics split off, as two small critical curves ("bean" critical curves) pinch off from the outermost critical curve, to leave a single four-cusp astroid caustic ($a = 5.6$ and $a = 5.4$). At $a = 4.0$, the three-cusp caustics have moved away from the origin and enlarged, whilst the "bean" critical curves have moved towards the origin and enlarged.
Type 3b. Decreasing a still further, the two "bean" critical curves merge with the two radial critical curves, creating two critical curves around the origin (bottom-most panels). The inner one maps to a caustic with two butterfly cusps, whilst the outer one maps to the outermost caustic. The outermost critical curve still corresponds to an astroid caustic around the origin.

In a wide binary, each galaxy has individual tangential and radial caustics. As the separation of the binary decreases, the caustics is subjected to three metamorphoses. The first metamorphosis occurs when the tangential caustics merge to form a single six-cusped caustic, lying interior to the radial caustics. At smaller separations, the six-cusped caustic undergoes the second metamorphosis. It splits into a four-cusped caustic and two three-cusped caustics, which shrink to zero size (an *elliptic umbilic catastrophe*) before they enlarge again and move away from the origin perpendicular to the binary axis.
A third metamorphosis occurs as the threecusp caustics join the radial caustics. This leaves an inner distorted astroid caustic enclosed by two outer caustics. For two singular isothermal spheres ($r_{c_1} = r_{c_2} = 0$), the critical curves and caustics, using the same terminology of the cored ($r_{c_1}, r_{c_2} > 0$) case, can be of *Type 0*, *1*, and *2*. However the difference between the singular and cored cases is that the radial critical curves around the two galaxy centres shrink to zero size as the core radii decrease to zero. There are no radial caustics. Any core images move towards the centres of the isothermal spheres as r_{c_1} and r_{c_2} tends to zero, their magnifications diminishing, until they disappear at the singularities. A source can produce either an odd or an even number of images. This depends on the number of core images it would produce if the core radii were not zero. The number of images changes

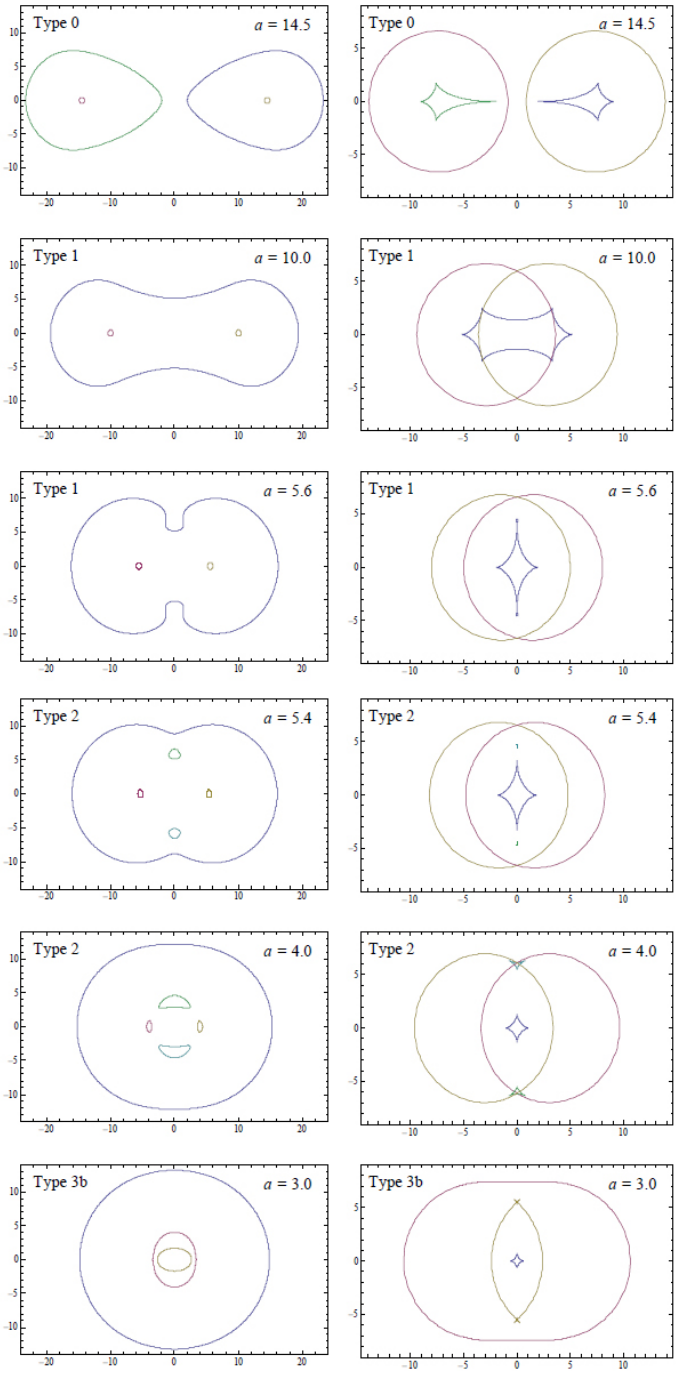

Figure 2.17: Critical curves (left panels) and caustics (right panels) for two identical fiducial isothermal spheres (with dimensionless Einstein radius ~ 7.11) separated by dimensionless distance 2a. Colours of corresponding critical curves and caustics match. The *Type* of the critical-curves or caustics is defined in the text. E.M. Shin and N.W. Evans [31].

by one (an image is created or destroyed at the centre of a singular isothermal sphere) when the source crosses a *pseudocaustic*. The pseudocaustic is a closed curve in the source plane which is approached by the radial caustics when r_{c_1} and r_{c_2} tends to zero. By considering the lens mapping on small circles around the singularities, it is possible to find the positions of the pseudocaustics. The lens equation, in vector form is

$$\boldsymbol{\xi} = \boldsymbol{x} - E_1 \frac{\boldsymbol{x}+\boldsymbol{a}}{|\boldsymbol{x}+\boldsymbol{a}|} - E_2 \frac{\boldsymbol{x}-\boldsymbol{a}}{|\boldsymbol{x}-\boldsymbol{a}|} \tag{2.95}$$

with $\boldsymbol{a} = (a, 0)$. Consider a small circle of radius δ in the lens plane, centred at the second singular isothermal sphere. When δ goes to zero, $\boldsymbol{x} \to \boldsymbol{a}$ and $(\boldsymbol{x} + \boldsymbol{a}) \to (2a, 0)$, although $E_2(\boldsymbol{x} - \boldsymbol{a})/|\boldsymbol{x} - \boldsymbol{a}|$ becomes E_2 times a unit direction vector. Then a circle around the singularity at $\boldsymbol{a}$ maps to a circle in the source plane of radius E_2, centred at $(a - E_1, 0)$. In the same way, it is possible to derive the other pseudocaustic for the singularity at $-\boldsymbol{a}$, as a circle of radius E_1, centred at $(-a + E_2, 0)$.
The "bean" critical curves surround small regions of positive $det\boldsymbol{A}$ inside the tangential critical curves, where $det\boldsymbol{A}$ is negative. These regions exist because there are points where the shear is zero. In fact, if $\gamma(\boldsymbol{x}) = 0$ at some $\boldsymbol{x}$, then $det\boldsymbol{A} > 0$ (see Eq. (2.93)). Since the shears from the two isothermal spheres cancel out, for the double isothermal sphere lens there are two points where $\gamma(\boldsymbol{x}) = 0$. It is possible to determine the position of the points of zero shear for the isothermal spheres: if the isothermal spheres, singular or not, are located at $(\pm a, 0)$, the points of zero shear lie on a circle of radius a centred at the origin. First of all they write the shear as the complex quantity

$$\Gamma = \gamma_1 + i\gamma_2 \equiv \gamma e^{2i\omega} \tag{2.96}$$

with ω the angle of shear. Since the deflection potential of two spheres is the sum of their two separate deflection potentials, the complex shear will be the sum of two separate shears: $\Gamma = \Gamma^{(1)} + \Gamma^{(2)}$. If the shear is zero at same point $\boldsymbol{x}$, we obtain

$$\omega^{(2)}(\boldsymbol{x}) = \omega^{(1)}(\boldsymbol{x}) + \frac{(2k+1)\pi}{2} \qquad k \in \mathbb{Z}. \tag{2.97}$$

This last relation holds if

$$\theta_2 - \theta_1 = \pm\frac{\pi}{2} \tag{2.98}$$

where θ_j is the direction of $\boldsymbol{x}$ from the centre of the jth isothermal sphere. Then the line segment joining $(-a, 0)$ to $\boldsymbol{x}$ is perpendicular to that joining $(a, 0)$ to $\boldsymbol{x}$. The points $\boldsymbol{x}$ lie on the circle with the two galaxy centres as its

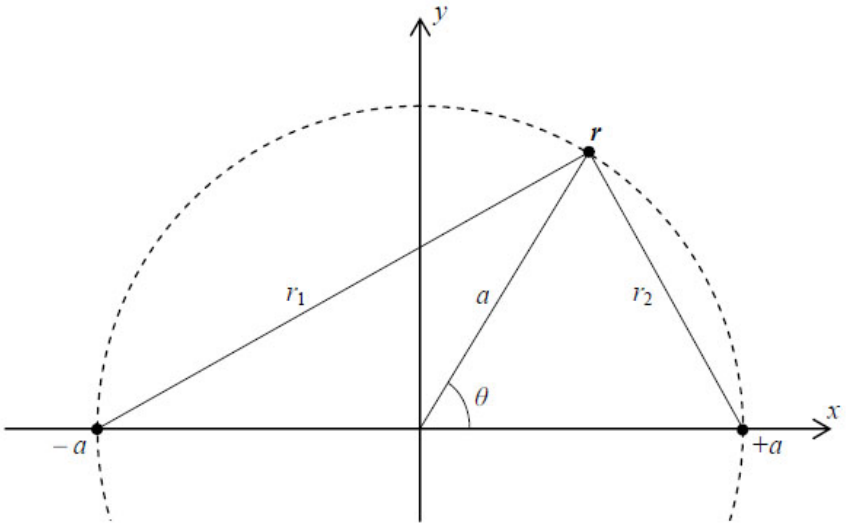

Figure 2.18: The point of zero shear lies on the circle $|r| = a$. The centres of the (singular or cored) isothermal speres are at $\pm a$ on the x-axis. E.M. Shin and N.W. Evans [31].

diameter, $|r| = a$, as shown in Fig. 2.18.
The second metamorphosis is characterized by the elliptic umbilic catastrophe. This catastrophe occurs when the point of zero shear, is also a critical point. To find the lens parameters at which the elliptic umbilic catastrophe takes place, it is necessary to know the polar coordinates (a, θ_{zs}) of the point of zero shear. On the circle $|r| = a$ we have

$$r_1^2 = 2a^2(1 + cos\theta), \qquad r_2^2 = 2a^2(1 - cos\theta) \tag{2.99}$$

where r_1 and r_2 are the distances between a point $\boldsymbol{r}$ and the centres of the isothermal spheres. For a single isothermal sphere, the magnitude of shear is

$$\gamma^{(j)} = \frac{1}{2} E_j \frac{r_j^2}{(r_c^2 + r_j^2)^{3/2}} \tag{2.100}$$

(where r_j is the distance from its centre), and then the point of zero shear for the double lens has

$$\frac{r_1}{r_2} = \frac{E_1}{E_2}. \tag{2.101}$$

Combining this last equation with (2.99) we obtain the relation

$$cos\theta_{zs} = \frac{E_1^2 - E_2^2}{E_1^2 + E_2^2} \tag{2.102}$$

At the point of zero shear (see Eq. (2.93)) $det\boldsymbol{A} = (1-\kappa)^2$, where the convergence κ is

$$\kappa(r,\theta) = \kappa^{(1)} + \kappa^{(2)} = \frac{E_1}{2r_1} + \frac{E_1}{2r_1}. \tag{2.103}$$

Using Eqs. (2.99) and (2.102), and putting (2.103) into $(1-\kappa)^2 = 0$ we have

$$a = \frac{1}{2}\sqrt{E_1^2 + E_2^2}. \tag{2.104}$$

Therefore, from Eqs. (2.102) and (2.104) we have that the polar coordinates (a, θ_{zs}) of the point of zero shear depend on the Einstein radii E_1 and E_2 of the isothermal spheres. As we have seen, binary isothermal spheres differ from the case of two point masses. They have additional critical curves and caustics, or pseudocaustics in the case of singular isothermal spheres, and hence different multiple-imaging properties. If the isothermal spheres are coreless, the number of images may be 1, 2, 3, 4 or 5. If the isothermal spheres haves cores, the number of images can be 1, 3, 5 or 7, depending on three parameters: the location of the source, the separation of the binary and the velocity dispersions.

Chapter 3

Gravitation $1/r^n$

A broad literature exists on lensing by any kind of non-Schwarzschild metrics [26, 27]. While these metrics predict strong deviation from Schwarzschild in the strong deflection regime, they typically reduce to Schwarzschild in the weak field limit, leaving only subdominant tiny corrections in the most explored regime. However, there is a considerable exception: the Ellis wormhole [66]. This metric, introduced so as to demonstrate the possibility to connect two asymptotically flat regions by a non-singular throat, has the interesting property of falling down as $1/r^2$ asymptotically. Thus, any observables depending on the gravitational field is affected, even in the weak field limit. Concentrating on the gravitational lensing effect, it has been proved that the bending angle by an Ellis wormhole goes as $1/u^2$ instead of $1/u$ (where u is the impact parameter) [28, 29, 30] and that it is possible to obtain a total amplification smaller than one. This implies that for certain geometries the combined flux of the images is smaller than the original flux of the source (defocusing effect), which is impossible to achieve in ordinary gravitational lensing by isolated objects [29] (in the context of ordinary matter, demagnification can only occur for lines of sight along underdense regions [63]). Actually, defocusing is not an accident of the Ellis wormhole metric. Gravitational lensing by metrics falling as $1/r^n$ has been studied by Kitamura et al. [33], who showed that the deflection angle inherits the same exponent as the metric: $\hat{\alpha} \sim 1/u^n$. They also showed that the defocusing effect is generic for any metrics falling as $1/r^n$, with $n > 1$. The physical problem of gravitational lensing by metrics falling as $1/r^n$ has been deeply investigated in a sequence of papers appeared in the last few years [34]. Metrics falling as $1/r^n$ were first studied in Ref. [33] as a phenomenological extension of the Ellis wormhole case, while the implications for the energy-momentum tensor supporting this kind of metrics were only considered in Ref. [14]. They prove that some violation of the weak energy density must necessarily

occur in order to have a metric falling faster than Schwarzschild ($n > 1$). As a consequence, the observation of defocusing in some physical lenses would provide a smoking gun for the existence of exotic matter. On the other hand, many authors have proved that it is possible to obtain wormhole solutions without exotic matter in modified theories of gravity [68].

3.1 Demagnification condition

Following Kitamura et al. [33] we assume that an asymptotically flat, static and spherically symmetric modified spacetime could depend on the inverse distance to the power of positive n in the weak field approximation. They consider light propagating through a four-dimensional spacetime (in this frame G = c = 1). The four-dimensional spacetime metric is

$$ds^2 = -\left(1 - \frac{\varepsilon_1}{r^n}\right) dt^2 + \left(1 + \frac{\varepsilon_2}{r^n}\right) dr^2 + r^2(d\theta^2 + \sin^2\theta d\phi^2) + O(\varepsilon_1^2, \varepsilon_2^2, \varepsilon_1\varepsilon_2) \tag{3.1}$$

where r is the circumference radius and ε_1 and ε_2 are small parameters in the iterative calculations. These parameters may be either positive or negative, respectively. Notice that negative ε_1 and ε_2 for $n = 1$ corresponds, in the linearized Schwarzschild metric, to a negative mass. The light propagation is not affected by the conformal transformation. Then, it is useful to make a conformal transformation with a factor of $(1 - \varepsilon_1/r^n)^{1/2}$. At the linear order of ε_1 and ε_2, the spacetime metric takes the form

$$d\bar{s}^2 = -dt^2 + \left(1 + \frac{\varepsilon}{R^n}\right) dR^2 + R^2(d\theta^2 + \sin^2\theta d\phi^2) + O(\varepsilon^2) \tag{3.2}$$

where $\varepsilon \equiv n\varepsilon_1 + \varepsilon_2$ and $R^2 \equiv r^2/(1 - \varepsilon_1/r^n)$. Since the spacetime is spherically symmetric, they focus on the equatorial plane ($\theta = \pi/2$) and find the deflection angle of light at the linear order

$$\alpha = 2\int_{R_0}^{\infty} \frac{d\phi(R)}{dR} dR - \pi = \frac{\varepsilon}{b^n} \int_0^{\pi/2} \cos^n\psi d\psi + O(\varepsilon^2) \tag{3.3}$$

where R_0 is the closest approach and b is the impact parameter, of the light ray. The integral factor becomes

$$\begin{aligned} \int_0^{\pi/2} \cos^n\psi d\psi &= \frac{(n-1)!!}{n!!}\frac{\pi}{2}\ (even\ n), \\ &= \frac{(n-1)!!}{n!!}\ (odd\ n), \\ &= \frac{\sqrt{\pi}}{2}\frac{\Gamma\left(\frac{n+1}{2}\right)}{\Gamma\left(\frac{n+2}{2}\right)}\ (real\ n > 0). \end{aligned} \tag{3.4}$$

It is possible to rewrite the deflection angle as

$$\alpha(b) = \frac{\bar{\varepsilon}}{b^n} \tag{3.5}$$

by absorbing the numerical constant into the $\bar{\varepsilon}$ parameter. This deflection angle recovers the Schwarzschild ($n = 1$) and Ellis wormhole ($n = 2$) cases. In the thin-lens approximation [19] the lens equation becomes

$$\beta = \frac{b}{D_L} - \frac{D_{LS}}{D_S}\alpha(b). \tag{3.6}$$

Here, as usual, β denotes the angular position of the source, D_L, D_S and D_{LS} are the distances from the observer to the lens, from the observer to the source, and from the lens to the source, respectively. For a source in (or near) the Einstein ring, we have a significant magnification (or demagnification). As we saw in the previous chapter, the Einstein ring is defined by the condition $\beta = 0$. From equation (3.6), we have for $\varepsilon < 0$ no positive roots for $\beta = 0$ (because of the repulsive force in the particular gravity model). Instead, for $\varepsilon > 0$ there is always a positive root corresponding to the Einstein ring. In this last case, the lens equation can be rewritten, in units of the Einstein ring radius as

$$\hat{\beta} = \hat{\theta} - \frac{1}{\hat{\theta}^n} \qquad (\hat{\theta} > 0) \tag{3.7}$$

$$\hat{\beta} = \hat{\theta} + \frac{1}{(-\hat{\theta})^n} \quad (\hat{\theta} < 0) \tag{3.8}$$

where $\hat{\beta} \equiv \beta/\theta_E$ and $\hat{\theta} \equiv \theta/\theta_E$ for the angular position of the image $\theta \equiv b/D_L$. For a general positive n, it is possible to find exact solutions for the modified lens equation. In gravitational microlensing, only the significantly amplified images become detactable and these events occur when a source (e.g. a distant star) crosses the Einstein ring. For the $\hat{\beta} < 1$ case, Equations (3.7) and (3.8) are solved, in the Taylor series form with respect to $\hat{\beta} < 1$, to obtain

$$\hat{\theta}_+ = 1 + \frac{1}{n+1}\hat{\beta} + \frac{1}{2}\frac{n}{(n+1)^2}\hat{\beta}^2 + O(\beta^3) \qquad (\hat{\theta} > 0) \tag{3.9}$$

$$\hat{\theta}_- = -1 + \frac{1}{n+1}\hat{\beta} - \frac{1}{2}\frac{n}{(n+1)^2}\hat{\beta}^2 + O(\beta^3) \quad (\hat{\theta} < 0). \tag{3.10}$$

By using the last two equations, we derive the amplification factor of each image

$$A_\pm = \frac{1}{\hat{\beta}(n+1)} + O(\hat{\beta}^0). \tag{3.11}$$

Then, the total amplification is

$$A_{tot} \equiv A_+ + A_- = \frac{2}{\hat{\beta}(n+1)} + O(\hat{\beta}^0). \tag{3.12}$$

Note that for the Schwarzschild case ($n = 1$), the total amplification is always larger than unit for $\hat{\beta} < 1$, as we know. Demagnifying gravitational lenses could appear when the impact parameter of light $\hat{\beta}$ and the power n satisfy the condition

$$\hat{\beta} > \frac{2}{n+1} \tag{3.13}$$

in units of the Einstein ring radius under a large-n approximation. The total demagnification could occur only when $\hat{\beta}$ is small, but larger than the critical value $2/(n+1)$. The compatibility of the assumption $\hat{\beta} < 1$ and Eq. (3.13) implies that $n > 1$. Kitamura et al. performed a test of their analytic result. Figure 3.1 shows the total amplification factor of the lensed images as a function of the source position for $n = 1, 2, 3$ and 10. They found a good agreement for the analitical critical value $\hat{\beta} = 2/11 = 0.182$ with the numerical one $\hat{\beta} = 0.187$. Figure 3.2 shows a numerical light curves for the same minimum impact parameter of the light trajectory $\hat{\beta}_0 = 0.1$. Examples of $n = 3$ and $n = 10$ show maximally ~ 10 and ~ 60 percent depletion of the light, when the source position is $\hat{\beta} \sim 1.1$ and $\hat{\beta} \sim 0.7$, respectively. What is asserted allows us to think that gravitational demagnification of light occurs because modified lenses could act as an effectively negative mass on a particular light ray. Then, a gravitational demagnification of light might be used for hunting a clue of exotic matter and energy.

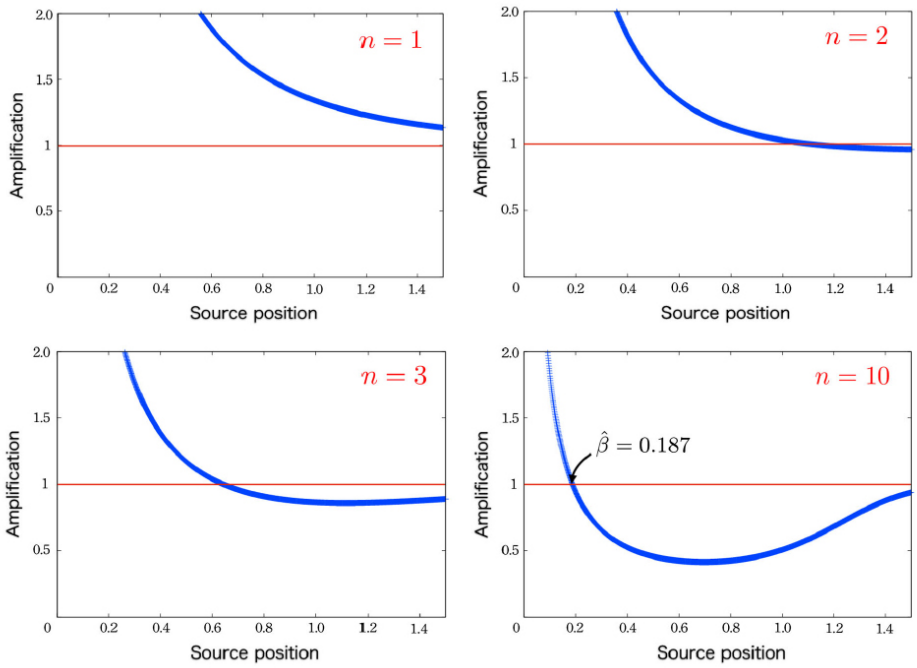

Figure 3.1: Total amplification factor of the lensed images as a function of the source position $\hat{\beta}$ for $n = 1, 2, 3$ and 10. Top left, top right, bottom left, and bottom right panels correspond to $n = 1, 2, 3$ and 10, respectively. In the case of $n = 10$, the total amplification factor is larger than unity for $\hat{\beta} < 0.187$, whereas it is smaller for$\hat{\beta} > 0.187$. For convenience, a thin (red) line denotes $A_{tot} = 1$. Kitamura et al [33].

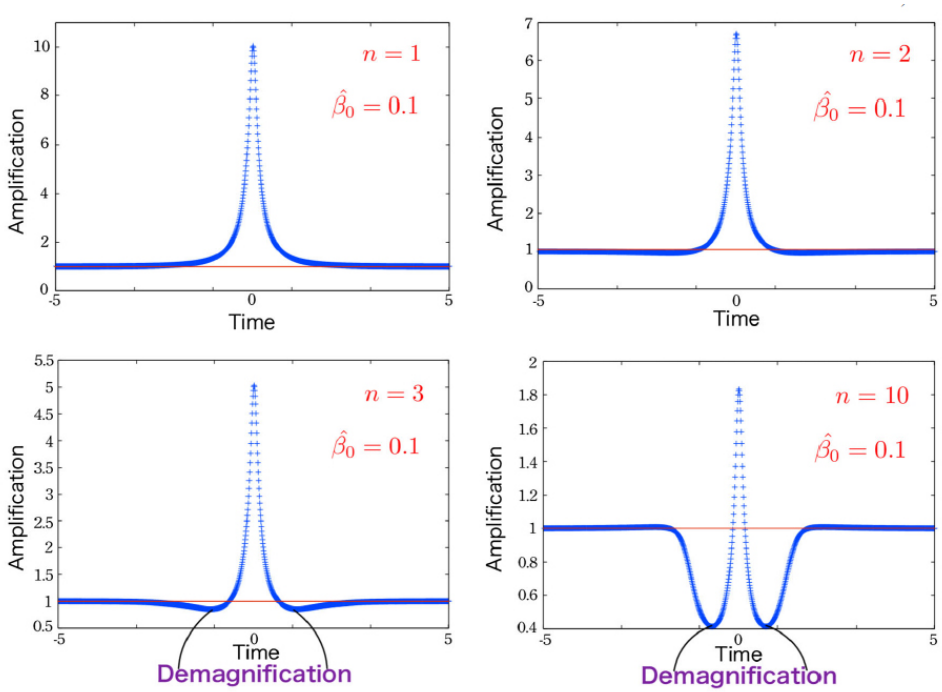

Figure 3.2: Numerical light curves for the same minimum impact parameter of the light trajectory $\hat{\beta}_0 = 0.1$. The source star moves at constant speed and the source position changes as $\hat{\beta}(t) = (\hat{\beta}_0^2 + t^2)^{1/2}$, where time is normalized by the Einstein ring radius crossing time. Top left, top right, bottom left, and bottom right panels correspond to $n = 1, 2, 3$ and 10, respectively. For convenience, a thin (red) line denotes $A_{tot} = 1$. Kitamura et al. [33].

3.2 Gravitational lensing shear by demagnifying lens model

It was shown [36], in the weak field and thin lens approximations, that images due to lens models for the gravitational pull on light rays are tangentially elongated, whereas those by the other models for the gravitational repulsion on light rays are always radially distorted. As a cosmological implication, it is suggested that cosmic voids might correspond to the parameters $\kappa < 0$ and $\varepsilon < 0$, and hence they could produce radially elongated images. So that, gravitational lensing shear measurements would be another tool for studying voids. Lens objects cannot be directly seen except for visible lens objects such as galaxies. Exotic lens models, that are discussed in this section might be invisible. In the following calculations, the origin of the two-dimensional coordinates is chosen as the center of the lens object. The radial and tangential directions can be well defined. For a pair of radially elongated images ($\varepsilon < 0$), they are in alignment with each other. For a pair of tangentially elongated images ($\varepsilon > 0$), they are parallel with each other. But, one can distinguish radial elongation from tangential one by measuring such an image alignment in observations.

From the standard lens theory [19], it is possible to derive that the deflection angle of light (Eq. (3.5)) corresponds to a convergence (scaled surface mass density)

$$\kappa(b) = \frac{\bar{\varepsilon}(1-n)}{2}\frac{1}{b^{n+1}}. \tag{3.14}$$

According to the last equation, the sign of the convergence κ is the same as that of $\varepsilon(1-n)$. Note that the convergence vanishes when $n = 1$, i.e. for the weak-field Schwarzschild case. As we have seen in the previous section, for $\varepsilon > 0$ and $n > 1$, the effective surface mass density of the lens object is interpreted as negative in the framework of the standard lens theory: the matter and therefore the energy need to be exotic. Also when $\varepsilon < 0$ and $n < 1$, the convergence is negative, and matter (and energy) need to be exotic. If $\varepsilon < 0$ and $n > 1$, the convergence is positive everywhere except for the central singularity and in this case exotic matter are not required in the framework of the standard lens theory. For $\varepsilon > 0$, Eq. (3.6) has always positive root corresponding to the Einstein ring for $\beta = 0$. The Einstein ring radius is defined as [33]

$$\theta_E \equiv \left(\frac{\bar{\varepsilon} D_{LS}}{D_S D_L^n}\right)^{\frac{1}{n+1}}. \tag{3.15}$$

If $\varepsilon < 0$, there is no positive root for $\beta = 0$. In fact this case describes the repulsive force. Anyway it is possible to define the Einstein ring radius for $\varepsilon < 0$ as

$$\theta_E \equiv \left(\frac{|\bar{\varepsilon}| D_{LS}}{D_S D_L^n} \right)^{\frac{1}{n+1}} \tag{3.16}$$

that gives a typical angular size for these lenses. Now we discuss about the $\varepsilon > 0$ case. Eqs. (3.7) and (3.8) can be rewritten in the vectorial form as

$$\hat{\boldsymbol{\beta}} = \hat{\boldsymbol{\theta}} - \frac{\hat{\boldsymbol{\theta}}}{\hat{\theta}^{n+1}} \qquad (\hat{\theta} > 0) \tag{3.17}$$

$$\hat{\boldsymbol{\beta}} = \hat{\boldsymbol{\theta}} - \frac{\hat{\boldsymbol{\theta}}}{(-\hat{\theta})^{n+1}} \quad (\hat{\theta} < 0). \tag{3.18}$$

There is always one image for $\hat{\theta} > 0$ and the other image appears for $\hat{\theta} < 0$. The lensing shear is generally defined through the magnification matrix $A_{ij} \equiv \partial\beta^i / \partial\theta_j$ [19]. The magnification matrix for $\theta > 0$ can be diagonalized by using its eigenvalues as

$$\begin{aligned} (A_{ij}) &= \begin{pmatrix} 1 - \kappa - \gamma & 0 \\ 0 & 1 - \kappa + \gamma \end{pmatrix} \\ &\equiv \begin{pmatrix} \lambda_- & 0 \\ 0 & \lambda_+ \end{pmatrix}. \end{aligned} \tag{3.19}$$

Here the x and y coordinates are chosen along the radial and tangential directions and then, $(\hat{\theta}_i) = (\theta, 0)$ and $(\hat{\beta}_i) = (\beta, 0)$. The radial elongation factor is $1/\lambda_-$ and the tangential one, $1/\lambda_+$. The primary image ($\hat{\theta} > 0$) has eigenvalues (Eq. (3.17))

$$\lambda_+ = \frac{\hat{\beta}}{\hat{\theta}} = 1 - \frac{1}{\hat{\theta}^{n+1}} \tag{3.20}$$

$$\lambda_- = \frac{d\hat{\beta}}{d\hat{\theta}} = 1 + \frac{n}{\hat{\theta}^{n+1}}. \tag{3.21}$$

If and only if $n > -1$, one can show $\lambda_- > \lambda_+$, hence the primary image is always tangentially elongated. From Eqs. (3.20) and (3.21), the convergence

and the shear take the form

$$\begin{aligned} \kappa &= 1 - \frac{\lambda_+ + \lambda_-}{2} \\ &= \frac{1-n}{2}\frac{1}{\hat{\theta}^{n+1}}, \end{aligned} \tag{3.22}$$

$$\begin{aligned} \gamma &= \frac{\lambda_+ - \lambda_-}{2} \\ &= -\frac{1+n}{2}\frac{1}{\hat{\theta}^{n+1}}. \end{aligned} \tag{3.23}$$

Notice that $n = 1$, corresponding to the Schwarzschild lens, leads to $\kappa = 0$. By using Eq. (3.18) one can show that also the secondary image ($\hat{\theta} < 0$) is tangentially elongated. In fact, if and only if $n > -1$, $\lambda_- > \lambda_+$. After an expansion of Eqs. (3.20) and (3.21) around the Einstein ring ($\hat{\theta} \sim 1$), it is possible to show that the arc shape appearing near $\hat{\theta} \sim 1$ depends on n as

$$\frac{\lambda_-}{\lambda_+} = \frac{1}{\hat{\theta} - 1} + \left(1 - \frac{n}{2}\right) + O(\hat{\theta} - 1). \tag{3.24}$$

Then, for a given observed lens position $\hat{\theta}$, the elongation of images becomes weaker when n becomes larger. This is also true for the secondary image.
For $\varepsilon < 0$ case, Eq. (3.6), in the units of the Einstein ring radius can be rewritten as

$$\hat{\boldsymbol{\beta}} = \hat{\boldsymbol{\theta}} + \frac{\hat{\boldsymbol{\theta}}}{\hat{\theta}^{n+1}} \qquad (\hat{\theta} > 0) \tag{3.25}$$

$$\hat{\boldsymbol{\beta}} = \hat{\boldsymbol{\theta}} + \frac{\hat{\boldsymbol{\theta}}}{(-\hat{\theta})^{n+1}} \quad (\hat{\theta} < 0). \tag{3.26}$$

Assuming that $\hat{\beta} > 0$, Eq. (3.25) has at most two positive root, instead Eq. (3.26) has no root satisfying $\hat{\theta} < 0$. For a large impact parameter there are two images on the same side with respect to the lens position, while for small impact parameter no image appears. The two images can be studied by using Eq. (3.25) such that

$$\lambda_+ = \frac{\hat{\beta}}{\hat{\theta}} = 1 + \frac{1}{\hat{\theta}^{n+1}} \tag{3.27}$$

$$\lambda_- = \frac{d\hat{\beta}}{d\hat{\theta}} = 1 - \frac{n}{\hat{\theta}^{n+1}}. \tag{3.28}$$

If and only if $n > 1$, $\lambda_- < \lambda_+$: both images are everywhere radially elongated. Figure 3.3 shows κ and $\lambda_\pm$ numerically calculated for $n = 0.5, 1, 2$ and 3.

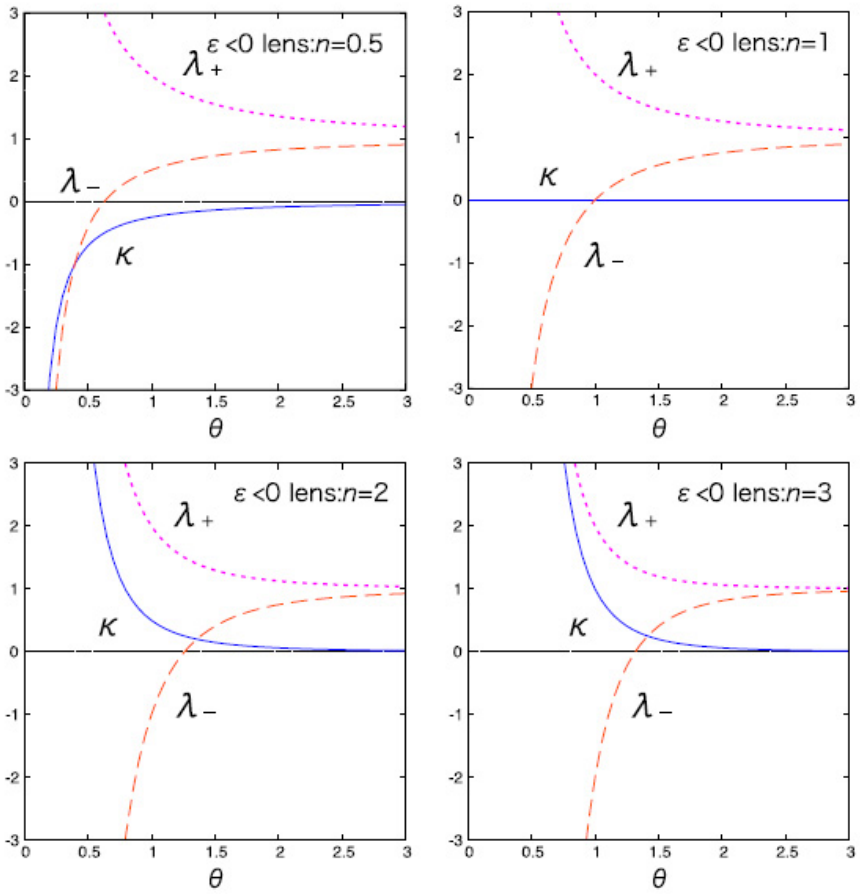

Figure 3.3: κ, λ_+ and λ_- for $\varepsilon < 0$.They are denoted by solid (blue in colors), dotted (purple in colors) and dashed (red in colors) curves, respectively. The horizontal axis denotes the image position θ in the units of the Einstein radius. Top left: $n = 0.5$. Top right: $n = 1$. Bottom left: $n = 2$. Bottom right:$n = 3$. Izumi et al. [36]

The convergence is negative for $n = 0.5$ and positive for $n = 2, 3$. Then, $n = 1$ corresponding to the negative-mass Schwarzschild lens leads to $\kappa = 0$. For these four cases λ_+ is always larger then λ_-. It is possibile to calculate the shear by using Eqs. (3.27) and (3.28)

$$\begin{aligned} \gamma &= \frac{\lambda_+ - \lambda_-}{2} \\ &= \frac{1+n}{2}\frac{1}{\hat{\theta}^{n+1}} \end{aligned} \tag{3.29}$$

A repulsive case might correspond to the lensing by a void-like mass distribution. As a cosmological implication, the present model with $\kappa < 0$ might correspond to an underdense region called a cosmic void. The cosmic void is characterized by a local mass density below the cosmic mean density and then, the density contrast is negative. The gravitational force on the light rays by the surrounding region could be interpreted as repulsive ($\varepsilon < 0$). In fact, the bending angle of light with respect to the center of the spherical void might be negative. Notice that the positive convergence due to the cosmic mean density is taken into account in the definition of the cosmological distances.

As we have seen (Eq. (3.14)) Izumi et al. found a relation between convergence and energy. It is interesting to show now what Bozza and Postiglione [14] got on the convergence in connection with energy-momentum tensor components. Let us introduce the metric [33]

$$ds^2 = \left(1 - \frac{\alpha}{r^n}\right)c^2dt^2 - \left(1 + \frac{\gamma}{r^n}\right)\left(dr^2 - r^2d\theta^2 + \sin^2\theta d\phi^2\right), \tag{3.30}$$

depending on the coefficients α and γ. As shown in Ref. [14], in order to support such a metric, Einstein equations require precise relations between these coefficients and the energy-momentum tensor components. In particular, we recall that the exponent n only depends on the ratio between tangential and radial pressure $n = -2p_t/p_r$. The deflection of light in such a metric was first studied by Kitamura et al. [33]. They find

$$\hat{\alpha} = \frac{\sqrt{\pi}\Gamma[(1+n)/2]}{\Gamma[n/2]}\frac{\alpha+\gamma}{u^n}, \tag{3.31}$$

where $\Gamma[z]$ is the Euler gamma function and u is the impact parameter of the light ray. They also derived the so-colled convergence, defined as

$$\kappa = \frac{1}{2}\nabla\cdot\hat{\vec{\alpha}}, \tag{3.32}$$

where $\hat{\vec{\alpha}} \equiv \hat{\alpha}\vec{x}/u$ is the vectorial form of the deflection taking into account its direction on the planr orthogonal to the line of sight ($u = |\vec{x}|$ is the impact parameter). Using Eq. (3.31) Bozza and Postiglione [14] obtain

$$\kappa = \frac{\sqrt{\pi}\Gamma[(1+n)/2]}{\Gamma[n/2]} \frac{(1-n)(\alpha+\gamma)}{u^{n+1}} \tag{3.33}$$

which matches the result of Ref. [33].

In standard gravitational lensing, convergence is proportional to the mass density projected along the line of sight $\int \rho dz$. Kitamura et al. note that $n > 1$ and attractive deflection ($\alpha + \gamma > 0$) imply a negative mass density and then that exotic matter is needed. Bozza and Postiglione also establish a firmer bond between convergence and energy-momentum tensor components. They get (see section 1.6 for coordinates and ansatz)

$$\begin{aligned} \kappa &= \frac{\alpha_G}{2} \int dz (T^t_t - T^z_z) \\ &= \frac{\lambda_G}{2} \int dz \left[\rho + p_t + (p_r + p_t) \frac{z^2}{u^2 + z^2} \right] \end{aligned} \tag{3.34}$$

where $\lambda_G = 8\pi G/c^4$ is the gravitational coupling constant. As we can see gravitational lensing is not only sensitive to the mass, but also to the pressure of the sources. Light rays feel the energy density and the longitudinal pressure encountered along their path. In order to have the integral of the last equation negative, i.e. negative convergence, there must be at least some region with $\rho + p_z < 0$. This is a clear violation of the weak energy condition. In addition the authors of Ref. [14] note that a negative convergence is equivalent to a violation of strong energy condition (see Eqs. (3.33) and (1.69)).

Finally, starting from the eigenvalues written in Eqs. (3.27) and (3.28), it is possible to show [37] what happens to the total magnification in the limit $\beta \gg \theta_E$. We can write the lens equation as

$$\beta = \theta - \frac{\theta_E^{n+1}}{|\theta|^n} \mathrm{Sign}(\theta), \tag{3.35}$$

where β is the source angular position with respect to the center of the lens, $\theta = u/D_L$ is the angular position at which the observer observes the image and the modified angular Einstein radius reads

$$\theta_E = \left[\frac{D_{LS}}{D_L^n D_S} \frac{\sqrt{\pi}\Gamma[(1+n)/2]\,(\alpha+\gamma)}{\Gamma[n/2]} \right]^{1/(n+1)}. \tag{3.36}$$

For $n > 0$ there are still two real images, whose position can be calculated numerically. In the limit $\beta \gg \theta_E$, the primary image is in $\theta_+ \simeq \beta$ and the secondary image is in $\theta_- \simeq -(\theta_E^{n+1}/\beta)^{1/n}$. In the singular isothermal sphere ($n = 0$), the secondary image can only exist when the source is within the Einstein radius $\beta < \theta_E$. The emergence of a single image from the crossing of the Einstein ring clearly violates the theorems on the number of images. This is a consequence of the presence of the central singularity.
The radial and tangential magnifications are respectively given by

$$\mu_r = \left(\frac{\partial\beta}{\partial\theta}\right)^{-1} = \left(1 + n\frac{\theta_E^{n+1}}{\theta^{n+1}}\right)^{-1} \tag{3.37}$$

$$\mu_t = \frac{\theta}{\beta} = \left(1 - \frac{\theta_E^{n+1}}{\theta^{n+1}}\right)^{-1}, \tag{3.38}$$

with the total magnification given by $\mu = \mu_r\mu_t$. As noted in Ref. [33], for $n > 1$ there always exists some value of β leading to a total magnification smaller than one (defocusing). This can be simply obtained by an expansion of μ for $\theta \simeq \beta \gg \theta_E$ and neglecting the contribution by the secondary image:

$$\mu \to 1 + (1-n)\left(\frac{\theta_E}{\beta}\right)^{n+1} + (1 - n + n^2)\left(\frac{\theta_E}{\beta}\right)^{2n+2} + o\left(\frac{\theta_E}{\beta}\right)^{2n+2}. \tag{3.39}$$

The first deviation from unity is negative for any $n > 1$. For the Schwarzschild case, the leading deviation is the second order, scaling as β^{-4} as well known. In practice, images created by exotic lenses are as extended as Schwarzschild ones tangentially, but are more compressed on the radial direction. While the two deformations compensate at first order in Schwarzschild, this no longer happens for exotic lenses. For what concerns ordinary matter distributions ($n < 1$), the situation is reversed, with a radial compression that is smaller than in the Schwarzschild case, allowing a higher total magnification emerging at the $1/\beta^2$ level already.

3.3 Observational upper bound from SQLS

Although there are a lot of theoretical works concerning negative-mass objects and the Ellis wormhole, observational studies have been very rare. This is mainly due to the repulsive force by negative mass and Ellis wormhole and to the no matter accretion result. Then it is unlikely to directly see them as luminous objects. That's why today gravitational lensing has attracted interest as an observational tool to probe such exotic dark objects. In this section we report the results obtained by Takahashi and Asada [40] about the

upper bound on the cosmic abundances of the negative-mass compact object and the Ellis wormhole using the quasar lens sample in the Sloan Digital Sky Survey Quasar Lens Search (SQLS) data based on SDSS II. They employ the unit $G = c = 1$ and use the cosmological parameters of the Hubble constant $h = 0.7$, the matter density $\Omega_m = 0.28$, and the cosmological constant $\Omega_\Lambda = 0.72$, which is in concordance with the latest *Wilkinson Microwave Anisotropy Probe* results [41]. For negative-mass compact object case, they obtain a relation between the typical lens mass and the image angular separation (see Eq. (2.14)) as

$$|M| \simeq 1 \times 10^{11} h^{-1} M_\odot (\theta_E/1'')^2 [(D_L D_S/D_{LS})/1h^{-1}Gpc]. \tag{3.40}$$

As a result, the sensitive mass range is $|M| = (10^{11} - 10^{14})M_\odot$ for the image separation of $1'' - 20''$.
As we have seen in the first chapter, the Ellis Wormhole is characterized by one parameter as its throat radius a and the line element takes the form

$$ds^2 = dt^2 - dr^2 - (r^2 + a^2)(d\theta^2 + sin^2\theta d\phi^2). \tag{3.41}$$

For Ellis wormholes, the lens equation in the weak field approximation becomes

$$\beta = \theta - \theta_E^3 \frac{\theta}{|\theta|^3} \tag{3.42}$$

with the Einstein angular radius

$$\theta_E = \left(\frac{\pi a^2}{4} \frac{D_{LS}}{D_L^2 D_S} \right)^{1/3}. \tag{3.43}$$

The two images form at the angular positions

$$x_\pm^{-1} = \pm \sqrt[3]{1/2 + \sqrt{1/4 \pm y^3/27}} - \sqrt[3]{\mp 1/2 \pm \sqrt{1/4 \pm y^3/27}} \tag{3.44}$$

where $x_\pm = \theta_\pm/\theta_E$ and $y = \beta/\theta_E$ [42]. The magnification for each image is

$$\mu_\pm = |(1 \mp x_\pm^{-3})(2x_\pm^{-3} \pm 1)|^{-1}. \tag{3.45}$$

The typical throat radius for a given θ_E (see Eq. (3.43)) is estimated as

$$a \simeq 10 h^{-1} pc (\theta_E/1'')^{3/2} [(D_L^2 D_S/D_{LS})/(1h^{-1}Gpc)^2]^{1/2}. \tag{3.46}$$

The sensitive throat radius falls in the range, $a = (10 - 100)pc$ from the image separation of $1'' - 20''$. The throat radius is much smaller than the corresponding Einstein ring radius

$$R_E = \theta_E \times D_L \sim 10 kpc (\theta_E/1'')(D_L/1h^{-1}Gpc). \tag{3.47}$$

This means that the range of the radius is slightly wider, since the lensing effects are dependent also on distance ratios.
The latest result in SQLS has set the first cosmological constraints on negative-mass compact objects and Ellis wormholes. There are no multiple images lensed by the above two exotic objects for ~ 50000 distant quasars in the SQLS data. But, an upper bound is put on the cosmic abundances of these lenses. Figures 3.4 and 3.5 show the current upper bound on the cosmological number of the negative-mass compact objects and on the Ellis wormhole, respectively. The vertical axis in Figure 3.4 is the number density $n(h^3 Mpc^{-3})$ and the horizontal one, the absolute value of the mass $|M|(h^{-1}M_\odot)$. The two curves are the upper bounds at 68% and 95% confidence levels. For $|M| > 10^{14}(10^{12})M_\odot$, the number density is less than $n < 10^{-7}(10^{-5})h^3 Mpc^{-3}$. The blue dashed lines denote the absolute value of the cosmological density parameter for the negative mass, $|\Omega| = 10^{-4}, 10^{-2}$ and 1. The density parameter is defined as the mass density divided by the cosmological critical density, $\Omega = Mn/\rho_{cr}$. For galactic and cluster mass scale $|M| = (10^{12} - 10^{15})M_\odot$, the density parameter is less than $\Omega < 10^{-4}$. Then the negative-mass compact object is less abundant than the galaxy with typical luminosity $L^*(n_{gal} \approx 10^{-2} Mpc^{-3})$ and the galaxy cluster with typical mass $10^{14}M_\odot$ ($n_{clust} \approx 10^{-4} Mpc^{-3}$), which correspond to $\Omega_{gal} \approx 0.2$ for the galaxies and $\Omega_{clust} \approx 0.3$ for the clusters [43].
The horizontal axis of Figure 3.5 is the throat radius $a(h^{-1}pc)$. For $a = (10 - 10^4)pc$, the number density is $n < 10^{-4}h^3 Mpc^{-3}$. The Ellis wormhole with $a = (0.1 - 10^5)pc$ is much less abundant than a star ($n_{star} \approx 10^{10} Mpc^{-3}$). The upper-bound curves approach straight lines for very small $a(\ll 0.1pc)$ or large $a(\gg 10^4 pc)$. In the case of a very small a, the lens is very close to us since $a \propto D_L$ from Eq. (3.43) under the fixed θ_E and D_S, while the lens for a very large a is very close to the source since $a \propto D_{LS}^{-1/2}$ from Eq. (3.43).

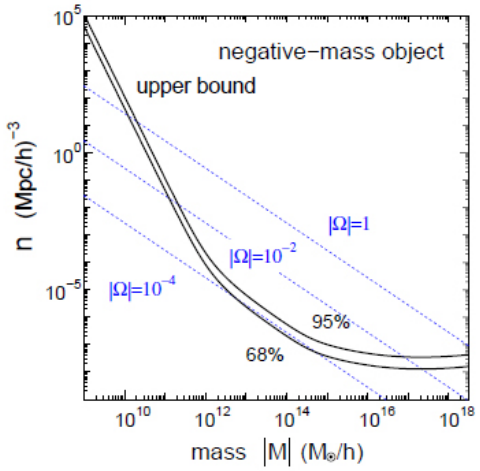

Figure 3.4: Upper bound on the cosmological number density of negative-mass compact objects. The vertical axis denotes the density n ($h^3 Mpc^{-3}$). The horizontal axis denotes the absolute value of the mass $|M|$ ($h^{-1}M_\odot$). The two solid curves correspond to upper bounds of 68% and 95% confidence levels. The blue dashed lines denote the absolute value of the cosmological density parameter for the negative mass, $|\Omega| = 10^{-4}, 10^{-2}$ and 1. Takahashi and Asada [40]

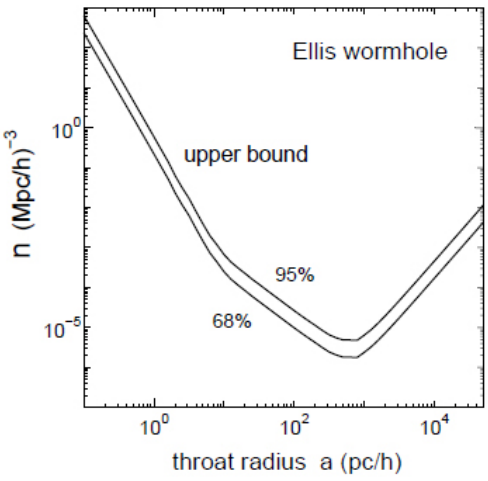

Figure 3.5: Same as Fig., but for the Ellis wormhole. The horizontal axis is the throat radius a ($h^{-1}pc$) Takahashi and Asada [40]

Chapter 4

Caustics of $1/r^n$ binary gravitational lenses: galactic haloes and exotic matter under the same model

4.1 Gravitational lensing by non-Schwarzschild objects

With all these recent studies motivating further investigation on the observational properties of non-Schwarzschild metrics, with the present work we aim at extending the existing gravitational lensing theory for $1/r^n$ metrics developed in Refs. [33, 34] to the binary case. Indeed, the defocusing property common to such metrics and the non-trivial structure of the Jacobian matrix found in the single-lens case incites to make the leap to a case in which the spherical symmetry is broken and the critical structure of the lens map becomes non-trivial. Do the caustics in an exotic binary lens have any resemblance to the standard Schwarzschild case? Is the number of images the same? Do we find any new mathematical features that cannot be reproduced in the standard case? There are many ways to break the spherical symmetry. We can consider the rotation of the source distribution [69], the presence of an external shear [70], a binary system composed of a normal star orbiting an exotic object or a binary system composed of two exotic condensates. Indeed, any of these routes require its own amount of work, so, as a first case study, we have decided to focus on the binary system composed of two exotic objects. This kind of system has the advantage of being mathematically simpler than the mixed case (normal star - exotic object) since the two

deflection terms come with the same power of the impact parameters. The absence of any standard terms in the lens equation also ensures that any new phenomena can be ascribed to the $1/r^n$ gravity without any contamination from other terms. So, it represents an ideal case in which we can explore a fully developed non-trivial caustic structure generated in a genuine $1/r^n$ framework. Besides mathematics, an astrophysical motivation for studying binary wormholes or $1/r^n$ objects comes from studies of dynamical formation of wormholes from an initial scalar field configuration [71]. It is likely that local inhomogeneities in this field may cause the formation of multiple objects in the same way as a gas cloud collapses by Jeans instability generating stellar clusters. So, a wide-range investigation of exotic objects should take into account the possibility that they form in binaries or clusters. The standard binary lens caustic structure has been studied by Schneider and Weiss [32] and by Erdl and Schneider [72]. They showed that, depending on the projected distance between the two components, three different topology regimes exist. Interesting results on the magnification pattern were obtained by Witt and Mao [73] and Asada [74]. Getting more closely to our work, Shin and Evans discussed the critical curves and caustics of isothermal haloes with and without a regular core [31]. Notably, the singular isothermal sphere provides a limiting case for the $1/r^n$ objects obtained for $n \to 0$. Gravitational potentials with $n < 1$ characterize dust (non-relativistic matter) distributions whose 3-dimensional density profile falls as $1/r^{n+2}$. Since haloes of galaxies may have different profiles depending on the amount of dark matter they contain, our study has interesting applications to lensing by galaxy systems. We may e.g. consider the gravitational lens formed by two galaxies with spheroidal haloes declining as $1/r^{n+2}$. The structure of critical curves and caustics is obviously a function of the exponent n. A complete understanding of these mathematical curves in different regimes may help modelling these systems and fix the slope parameter in real astrophysical cases. This would be useful to extend existing catalogues of unusual gravitational lenses [75] beyond the basic isothermal profile. In definitive, we will have two regimes for our investigation of binary $1/r^n$ objects: $n < 1$ corresponding to galactic haloes, $n > 1$ corresponding to exotic objects violating energy conditions. The familiar Schwarzschild metric comes with $n = 1$ and represents the divider between these two very different classes. As we have seen, light deflection is sensitive both to the energy density and the pressure, which is non-negligible in our case. So, when introducing the binary lens case, we will not refer to a "mass ratio" between the two components, but rather to a "strength ratio". This terminology perfectly applies to the ordinary matter $n < 1$ case, where the coefficients are determined by the local density normalizations rather than the total masses of the haloes.

From the lens equation introduced in Eq. (3.35) we note that when the source is perfectly aligned behind the lens ($\beta = 0$), the image coincides with the only tangential critical curve, the Einstein ring with radius θ_E. So, the caustic structure of the single $1/r^n$ lens is analogous to its standard cousin: one tangential critical curve corresponding to the degenerate caustic point in the origin. There are no radial critical curves in the $1/r^n$ lenses studied in this work. In the singular isothermal sphere ($n = 0$), actually the circle with radius θ_E divides the source plane in a region where we have a single image and an internal region in which we have two images. The name pseudo-caustic has been proposed [77, 31] for the curve with radius θ_E. This pseudo-caustic becomes a real radial caustic whenever we allow for a central regular core, where a third highly-demagnified image can live. It is interesting to note that the angular Einstein radius in the standard Schwarzschild lens scales as the square root of the mass. So, if one changes the mass by a factor q, the Einstein radius scales as $\sqrt{q}$. In the general $1/r^n$ case, if one changes the energy-momentum distribution by scaling it by a factor q, the deflection angle at a fixed impact parameter scales as q, but the Einstein radius scales as $q^{1/(n+1)}$, which recovers the Schwarzschild limit for $n = 1$. This difference has another interesting consequence: while the area of the critical curve is directly proportional to the mass in the Schwarzschild case, this is not true for non-Schwarzschild objects. The area enclosed in the critical curve grows more slowly with the lens strength.

4.2 Binary lenses

Now let us consider a lensing system composed of two objects whose gravitational potential asymptotically falls as $1/r^n$, whether ordinary ($n < 1$) or exotic ($n > 1$). If the two objects are gravitationally bound, the distribution of the matter-source supporting either object would be warped by the presence of the partner. The resulting distribution could only be obtained by a consistent resolution of the Einstein equations with the hydrodynamical equations of the source. We have no intention to tackle such a complicated problem, since our focus is on all possible new effects on the gravitational lensing sector. So, the only case in which we can consider the total light deflection as the sum of the contributions given by the two isolated objects arises when the two objects stand far apart along the line of sight but perspectivally close enough so as to affect the light trajectory by their peculiar gravitational potential. On the other hand, if we do not want to tangle with multiple plane deflection issues [47, 78, 79], we must still require that the distance between the pair of lenses is much smaller than the source-lens

and lens-observer distances. The mixed case, with a star orbiting the exotic object is probably more physically appealing, but more complicated mathematically. Our study intends to climb a clear and simple first step in this topic.
We then consider two non-Schwarzschild objects A and B whose reduced deflection angles are given by

$$\alpha_{A,B}(\vec{\theta}) = \epsilon_{A,B}\theta_E^{n+1}\frac{\left(\vec{\theta}-\vec{\theta}_{A,B}\right)}{|\vec{\theta}-\vec{\theta}_{A,B}|^{n+1}}. \tag{4.1}$$

The coordinates in the sky of the two objects are $\vec{\theta}_{A,B}$, the deflection strengths depend on the gravitational potentials of the two objects through Eq. (3.31). Setting $\epsilon_A + \epsilon_B = 1$, the strength ratio is $q \equiv \epsilon_A/\epsilon_B$, while the order of magnitude of the deflection is set by the angular scale θ_E. This corresponds to the angular radius of the Einstein ring of an isolated object with $\epsilon_i = 1$. As emphasized before, for each object, this radius scales with ϵ_i^{n+1}. At this point, we can write down the lens equation taking these two contributions into account

$$\vec{\beta} = \vec{\theta} - \epsilon_A\theta_E^{n+1}\frac{\left(\vec{\theta}-\vec{\theta}_A\right)}{|\vec{\theta}-\vec{\theta}_A|^{n+1}} - \epsilon_B\theta_E^{n+1}\frac{\left(\vec{\theta}-\vec{\theta}_B\right)}{|\vec{\theta}-\vec{\theta}_B|^{n+1}}. \tag{4.2}$$

For the ordinary binary lens equation ($n = 1$) it is very useful to introduce complex coordinates, as first envisaged by Witt [48]. We do the same in the generic power n case as follows

$$\zeta = \frac{\beta_1 + i\beta_2}{\theta_E}; \quad z = \frac{\theta_1 + i\theta_2}{\theta_E}. \tag{4.3}$$

For simplicity, we take the origin of coordinates at the mid-point between the two lenses $z_A = -z_B$ with the real axis along the line joining the lenses. We call the normalized angular separation between the lenses s, so that we can set $z_A = -s/2$ and $z_B = s/2$. Then the lens equation (4.2) can be written as

$$\zeta = z - \frac{\epsilon_A}{(z+s/2)^{\frac{n-1}{2}}(\bar{z}+s/2)^{\frac{n+1}{2}}} - \frac{\epsilon_B}{(z-s/2)^{\frac{n-1}{2}}(\bar{z}-s/2)^{\frac{n+1}{2}}}. \tag{4.4}$$

The fortunate simplification that removes z from the deflection terms only occurs for $n = 1$. Its presence in the general case severely complicates the Jacobian determinant of the lens map, which in complex notations is given by

$$J(z,\bar{z}) = \left|\frac{\partial\zeta}{\partial z}\right|^2 - \left|\frac{\partial\zeta}{\partial\bar{z}}\right|^2. \tag{4.5}$$

In fact, the first term, which was just unity in the Schwarzschild case, now becomes as involved as the second. In detail, the Jacobian is

$$J = \left\{1+\frac{n-1}{2}\left[\frac{\epsilon_A}{(z+s/2)^{\frac{n+1}{2}}(\bar{z}+s/2)^{\frac{n+1}{2}}}+\frac{\epsilon_B}{(z-s/2)^{\frac{n+1}{2}}(\bar{z}-s/2)^{\frac{n+1}{2}}}\right]\right\}^2 - \frac{(n+1)^2}{4}\left|\frac{\epsilon_A}{(z+s/2)^{\frac{n+3}{2}}(\bar{z}+s/2)^{\frac{n-1}{2}}}+\frac{\epsilon_B}{(z-s/2)^{\frac{n+3}{2}}(\bar{z}-s/2)^{\frac{n-1}{2}}}\right|^2 \quad (4.6)$$

The critical curves of a lens model are defined by the condition $J(z) = 0$ [49]. Creation/destruction of the images can only occur on such points. The corresponding points on the source plane, found by applying the lens map, form the caustic curves. Caustic curves bound regions in which a source gives rise to an additional pair of images. A source on a caustic point produces (at least) two degenerate images on the corresponding critical point. For all these properties, critical curves and caustics are generally sufficient to understand the qualitative behavior of a lens system. They are widely used for the interpretation of observations in all applications of gravitational lensing. Our goal, achieved in the following sections, is a full numerical and analytical exploration of critical curves and caustics of the generalized binary lens with deflections falling as $1/u^n$.

4.3 Numerical exploration of Critical curves and Caustics

We start from the symmetric equal-strength case and then move to the asymmetric strength case. Following the notation introduced in the previous section, we assume that the centers of the two lenses lie on the real axis (using complex notations) and we choose the origin half-way between the two lenses. The unit of measure is θ_E, i.e. the angular radius of the Einstein ring that we would obtain for an isolated object with strength $\epsilon = 1$. The strengths ratio of the two object is $q = \epsilon_A/\epsilon_B$ and their separation in units of θ_E is s. In order to show the evolution from $n = 1$ to higher values of n, we decided to plot the critical curves and caustics for $n = 0, 0.5, 1, 2, 3$. $n = 1$ corresponds to two ordinary Schwarzschild lenses [32, 72], while $n = 2$ corresponds to two Ellis wormholes. A generic value of n can be obtained in other cases, as explained e.g. in Ref. [14]. On the other side, galactic haloes can be obtained with this model in the range $0 < n < 1$, with the singular isothermal sphere being the limit $n = 0$. The technique used to obtain the critical curve is accurate contouring of the Jacobian determinant using

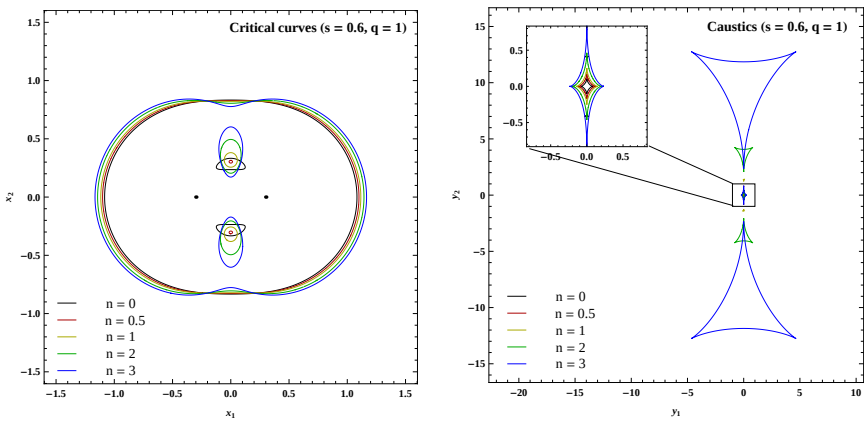

Figure 4.1: Equal-strength binary. Close separation

`Mathematica`. The contours are then mapped through the lens equation to obtain the corresponding caustics in the source plane.

4.3.1 Equal-strength binary $q = 1$

In the standard Schwarzschild binary lens, it is well-known that three topologies exist, depending on the separation of the two masses [32, 72]. The close topology is obtained for $s < 1/\sqrt{2}$. It consists of a primary 4-cusped caustic at the barycenter of the system generated by the common critical curve enveloping the whole lens and a pair of small triangular caustics generated by two symmetrical critical ovals close to the lenses containing local maxima of the Jacobian. The intermediate topology exists in the range $1/\sqrt{2} < s < 2$ and is characterized by a single 6-cusped caustic obtained when the two secondary caustics of the close topology merge with the primary one removing two pairs of cusps by a beak-to-beak singularity. Finally, the wide topology for $s > 2$ emerges when the intermediate caustic splits into two 4-cusped astroids along the lens axis; the two astroids become smaller and smaller while the two critical curves tend to the Einstein rings of the two isolated objects. For the singular isothermal sphere, the same topologies are found [31], but with important additional features in the close regime. In fact, the small ovals shrink to zero size at finite separation s and then grow to finite size again (this singularity is called elliptic umbilic). Finally, these ovals touch the two singular lenses, giving rise to degenerate caustics. We always find the same three topology regimes in the generic n case, nicely joining and generalizing the two known limits, but with notable differences in the sizes and the shapes of critical curves and caustics, which can be heavily deformed with respect to the known limits. In Fig. 4.1 we show the critical curves and

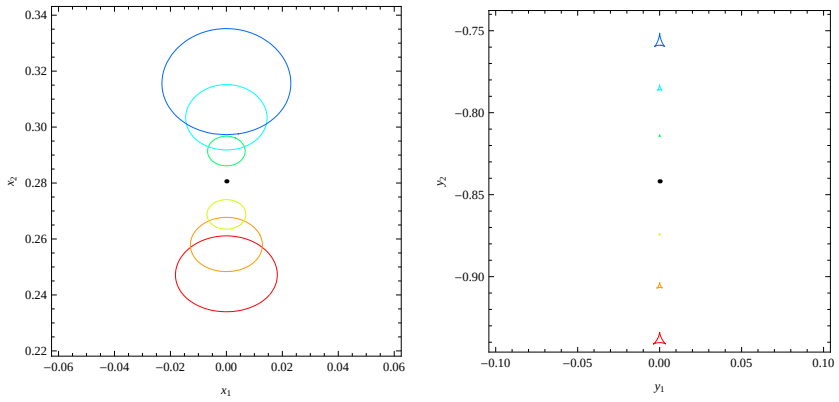

Figure 4.2: The elliptic umbilic catastrophe shown for $n = 0.5$ and separations growing from $s = 0.5$ to $s = 0.62$ in steps of 0.02 from red to blue. The elliptic umbilic occurs at $s = 0.56$.

caustics for $s = 0.6$, which is in the close regime for all values of n chosen. In the standard $n = 1$ case, the close topology features three critical curves, one resembling the Einstein ring of the lens obtained by summing the two masses and two smaller critical curves inside the main one. Correspondingly, there is a central astroidal caustic generated by the main critical curve and two triangular caustics corresponding to the small critical curves. For the singular isothermal sphere ($n = 0$), the two secondary critical curves become tangentially elongated and the two caustics become smaller and closer to the primary one. As anticipated, for separations closer than $s = 0.25$, the two critical curves reach the two lenses, and the secondary caustics merge with the circular pseudo-caustics [31]. The singular isothermal sphere represents a limiting case for our analysis. Indeed, this degenerate behavior is only found for n exactly equal to 0, but for any $n > 0$ the critical curves never touch the lenses. On the other hand, we find that the elliptic umbilic catastrophe distinguishing the singular isothermal sphere from the Schwarzschild case is present in the whole range $0 \leq n < 1$. Since this feature is particularly difficult to catch in general plots, in Fig. 4.2 we propose a sequence of critical curves and caustics at fixed $n = 0.5$ and growing separations. From $s = 0.5$ to $s = 0.56$ the oval (and so the corresponding caustic) shrinks to zero size and then from $s = 0.56$ to $s = 0.62$ it opens up again. We will come back to the description of this elliptic umbilic in the next section. Moving from 1 to higher n values, we still see the same three critical curves, but the inner ones are severely elongated in the radial direction opposite to the barycenter of the system. In the caustics, this difference causes the formerly small

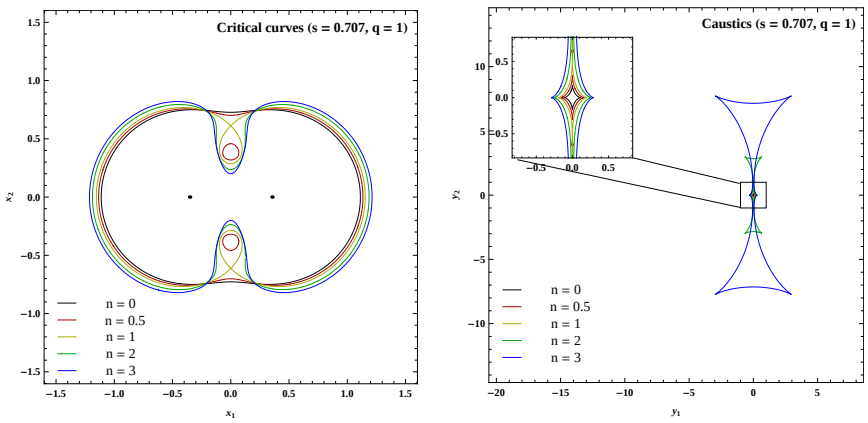

Figure 4.3: Equal-strength binary. Close-intermediate transition

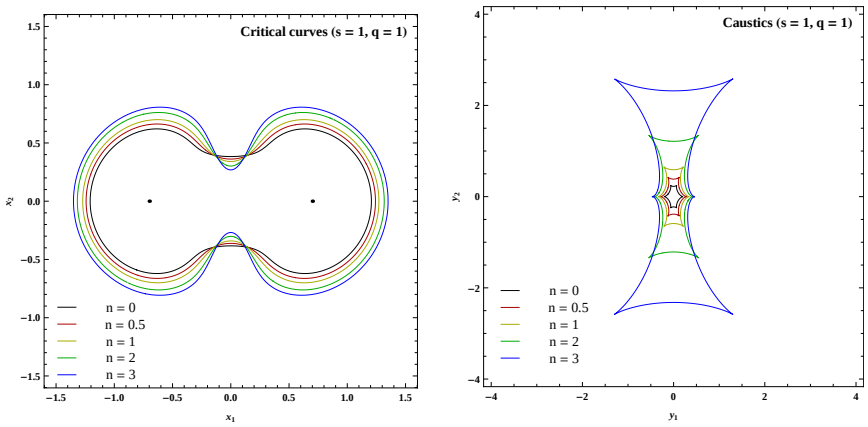

Figure 4.4: Equal-strength binary. Intermediate separation

triangular caustics to become bigger and bigger, quickly becoming huge in size (note the scale of the right panel of Fig. 4.4). The consequence of this difference is that it is much easier for exotic lenses to have a source inside one of these giant caustics and then have two additional images close to the corresponding critical curve. We can imagine that the strong elongation of the inner critical curves will cause the transition from the close to the intermediate regime to occur earlier than in the standard $n = 1$ case. Indeed, this is what happens. In fact, in Fig. 4.3 we have chosen $s = 1/\sqrt{2}$ to pick up the transition in the $n = 1$ case. At this separation, both the $n = 2$ and $n = 3$ critical curves are already in the intermediate regime, with one single dumbbell-shaped curve and a corresponding 6-cusped caustic. Still the size of these intermediate caustics is much larger than in the standard case. Conversely, the $n < 1$ caustics are still in the close regime. The extension

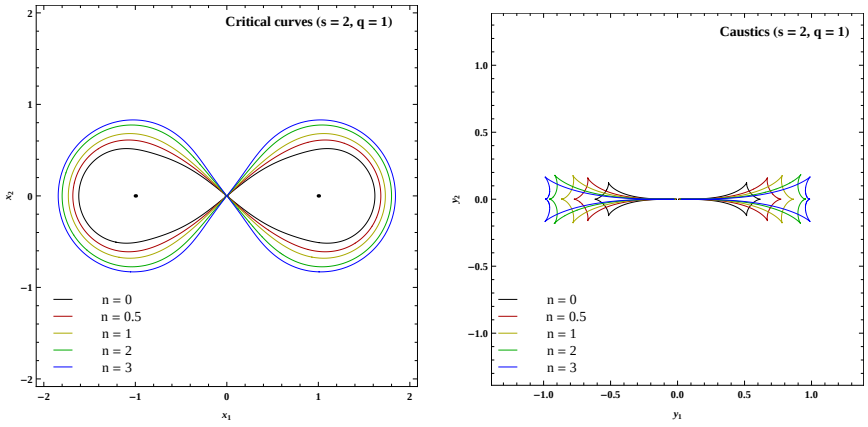

Figure 4.5: Equal-strength binary. Intermediate-Wide transition

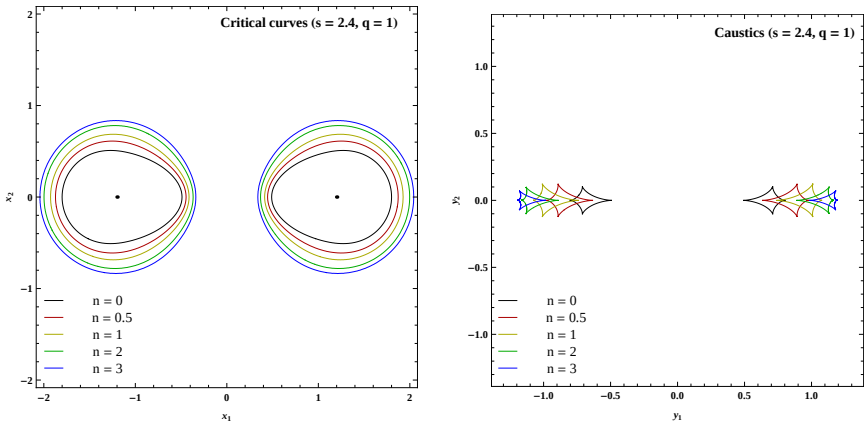

Figure 4.6: Equal-strength binary. Wide separation

of the intermediate caustics orthogonal to the lens-axis decreases gradually as we go deeper into the intermediate regime. In Fig. 4.4, we still have the $n = 2$ and $n = 3$ caustics larger than the $n = 1$ one, but they are all comparable now. The $n = 0.5$ and $n = 0$ caustics are still smaller than the $n = 1$ one. The transition between the intermediate and wide regime occurs at $s = 2$. This is true not only for $n = 1$, but also for all values of n, as is evident in Fig. 4.5. At this separation, the critical curve has a figure-eight shape with the beak-to-beak singularity. Finally, Fig. 4.6 illustrates the wide regime with $s = 2.4$. The critical curves tend to become circular as the lenses move far apart. However, we note that the curves remain more distorted at lower n, since the tidal field of the perturbing body decays more slowly. Correspondingly, the largest caustic is now the $n = 0$, with the others becoming smaller and smaller at larger n. Another thing we should note is

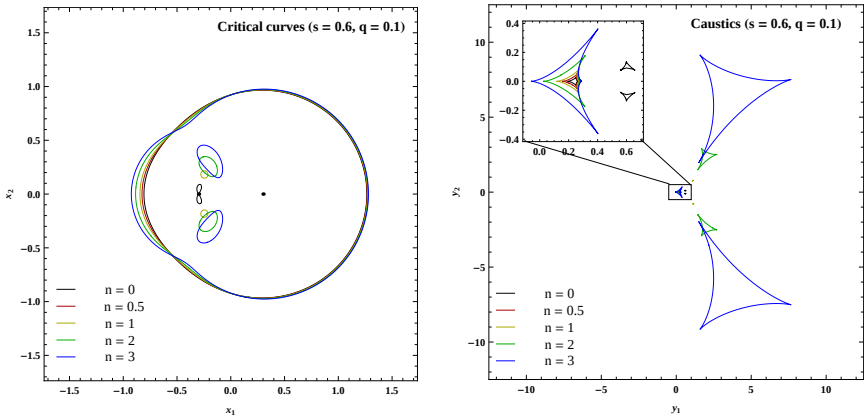

Figure 4.7: Unequal-strength binary. Close separation

that the radius of the critical curves is not the same for all n. This is in agreement with the discussion at the end of Section 4.1. Since either lens has strength $\epsilon_i = 1/2$, the angular Einstein ring of either lens tends to $1/2^{1/(n+1)}$, which grows with n.

4.3.2 Unequal-strength binary $q = 0.1$

Now we move to the unequal strength case, starting with a moderate strength ratio $q = 0.1$. In the close regime, shown in Fig. 4.7, we see the same characteristics already discussed in the equal-strength case: the main critical curve giving rise to the central caustic and the two smaller critical curves inside the main one, giving rise to the triangular caustics. The asymmetry of the lenses make the secondary critical curves move toward the weaker lens. For ordinary matter distributions ($n < 1$), the critical curves rush toward the weaker lens; the secondary caustics become smaller and closer to the primary caustic. Going from the $n = 1$-lensing to higher n we see that the inner critical curves become larger, drift toward the center of the system and become radially elongated. The corresponding caustics become larger and larger similarly to the equal-strength case. We also note that the main critical curve is perturbed on the side of the weaker lens, which is again a consequence of the scaling of the individual Einstein rings as $\epsilon_i^{1/(n+1)}$. In Fig. 4.8 we have $s = 0.769$, corresponding to the transition from the close to the intermediate regime in the $n = 1$ case. As already found in the equal-strength case, the transition occurs earlier (smaller s) for $n > 1$ and later (larger s) for $n < 1$. The $n > 1$ caustics are significantly larger than the $n = 1$ one. Then we have Fig. 4.9, with the intermediate regime $s = 1$. The caustics become comparable in size. The transition between the intermediate and the wide

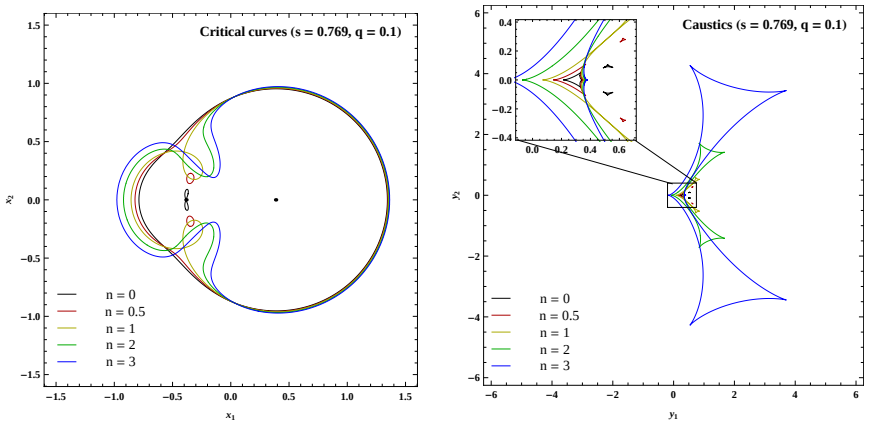

Figure 4.8: Unequal-strength binary. Close-Intermediate transition

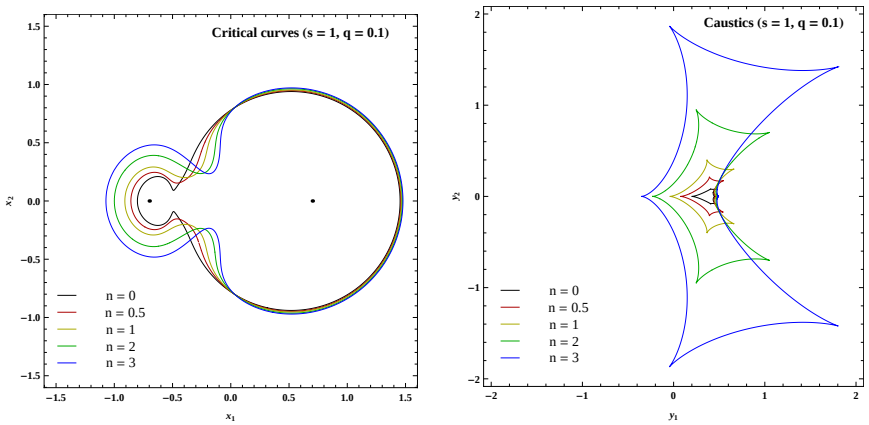

Figure 4.9: Unequal-strength binary. Intermediate separation

regime occurs at $s = 1.689$ for $n = 1$ but is pushed to higher separations for $n > 1$ and to lower separations for $n < 1$. So, contrarily to what happens in the equal-strength case, also this transition is affected when we change n. In general, the intermediate regime occupies a larger volume in the parameter space for $n > 1$ and a smaller volume for $n < 1$. Finally, Fig. 4.11 shows the wide regime $s = 2$. Note that the weaker lens critical curve has a radius that strongly depends on n, since $\theta_E \sim \epsilon_i^{1/(n+1)}$. The caustic of the weaker lens, instead, remains of the same size and it moves toward the projected lens position at higher n.

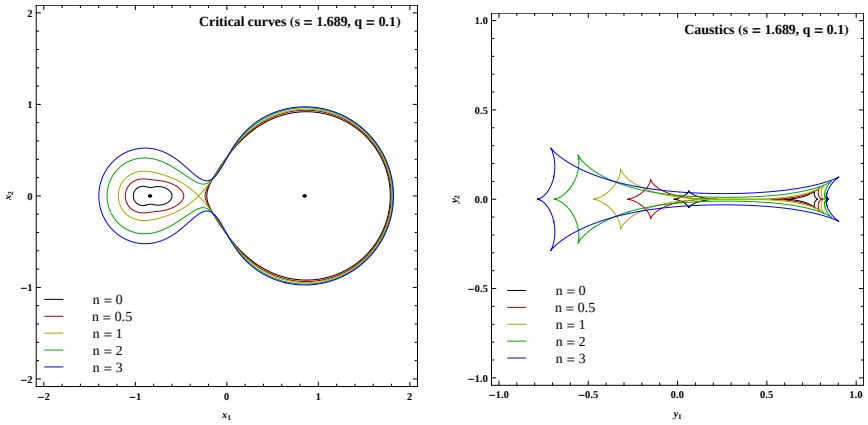

Figure 4.10: Unequal-strength binary. Intermediate-Wide transition

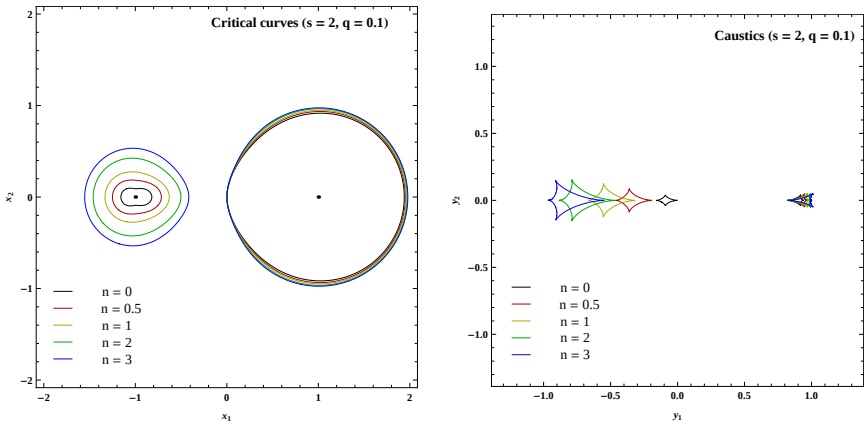

Figure 4.11: Unequal-strength binary. Wide separation

4.3.3 Extreme unequal-strength binary $q = 0.001$

Now we go deeper into the unequal-strength regime of the binary lens, with $\epsilon_A \ll \epsilon_B$. In the standard $n = 1$ context, this regime is conventionally called the "planetary" limit, as it naturally applies to the search for exoplanetary systems by the microlensing method. For $n = 0$, it may represent gravitational lensing by a massive galaxy accompanied by a smaller satellite. Fig. 4.12 shows the close regime for $s = 0.6$. The central caustic remains tiny, as the main critical curve is very weakly perturbed by the weaker lens. The small inner critical curves grow larger with n, as already noted in the previous subsection. The corresponding triangular caustics, become huge. This contrasts with the $n = 1$ case, for which it is well known that the chance of detecting planets is related to the probability that the source trajectory

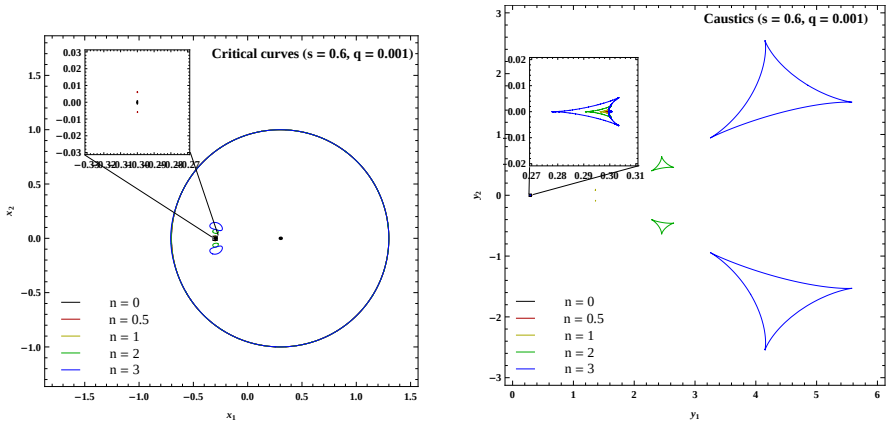

Figure 4.12: Extreme unequal-strength binary. Close separation

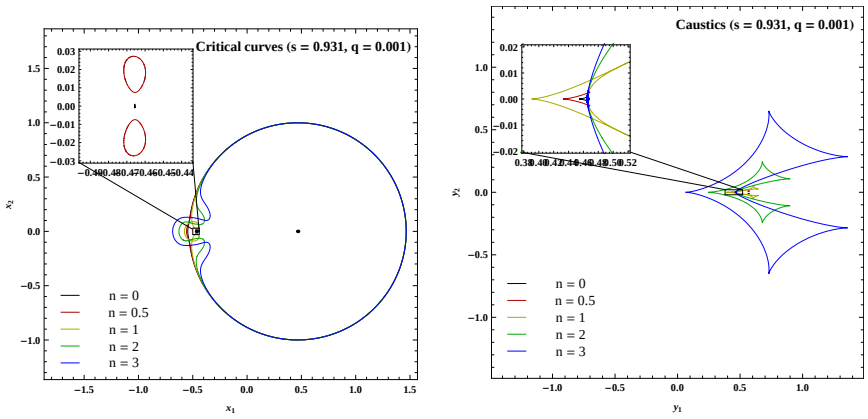

Figure 4.13: Extreme unequal-strength binary. Close-Intermediate transition

crosses these very small caustics. In the $n > 1$ case, it is much easier to detect a weaker component. The transition between the close and intermediate regime occurs at $s = 0.931$ in the $n = 1$ case. For $n > 1$ we are already in the intermediate regime here (Fig. 4.13), while we are still in the close regime for $n < 1$, although the secondary critical curves and caustics are almost invisible. At $s = 1$ (Fig. 4.14), we are in the so-called resonant regime, for which the $n = 1$ caustic assumes the largest size. Actually, for $n > 1$ the total size of the caustics is similar to that in the close regime, which is dominated by the triangular caustics. At $s = 1.153$, the $n = 1$ caustic enters the wide regime, while the $n > 1$ ones are still in the intermediate regime. The caustics rapidly evolve but still the $n > 1$ ones remain larger (Fig. 4.15). In general, the $n < 1$ caustics are extremely small. In the wide regime (Fig. 4.16), we have two separate critical curves. The weaker lens still has a larger

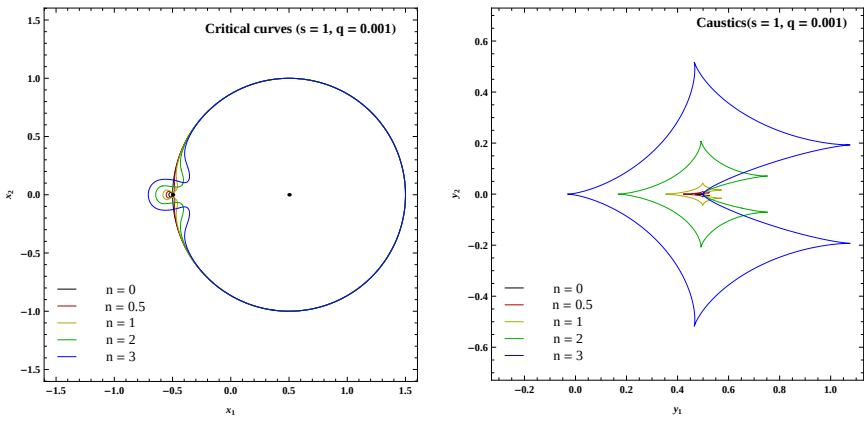

Figure 4.14: Extreme unequal-strength binary. Intermediate separation

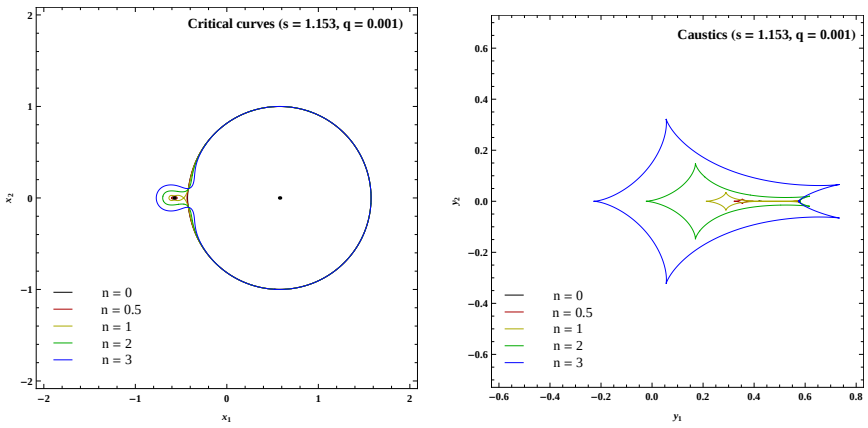

Figure 4.15: Extreme unequal-strength binary. Intermediate-Wide transition

ring in the $n > 1$ case, as discussed before. The caustics tend to become of similar size, as in the $q = 0.1$ case, although at $s = 1.4$ we still appreciate that the $n > 1$ caustics are slightly larger than the $n = 1$ one and are closer to the projected lens position.

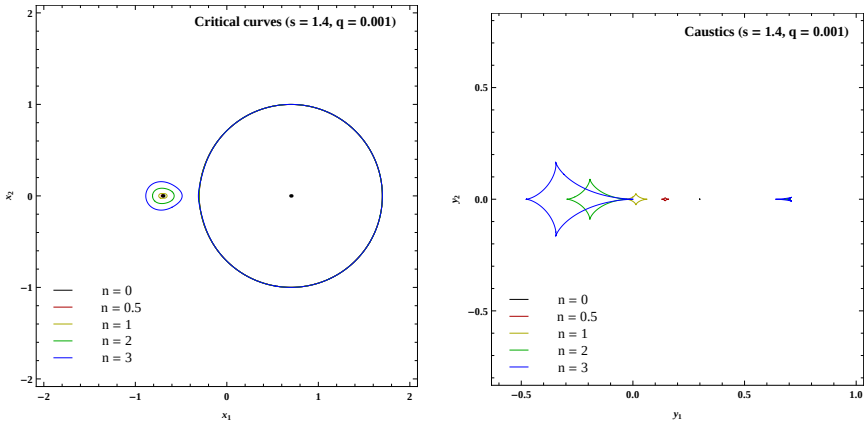

Figure 4.16: Extreme unequal-strength binary. Wide separation

4.4 Boundaries of the three topology regimes

In the standard Schwarzschild case (see Ref. [72]), the transition between the close and intermediate regime occurs at a separation $s_{CI,n=1}$ implicitly given by the solution of the equation

$$\frac{q}{(q+1)^2} = \frac{(1-s_{CI,n=1})^3}{27 s_{CI,n=1}^8}, \tag{4.7}$$

while the transition between the intermediate and wide regime falls at

$$s_{IW,n=1} = \frac{\left(q^{\frac{1}{3}}+1\right)^{\frac{3}{2}}}{(q+1)^{\frac{1}{2}}}. \tag{4.8}$$

Our numerical exploration has shown that the three topologies known in the $n = 1$ cases (close, intermediate, wide) naturally propagate to the $n > 1$ case, with no change, save for the sizes and elongation of critical curves and caustics. However, we have already noted how the region in the parameter space corresponding to the intermediate regime widens with respect to the standard case, with the only exception of the equal-strength case, for which the intermediate-wide transition still occurs for $s = 2$ for any n. In the $n < 1$ case, instead, the region corresponding to the intermediate regime shrinks and we have an additional catastrophe (the elliptic umbilic) well within the close regime. However, this catastrophe does not change the overall caustic topology. In this section we aim at finding the boundaries of the three topology regimes in the parameter space for any n and the position of the elliptic umbilic for $n < 1$. Transitions occur via higher order

singularities of the lens map, namely beak-to-beak singularities in the binary lens case. So, in order to find the values of the parameters q and s for which such transitions occur, we need to impose that the Jacobian J and its derivative $\partial J/\partial z$ simultaneously vanish. This quantity reads

$$\begin{aligned}\frac{\partial J}{\partial z} &= \frac{1-n^2}{4}\left[\frac{\epsilon_A}{(z+s/2)^{\frac{n+3}{2}}(\bar{z}+s/2)^{\frac{n+1}{2}}}+\frac{\epsilon_B}{(z-s/2)^{\frac{n+3}{2}}(\bar{z}-s/2)^{\frac{n+1}{2}}}\right]\\ &\left\{2+(n-1)\left[\frac{\epsilon_A}{(z+s/2)^{\frac{n+1}{2}}(\bar{z}+s/2)^{\frac{n+1}{2}}}+\frac{\epsilon_B}{(z-s/2)^{\frac{n+1}{2}}(\bar{z}-s/2)^{\frac{n+1}{2}}}\right]\right\}\\ &-\frac{(n-1)(n+1)^2}{8}\left|\frac{\epsilon_A}{(z+s/2)^{\frac{n+1}{2}}(\bar{z}+s/2)^{\frac{n+3}{2}}}+\frac{\epsilon_B}{(z-s/2)^{\frac{n+1}{2}}(\bar{z}-s/2)^{\frac{n+3}{2}}}\right|^2\\ &+\frac{(n+3)(n-1)^2}{8}\left\{\left[\frac{\epsilon_A}{(z+s/2)^{\frac{n+5}{2}}(\bar{z}+s/2)^{\frac{n-1}{2}}}+\frac{\epsilon_B}{(z-s/2)^{\frac{n+5}{2}}(\bar{z}-s/2)^{\frac{n-1}{2}}}\right]\right.\\ &\left.\left[\frac{\epsilon_A}{(z+s/2)^{\frac{n-1}{2}}(\bar{z}+s/2)^{\frac{n+3}{2}}}+\frac{\epsilon_B}{(z-s/2)^{\frac{n-1}{2}}(\bar{z}-s/2)^{\frac{n+3}{2}}}\right]\right\},\end{aligned} \tag{4.9}$$

which looks extremely complicated. However, we have managed to find the simultaneous solution of the equations $\partial J/\partial z = 0$ and $J = 0$ corresponding to the intermediate-wide transition. Unfortunately, after many efforts, we have not been able to find the close-intermediate transition. Concerning the intermediate-wide transition, we know that the beak-to-beak singularity occurs along the line joining the two lenses. This can be expressed by requiring $z = \bar{z}$ in complex notations. Then we introduce a new variable

$$y = \frac{s/2 - z}{s/2 + z}, \tag{4.10}$$

replacing z in J and $\partial J/\partial z$. We then solve $\partial J/\partial z = 0$ in terms of y, obtaining

$$y = \left(\frac{\epsilon_B}{\epsilon_A}\right)^{\frac{1}{2+n}} \tag{4.11}$$

Finally, we insert this expression for y in J and solve $J = 0$ for s. In this way, we obtain:

$$s_{WI} = (q+1)^{-\frac{1}{n+1}}\left(q^{\frac{1}{n+2}}+1\right)^{\frac{n+2}{n+1}} \tag{4.12}$$

which reduces to the solutions already known (Eq. (4.8)) for $n = 1$ [72] and for the $n = 0$ case [31]. For the Close-Intermediate transition, we are unable to extend Eq. (4.7) to arbitrary values of n, but we can easily study the transition numerically. Fig 4.17 plots s_{IC} and s_{WI} as functions of q for

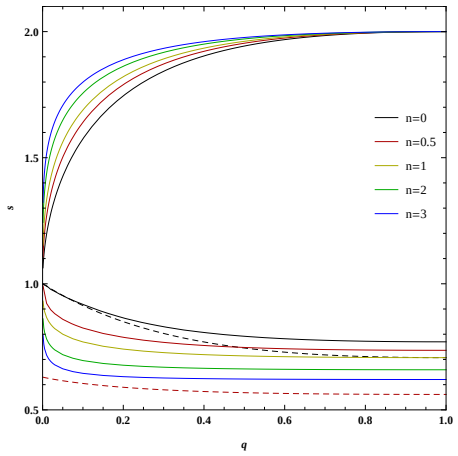

Figure 4.17: The critical values of the projected separation (in units of θ_E) at which the caustics topology of a binary lens changes as a function of the mass ratio q and the index n. The upper curves is s_{WI}, i.e. the critical value of s between the wide caustic and the intermediate or resonant caustic topology. The lower curves correspond to s_{IC}, the critical value between the resonant caustic and close caustic topology.

$n = (0, 0.5, 1, 2, 3)$. Note that for equal-mass binaries, $q = 1$ the critical value of the intermediate-wide separation is always 2 for any index n, as already anticipated in the previous section. In addition to the main topology transitions, we have discussed the existence of an elliptic umbilic catastrophe in the close regime for $n < 1$. Shin and Evans [31] showed that this catastrophe should lie centered half-way between the two lenses and passing through them. We find that their argument is still valid for any values of n and therefore look for simultaneous solutions of the equations $J = 0$ and $\partial J/\partial z = 0$ along this circle. After setting $z = se^{i\theta}/2$, we introduce the variable t by the equation

$$t^{\frac{1}{1+n}} \equiv \tan\frac{\theta}{2}. \tag{4.13}$$

This considerably simplifies the two equations and we obtain the angular position of the elliptic umbilic as

$$t = \frac{\epsilon_B}{\epsilon_A}, \tag{4.14}$$

and the critical value of the separation at which the catastrophe occurs

$$s = (1-n)^{\frac{1}{1+n}}\sqrt{\epsilon_A^{\frac{2}{1+n}} + \epsilon_B^{\frac{2}{1+n}}}, \tag{4.15}$$

which nicely matches the $n = 0$ limit already found in Ref. [31]. As shown by this formula, for $n \to 1$ the elliptic umbilic occurs at zero separation and is therefore unobservable from $n = 1$ on. In Fig. 4.17 the positions of the elliptic umbilic in the parameter space are shown by dashed curves in the cases $n = 0$ and $n = 0.5$.

4.5 Analytical approximation of Critical curves and Caustics

Our numerical study of the critical curves and caustics of exotic lenses has shown some interesting differences with respect to the standard Schwarzschild case. In particular, the enormous size of the formerly small triangular caustics in the close topology represents the most impressive novelty of the systems explored in our investigation. These numerical results call for support by analytical formulae describing the behavior of the caustics in some particular limits. In the binary Schwarzschild lens, this kind of exploration has led to several interesting analytical results in the close, wide and planetary limits [50, 51, 52, 53, 54, 55, 56]. Some analytical results have also been obtained for the $n = 0$ case [31]. In this section we extend these studies to a generic value of the exponent n. By discussing the analytical approximations, we will gain a much deeper understanding of the evolution of the caustic structure with n.

4.5.1 Wide binary

First, let us consider the simplest limit: an isolated object whose deflecting potential is perturbed by another object at a distance much larger than the Einstein radius. We place our lens at position $z_A = 0$, and the perturbing object at $z_B = -s$, with $s \gg 1$. So the lens equation reads:

$$\zeta = z - \frac{\epsilon_A}{z^{\frac{n-1}{2}}\bar{z}^{\frac{n+1}{2}}} - \frac{\epsilon_B}{(z+s)^{\frac{n-1}{2}}(\bar{z}+s)^{\frac{n+1}{2}}} \tag{4.16}$$

Their properties can be studied through the Jacobian determinant of the lens map

$$\begin{aligned} J \;= & \left\{1 + \frac{n-1}{2}\left[\frac{\epsilon_A}{z^{\frac{n+1}{2}}\bar{z}^{\frac{n+1}{2}}} + \frac{\epsilon_B}{(z+s)^{\frac{n+1}{2}}(\bar{z}+s)^{\frac{n+1}{2}}}\right]\right\}^2 \\ & - \frac{(n+1)^2}{4}\left|\frac{\epsilon_A}{z^{\frac{n+3}{2}}\bar{z}^{\frac{n-1}{2}}} + \frac{\epsilon_B}{(z+s)^{\frac{n+3}{2}}(\bar{z}+s)^{\frac{n-1}{2}}}\right|^2 . \end{aligned} \tag{4.17}$$

Starting from an isolated point-lens, the presence of the other mass, that is very far from the first one, deforms the circular critical curve. This deformation can be recovered by a perturbative approach [50, 52]. Therefore, we set

$$z = \rho(1+\delta)e^{i\theta}, \tag{4.18}$$

with $\delta \sim 1/s^p$, and the exponent p being fixed by the perturbative expansion. At zero order, sending s to infinity in Eq. (4.17), the equation $J = 0$ is solved by

$$\rho = \epsilon_A^{1/(n+1)}, \tag{4.19}$$

which is the critical curve for a single lens. To first order in $1/s$, the first correction to the critical curve appears for $\delta \sim 1/s^{n+1}$:

$$\delta = \frac{\epsilon_B[1 - n + (n+1)\cos(2\theta)]}{2(n+1)s^{n+1}}. \tag{4.20}$$

In the standard $n = 1$ case, this correction reduces to

$$\delta = \frac{\epsilon_B \cos(2\theta)}{2s^2}, \tag{4.21}$$

which matches what was found in previous studies [50, 52]. The deformation of the circular critical curve is still given by $\cos(2\theta)$ with the same amplitude independent of n. However, the curve is slightly shrunk (or enlarged) by a fixed term proportional to $(1-n)/(n+1)$. By applying the lens equation (4.16) and expanding we obtain:

$$Re[\zeta(\theta)] = -\frac{\epsilon_B}{s^n} + \frac{(n+1)\epsilon_A^{1/(n+1)}\epsilon_B \cos^3\theta}{s^{n+1}} \tag{4.22}$$

$$Im[\zeta(\theta)] = -\frac{(n+1)\epsilon_A^{1/(n+1)}\epsilon_B \sin^3\theta}{s^{n+1}} \tag{4.23}$$

For $\epsilon_B \to 0$ we return to the case of a point-lens, therefore the terms with ϵ_B give the perturbation of the caustics. The first term in $Re[\zeta]$ is a shift $-\epsilon_B/s^n$ of the caustic in the direction toward the perturbing object. The shift decays with the index n, in agreement with what we note in Figs. 4.6, 4.11, 4.16. The other terms in ζ describe the shape of the caustics as $\cos^3\theta + i\sin^3\theta$, which corresponds to the classic Chang-Refsdal 4-cusped astroid [70, 52]. This does not change from $n = 1$ to greater or smaller n. However, the size of the caustic scales as $(n+1)/s^{n+1}$. At moderate separations, the caustics at higher n are larger than in the $n = 1$ case, but in the deep wide limit $s \gg 1$, the caustics become smaller and smaller.

4.5.2 Close binary

The close binary regime poses the greatest challenge for any analytical results, as we already experienced with our search for the boundary between the close and intermediate regime. We will first discuss the central caustic [50, 52] and then the "secondary" caustics [53], which for $n > 1$ give rise to the huge triangular structures shown in our numerical investigation.

Central caustic

We leave the two masses at positions $z_A = -s/2$ and $z_B = s/2$ as in the lens equation (4.2) and consider the Jacobian determinant in the form of Eq. (4.6). The separation between the masses s modulate the deviations from the Schwarzschild lens and constitute the perturbative parameter in our expansion. We use the parameterization

$$z = \rho(1 + \delta_1 + \delta_2)e^{i\theta}, \tag{4.24}$$

where δ_1 is of order s, and δ_2 is of order s^2 . Substituting in equation (4.6) and expanding in powers of s up to second order, we can solve for ρ, δ_1 and δ_2 :

$$\begin{aligned}
\rho &= 1 \\
\delta_1 &= \frac{1}{2}(-\epsilon_A + \epsilon_B)\cos\theta \; s \\
\delta_2 &= \frac{1}{16}\{-1 + 4n\epsilon_A\epsilon_B + [1 + (16 + 4n)\epsilon_A\epsilon_B]\cos(2\theta)\} \; s^2
\end{aligned} \tag{4.25}$$

Note that, the dependence on n is only in the second order of the expansion. Once known the perturbations to the critical curve, we can find the caustic using the lens equation:

$$Re[\zeta(\theta)] = \frac{(-\epsilon_A + \epsilon_B)}{2(\epsilon_A + \epsilon_B)}s + \frac{(n+1)\epsilon_A\epsilon_B\cos^3\theta}{(\epsilon_A + \epsilon_B)^{\frac{2n+3}{n+1}}}s^2 \tag{4.26}$$

$$Im[\zeta(\theta)] = -\frac{(n+1)\epsilon_A\epsilon_B\sin^3\theta}{(\epsilon_A + \epsilon_B)^{\frac{2n+3}{n+1}}}s^2 \tag{4.27}$$

The first order perturbations in $Re[\zeta]$ is simply a shift term that displaces the caustic from the origin (median point between the two lenses) to the center of strength (the wording "center of mass" should be reserved to $n = 1$ case only). The dependence on n appears at the second order terms in ζ with the factor $(n+1)$. The denominator is just a power of $(\epsilon_A + \epsilon_B)$, which has been set to 1 in our investigations. Then we learn that the central caustic scales linearly

with the exponent n, something that can be appreciated in Fig. 4.12, in particular, but occurs for all values of the strength ratio q. The shape of the caustic is still the classical 4-cusped astroid as in the wide separation limit, reminding us of the wide-close degeneracy [50], which plagues gravitational lensing by binary systems.

Secondary caustics

The lens map is characterized by secondary critical curves that can appear in the form of small ovals near the center of strength of the system (Fig. 4.1) [52, 53]. These secondary critical curves produce tiny caustics for $n < 1$ and the huge triangular caustics far from the lens system for $n > 1$. So, we are particularly interested in confirming our numerical results by an analytical approximation that makes us understand how this phenomenology arises. Our starting point is still the Jacobian in the form Eq. (4.6). The critical curves appear along a circle with radius $s/2$ centered in our origin. Unfortunately, we are unable to achieve a full description of these small ovals and we have to content ourselves with some partial yet valuable information. By setting

$$z = \frac{s}{2} e^{i\theta}, \tag{4.28}$$

we manage to obtain the two intersections of these ovals with the circle of radius $s/2$. These two points are already enough to appreciate the size of the ovals and then of the corresponding tiny (for $n \leq 1$) or giant (for $n > 1$) caustics. Inserting this parameterization in Eq. (4.6) and saving the zero order in s only, we obtain an equation for θ:

$$-\epsilon_A \epsilon_B e^{2\imath n\pi}(n^2+1)\sin\theta \sin^n(\theta/2)\cos^n(\theta/2)+2n[{\epsilon_A}^2 \sin^{2n+2}(\theta/2)+{\epsilon_B}^2\cos^{2n+2}(\theta/2)] = 0. \tag{4.29}$$

This equation is satisfied by the angles:

$$\theta_1 = 2\tan^{-1}\left[\left(\frac{\epsilon_B}{n\epsilon_A}\right)^{\frac{1}{n+1}}\right] \tag{4.30}$$

$$\theta_2 = 2\tan^{-1}\left[\left(\frac{n\epsilon_B}{\epsilon_A}\right)^{\frac{1}{n+1}}\right]. \tag{4.31}$$

These two angles represent the positions of the two intersections of the secondary critical curves with the circle of radius $s/2$. Note that the standard case $n = 1$ is degenerate, in the sense that the two intersections coincide at zero order. This is a warning that only in the special Schwarzschild lens the secondary critical curves require an expansion to the next order in s of the

Jacobian [53]. This is the root of the extreme difference in size we find when we move from $n = 1$ to $n > 1$. At $n > 1$ the secondary critical curves open up at first order already, while they remain pointlike at $n = 1$ and open up at second order only. Having widened our horizons by our exploration of all values of n, we learn that this fact is related to the presence of the elliptic umbilic at $n < 1$, which collapses to $s = 0$ for $n \to 1$. Therefore, in the starting point of our expansion at small s, the $n = 1$ case is at the elliptic umbilic, which makes secondary critical curves shrink to zero size. Setting $\epsilon_A = \epsilon_B$ in θ_1 and θ_2, we can easily see that $\theta_2 - \pi/2 = \pi/2 - \theta_1$, i.e. the two intersections are symmetrical with respect to the vertical axis, as it is expected in the equal-strength case. Using the lens equation, we can calculate the position of the caustic points corresponding to these intersections. We find

$$\zeta = \frac{(n^{-\frac{2}{1+n}} + 1)^{\frac{n-1}{2}}}{2n^{\frac{1}{1+n}} s^n} \left[\left(n^{\frac{n}{1+n}} - n^{\frac{1}{1+n}} \right) - i(n+1) \right] \tag{4.32}$$

The imaginary part of these caustic points gives us an idea of the distance of the secondary caustic from the origin. The real part, instead, can be taken as a measure of the transverse extension of the caustic. Note that the latter is exactly zero in the limit $n = 1$, which means that the extension of the caustic must be calculated at the next order in the power expansion in s in the standard case. Indeed, from previous studies, [53] we know that the transverse extension of the secondary caustic is proportional to s^3 for the standard binary Schwarzschild lens. When $n > 1$, the secondary caustic has an extension comparable to its shift along the vertical axis, which is what we have observed in Figs. 4.1, 4.7 and 4.12. More in detail, we can make a plot of the real and imaginary parts of Eq. (4.32) at fixed separation as functions of n, as shown in Fig. 4.18. This plot makes us appreciate the impressive sizes reached by these giant caustics.

4.5.3 Extremely unequal-strength ratio limit

The limit $\epsilon_B \ll \epsilon_A$ takes the form of the planetary limit in the $n = 1$ case [50, 51, 52]. This limit is also interesting because it is possible to fully describe the huge triangular caustics of the close topology, confirming our previous partial results.

Central caustic

We consider the main lens at position $z_A = 0$ accompanied by a weak perturbing object placed at $z_B = -s$. The lens equation and the Jacobian

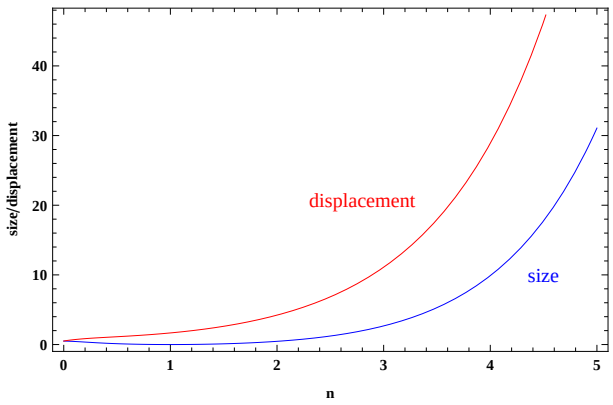

Figure 4.18: Real and imaginary parts of the caustic points calculated in Eq. (4.32). The imaginary part is a measure of the distance of the secondary caustics, while the real part is a measure of the transverse size. The graphic is for $s = 0.6$.

determinant take the forms already calculated in the wide limit (4.16), (4.17). We then introduce the parameterization

$$z = \epsilon_A^{1/(n+1)}(1+\delta)e^{i\theta}, \tag{4.33}$$

where δ is of order of $\epsilon_B \ll \epsilon_A$. Substituting in Eq. (4.17) and expanding in power series about the point $\epsilon_B = 0$, to first order in ϵ_B, we can solve for δ:

$$\delta = \frac{\epsilon_B\{2\epsilon_A^{2/(n+1)} + 4\epsilon_A^{1/(n+1)}\cos\theta\ s + [1-n+(n+1)\cos(2\theta)]s^2\}}{2(n+1)\left[\epsilon_A^{2/(n+1)} + 2\epsilon_A^{1/(n+1)}\cos\theta\ s + s^2\right]^{\frac{n+3}{2}}} \tag{4.34}$$

Once determined δ, we can find the caustic by use of the lens equation:

$$\zeta = -\frac{\{4\epsilon_A^{2/(n+1)}e^{\imath\theta} - \epsilon_A^{1/(n+1)}[n-3-2(n+3)e^{2\imath\theta} + (n+1)e^{4\imath\theta}]\ s + 4e^{\imath\theta}s^2\}\epsilon_B\ s}{4e^{\imath\theta}(\epsilon_A^{2/(n+1)} + 2\epsilon_A^{1/(n+1)}\cos\theta\ s + s^2)^{\frac{n+3}{2}}} \tag{4.35}$$

to first order in ϵ_B. The size of the caustic is proportional to ϵ_B, as in the standard $n = 1$ case. More precisely, the distance between the left and right cusps (obtained with $\theta = \pi$ and $\theta = 0$ respectively) is

$$\Delta\zeta = \epsilon_B s\left[\left|s - \epsilon_A^{1/(n+1)}\right|^{-n-1} - \left|s + \epsilon_A^{1/(n+1)}\right|^{-n-1}\right]. \tag{4.36}$$

While the size increases with n for $s < 2$ because of the first term, it decreases for $s > 2$. It is finally interesting to extend the famous wide/close degeneracy for the central caustic of the "planetary" system to the case of arbitrary n

[57, 50, 51]. Indeed, we find that the formula (4.35) is invariant under the transformation

$$s \to \frac{\epsilon_A^{2/(n+1)}}{s}, \quad \epsilon_B \to \epsilon_B \left(\frac{\epsilon_A^{1/(n+1)}}{s} \right)^{n-1} . \tag{4.37}$$

We remind that the radius of the critical curve of an isolated exotic object is proportional to $\epsilon_A^{1/(n+1)}$, which makes clear that the inversion of s is exactly the same we find in the standard case. However, for $n \neq 1$, the transformation must be complemented by a change in the strength of the perturbing object.

Caustics of the perturbing object

In order to study the caustics of the perturbing object, which reduce to the planetary caustics in the $n = 1$ limit [51, 52], we put the main lens at $z_A = -s$ and the secondary lens at $z_B = 0$. The lens equation takes the form:

$$\zeta = z - \frac{\epsilon_A}{(z+s)^{\frac{n-1}{2}}(\bar{z}+s)^{\frac{n+1}{2}}} - \frac{\epsilon_B}{z^{\frac{n-1}{2}}\bar{z}^{\frac{n+1}{2}}}, \tag{4.38}$$

and the Jacobian determinant is

$$\begin{aligned} J &= \left\{ 1 + \frac{n-1}{2} \left[\frac{\epsilon_A}{(z+s)^{\frac{n+1}{2}}(\bar{z}+s)^{\frac{n+1}{2}}} + \frac{\epsilon_B}{z^{\frac{n+1}{2}}\bar{z}^{\frac{n+1}{2}}} \right] \right\}^2 \\ &\quad - \frac{(n+1)^2}{4} \left| \frac{\epsilon_A}{(z+s)^{\frac{n+3}{2}}(\bar{z}+s)^{\frac{n-1}{2}}} + \frac{\epsilon_B}{z^{\frac{n+3}{2}}\bar{z}^{\frac{n-1}{2}}} \right|^2 . \end{aligned} \tag{4.39}$$

We write

$$z = \rho^{1/(n+1)} \epsilon_B^{1/(n+1)} e^{i\theta}, \tag{4.40}$$

and substitute in the equation (4.39). The lowest order Jacobian is:

$$\frac{(n+\rho)(\rho-1)}{\rho^2} + \frac{[(n-1)(2\rho+n-1) - (n+1)^2\cos(2\theta)]\epsilon_A}{2\rho s^{n+1}} - \frac{n\epsilon_A^2}{s^{2n+2}} = 0. \tag{4.41}$$

Solving this last equation for ρ, we find two solutions:

$$\begin{aligned} \rho_\pm &= \frac{\{\epsilon_A[(n+1)^2\cos(2\theta) - (n-1)^2] + (2-2n)s^{n+1} \pm (n+1)\sqrt{\Delta}\}s^{n+1}}{4(s^{n+1}-\epsilon_A)(s^{n+1}+n\epsilon_A)} \\ \Delta &= 4s^{2n+2} + 2\epsilon_A\{(4n-4)s^{n+1} + \epsilon_A[n^2 - 6n + 1 - (n+1)^2\cos(2\theta)]\} \end{aligned} \tag{4.42}$$

Now, when the secondary object is outside of the main lens Einstein ring, the critical curve assumes the shape of an elongated ring. When the planet

is inside the main lens critical curve, the secondary object generates two specular ovals. According to the double sign, two branches are present. For external objects ($s > 1$) only the higher is real, while for internal objects ($s < 1$) both branches are real in a small interval centered on $\theta = \pi/2$ [51, 52]. So, we have fully analytical formulae describing the secondary critical curves of the close topology in the extreme strength-ratio limit, something that was not possible to achieve for arbitrary values of the strength ratio. Through the lens equation, we can find the caustics

$$\zeta = \frac{\epsilon_A \epsilon_B^{1/(n+1)} \rho [n+1+(n-1)e^{2\imath\theta}] - 2\epsilon_A \rho^{n/(n+1)} e^{\imath\theta} s + 2\epsilon_B^{1/(n+1)} e^{2\imath\theta}(\rho-1)s^{n+1}}{2\rho^{n/(n+1)} e^{\imath\theta} s^{n+1}}. \tag{4.43}$$

This formula gives a full description of the caustics in the $\epsilon_B \ll \epsilon_A$ limit for all values of s. It can be used to obtain general indications of the size and the displacement of the secondary caustics from the main one. The displacement along the axis joining the two lenses can be obtained as the mid-point $(\zeta(0) + \zeta(\pi))/2$, which lies at the center of the secondary caustic structure. Taking into account that here we have considered the secondary object as the origin of the reference frame, the full displacement from the main object is

$$\zeta_{center} = s - \frac{\epsilon_A}{s^n}, \tag{4.44}$$

which reduces to the classical expression for the position of the planetary caustic for $n = 1$ [50, 51]. The extension of the caustic in the wide case in the direction parallel to the lens axis is simply given by $(\zeta(0) - \zeta(\pi))$, which reads

$$\Delta\zeta_{\parallel,wide} = 2(1+n)\frac{\epsilon_A \epsilon_B^{1/(1+n)}}{s^n \left(s^{1+n} - \epsilon_A\right)^{1/(1+n)}}. \tag{4.45}$$

In the vertical direction, orthogonal to the lens axis, $(\zeta(\pi/2) - \zeta(-\pi/2))$ gives

$$\Delta\zeta_{\perp,wide} = 2(1+n)\frac{\epsilon_A \epsilon_B^{1/(1+n)}}{s^n \left(s^{1+n} + n\epsilon_A\right)^{1/(1+n)}}. \tag{4.46}$$

The astroid caustic is slightly elongated toward the main lens. By increasing n, we have terms in the numerator that become larger and the s^{n+1} in the denominator which tend to compensate and dominate at larger separations, so that the size of the caustic tends to decrease in this regime. In the close regime $s < \epsilon_A^{1/(1+n)}$, we can easily pick the position of the outer cusp (the one most distant from the lens axis). This is found by setting $\theta = \pi/2$ in Eq. (4.43) and choosing the positive sign for the square root in ρ in Eq. (4.42).

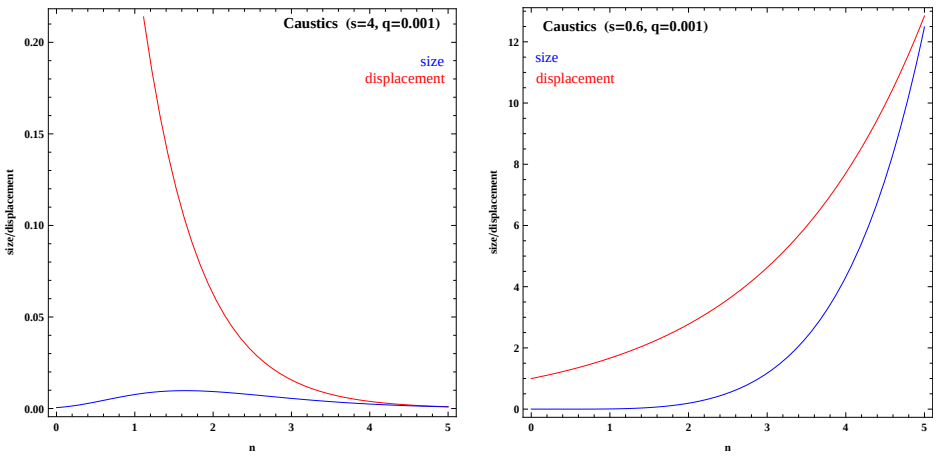

Figure 4.19: Size and displacement of the secondary caustics in the extreme strength ratio limit.

In fact, it can be easily verified that $d\zeta/d\theta = 0$ in this point, as it required by the cusp condition. The distance of this cusp from the lens axis is

$$Im[\zeta_+(\pi/2)] = (1+n)\frac{\epsilon_A \epsilon_B^{1/(1+n)}}{s^n \left(\epsilon_A - s^{1+n}\right)^{1/(1+n)}}. \tag{4.47}$$

The position of the remaining two cusps cannot be found analytically, but the mid-point is again given by $\zeta(\pi/2)$ with the negative sign for the square root of ρ in Eq. (4.42):

$$Im[\zeta_-(\pi/2)] = (1+n)\frac{\epsilon_B^{1/(1+n)}}{s^n \left[n(\epsilon_A - s^{1+n})\right]^{n/(1+n)}}. \tag{4.48}$$

The difference $Im[\zeta_+(\pi/2)] - Im[\zeta_-(\pi/2)]$ is thus a measure of the transverse size of the triangular secondary caustics. In Fig. 4.19 we show the trend of the position and the size of the caustic for $n \in [0, 5]$. In the wide regime, we note that the displacement of the secondary caustic from the perturbing object rapidly decreases going toward higher n. The size of the caustic first increases and then decreases at higher n. In the close regime, both the displacement and size increase with n. In particular, we see that the size reaches the same order of the displacement, giving rise to the huge caustics we have seen throughout our investigation. For $n < 1$, the transverse size (4.48) shrinks to zero for $s = (1-n)^{1/(n+1)}$, as prescribed by the correct limit of the elliptic umbilic singularity (4.15), and then grows again.

Discussion and Conclusions

The mathematical structure of the lens equation has inspired many studies in the past century, since it involves very spectacular aspects of the catastrophe theory [58]. Our study of the binary lens made up of two objects with metric falling as $1/r^n$ is not an exception in this picture. We have led a full numerical exploration of all topology regimes in the parameter space (s, q) where s is the separation of the two lenses and q is the strength ratio. We have traced the boundaries of the three topology regimes and for the occurrence of elliptic umbilics, and we have been able to derive analytical approximations for all the extreme cases, in analogy with what has been previously done for the standard binary lens with ordinary gravitational potentials $1/r$ [52, 53]. Although we have not found any new topologies with respect to the standard binary lens, all the positions and sizes of the caustics are modified by the power of the gravitational potential. In particular, the formerly small triangular caustics of the close topology become huge in size for $n > 1$, which comes as the most intriguing surprise of our study. Thanks to our analytical approximations, we have been able to quantify the sizes and displacements of caustics in all limits, confirming the numerical study. The by-products of these formulae have been barely explored in this thesis. We can just mention the extension of the famous wide/close degeneracy of the planetary limit [57] to the extreme strength ratio regime of the general $1/r^n$ space. The applications of this study are two-fold. The regime $n < 1$ corresponds to a generic matter distribution with a density profile scaling as r^{n+2}. Our exploration provides a considerable extension of previous results only known for the singular isothermal sphere ($n = 0$) [31]. We have confirmed that an elliptic umbilic catastrophe occurs in the close regime, while no critical curves ever reach the lens position as in the singular isothermal sphere. On the other side of the Schwarzschild lens, for $n > 1$, we have reached our goal of a first exploration of gravitational lensing by exotic $1/r^n$ objects in a non-trivial configuration. Such objects can only be obtained by some violation of the energy conditions. In our study we have focused on a pair of objects of the same type, so as to understand all modifications

of the standard binary case that have to be ascribed by the change of the Schwarzschild potential rather than to mixing effects. A possible next step would be the study of the mixed case with an ordinary Schwarzschild lens around an $1/r^n$ object. Indeed we might expect even more surprises from this asymmetric situation. The caustic structure is the basis to understand the full phenomenology of gravitational lensing. The much broader extension of caustics in the close and intermediate topology we find in our study suggests that it is much easier to form additional images for binary exotic lenses than for ordinary Schwarzschild lenses. However, this effect has to be weighted by the defocusing power which is known to appear with $1/r^n$ potentials for any $n > 1$. So, the application to astrophysical situations might set aside even more interesting surprises. We can imagine that microlensing by such binary lenses would feature incredibly long caustic crossings where they are not expected to be, accompanied by depressed regions in which one or more images are de-magnified. The existence of more signatures that might allow the unambiguous identification of exotic objects, including Ellis wormholes, is indeed the primary goal of this kind of studies. Considering that searches for Ellis wormholes in existing lensing databases have started [59], a full understanding of the interaction of these exotic objects with their environment is important to achieve a fully correct interpretation of these data.

Acknowledges

First and foremost, I would like to thank my supervisor Dr. Valerio Bozza for giving me the opportunity to write this thesis on a very interesting subject on the forefront of theoretical physics, and also for providing indispensable guidance and advice in learning this subject. I have had the pleasure of many meaningful friendships with the other PhD students in the program. Thank you all for many insightful conversations academic and otherwise. Thanks also to the many faculty members who have helped me throughout my career at University of Salerno. Thanks to Professors C. Noce, I. Rabuffo, R. De Luca, A. Nigro, M. Polichetti, A. Di Bartolomeo. Finally, I would like to thank all of my family for their continued support.

Bibliography

[1] K. Schwarzschild,*Über das Gravitationsfeld eines Massenpunktes nach der Einsteinschen Theorie*, S.-B. Preuss, Akad. Wiss, Phys.-Math. K I. 7, 189-196 (1916).

[2] G.D. Birkhoff, *Relativity and Modern Physics*, Harvard University Press, (1923).

[3] A. Einstein and N. Rosen,*The Particle Problem in the General Theory of Relativity*, Phys. Rev. 48, 73 (1935).

[4] M. S. Morris and K. S. Thorne,*Wormholes in spacetime and their usefor intestellar travel: A tool for teaching general relativity*, Am. J. Phys. 56, 395. (1988).

[5] H. G. Ellis, *Ether flow through a drainhole. A particle model in general relativity*, J. Math. Phys. 14, 104 (1973).

[6] H. Bondi. *Negative Mass in General Relativity.*, Rev. Mod. Phys. 29 No. 3 July (1957).

[7] S.-W. Kim, Y.M. Cho, *Evolution of the Universe and Its Observational Quest*, Universal Academy Press and Yamada Science Foundation, Tokyo, (1994).

[8] J. Cramer, R. Forward,M. Morris, M. Visser, G. Benford, G. Landis, Phys. Rev. D 51, 3117 (1995).

[9] D.F. Torres, G.E. Romero, L.A. Anchordoqui, Phys. Rev. D 58, 123001 (1998).

[10] D.F. Torres, G.E. Romero, L.A. Anchordoqui, Mod. Phys. Lett. A 13, 1575 (1998).

[11] L. Anchordoqui, G.E. Romero, D.F. Torres, I. Andruchow, Mod. Phys. Lett. A 14, 791 (1999)

[12] G.E. Romero, D.F. Torres, I. Andruchow, L. Anchordoqui, B. Link, Mon. Not. R. Astron. Soc. 308, 799 (1999).

[13] H.B.G. Casimir, *On the attraction between two perfectly conducting plates*, Proc. K. Ned. Akad. Wet. 51, 793 (1948).

[14] V. Bozza and A. Postiglione, *Alternatives to Schwarzschild in the weak field limit of General Relativity*, JCAP 06, 036 (2015).

[15] Einstein A., 1915, *Erklärung der Perihelbewegung des Merkur aus der allgemeinen Relativitätstheorie*, Sitzungsber. Preuβ. Akad. Wissensch., erster Halbband.

[16] Robertson D. S., Carter W. E., Dillinger W. M., 1991, *New measurement of the solar gravitational deflection of radio signals using VLBI*, Nature 349, 28.

[17] S. Mollerach, E.Roulet *Gravitational Lensing and Microlensing*, World Scientific Publishing Co. Pte. Ltd. (2002).

[18] Dodelson, S. *Modern Cosmology* (Academic Press USA 2003).

[19] Schneider P., Ehlers J., Falco E. E., *Gravitational Lenses*, Springer Verlag, Berlin (1992).

[20] Dyer C. C., Roeder R. C., 1973, *Distance-Redshift Relations for Universes with Some Intergalactic Medium*, Ap. J. Lett. 180, 31.

[21] Misner C. W., Thorne K. S. and Wheeler J. A. (1973), *Gravitation*, W. H. Freeman and Co. , San Francisco.

[22] Burke W., *Multiple gravitational imaging by distributed masses*, Astrophys. J. 244, L1(1981).

[23] Shapiro 1.1. (1964), *Fourth test of General Relativity*, Phys. Rev. Lett. 13, 789.

[24] Refsdal S., 1964, *On the possibility of determining Hubble's parameter and the masses of galaxies from the gravitational lens effect*, M.N.R.A.S. 128, 307.

[25] Narayan, R. and Bartelmann, M., 1997, astro-ph/9606001v2.

[26] A. Zakharov, Gen. Rel. and. Grav. 42, 2301 (2010).

[27] V. Bozza, Gen. Rel. and. Grav. 42, 2269 (2010).

[28] L. Chetouani and G. Clément, Gen. Relativ. Gravit. 16, 111 (1984); V. Perlick, Phys. Rev. D 69 , 064017 (2004); K. K. Nandi, Y. Z. Zhang and A. V. Zakharov, Phys. Rev. D 74, 024020 (2006); T. K. Dey and S. Sen, Mod. Phys. Lett. A, 23, 953 (2008).

[29] F. Abe, ApJ, 725, 787 (2010).

[30] A. Bhattacharya and A. A. Potapov, Modern Physics Letters A, 25, 2399 (2010); Y. Toki, T. Kitamura, H. Asada and F. Abe, Astrophys. J. 740, 121 (2011); J. M. Tejeiro and E. A. Larranaga, Rom. J. Phys. 57, 736 (2012); N. Tsukamoto, T. Harada and K. Yajima, Phys. Rev. D 86, 104062 (2012); K. Nakajima and H. Asada, Phys. Rev. D 85, 107501 (2012); G. W. Gibbons and M. Vyska, Class. Quant. Grav. 29, 065016 (2012); Ch.-M. Yoo, T. Harada, and N. Tsukamoto, Phys. Rev. D 87, 084045 (2013).

[31] E.M. Shin and N.W. Evans, MNRAS 390, 505 (2008).

[32] P. Schneider and A. Weiss, A&A 164, 237 (1986).

[33] T. Kitamura, K. Nakajima, and H. Asada, *Demagnifying gravitational lenses toward hunting a clue of exotic matter and energy*, Phys. Rev. D 87, 027501 (2013).

[34] K. Izumi, et al., Phys. Rev. D 88, 024049 (2013); T. Kitamura, et al., Phys. Rev. D 89, 084020 (2014); N. Tsukamoto, T. Kitamura, K. Nakajima, and H. Asada, Phys.Rev. D 90, 064043 (2014); K. Nakajima, K. Izumi, and H. Asada, Phys. Rev. D 90, 084026 (2014); N. Tsukamoto and T. Harada, Phys. Rev. D, 87, 024024 (2013).

[35] M. S. Morris, K. S. Thorne, and U. Yurtsever, Phys. Rev. Lett. 61, 1446 (1988).

[36] Koji Izumi, Chisaki Hagiwara, Koki Nakajima, Takao Kitamura, and Hideki Asada, *Gravitational lensing shear by an exotic lens object with negative convergence or negative mass*, arXiv:1305.5037v2 (2013).

[37] V. Bozza and C. Melchiorre, *Caustics of* $1/r^n$ *binary gravitational lenses: from galactic haloes to exotic matter*, JCAP 03, 040 (2016).

[38] C. M. Will, Living Rev. Relativity 9, 3 (2006).

[39] B. Bertotti, L. Iess, and P. Tortora, Nature (London) 425, 374 (2003).

[40] R. Takahashi and H. Asada, *OBSERVATIONAL UPPER BOUND ON THE COSMIC ABUNDANCES OF NEGATIVE-MASS COMPACT OBJECTS AND ELLIS WORMHOLES FROM THE SLOAN DIGITAL SKY SURVEY QUASAR LENS SEARCH*, ApJ 768, L16 (2013).

[41] Hinshaw, G., Larson, D., Komatsu, E., et al., 2012, arXiv:1212.5226, submitted to ApJ Suppl.

[42] Toki, Y., Kitamura, T., Asada, H., Abe, F., 2011, ApJ, 740, 121; Nakajima, K. Asada, H. 2012, Phys. Rev. D, 85, 107501.

[43] Fukugita, M., and Peebles, P.J.E. 2004, ApJ, 616, 643.

[44] H. Erdl and P. Schneider, A&A 268, 453 (1993).

[45] S.M. Kopeikin and G. Schäfer, Phys. Rev. D 60, 124002 (1999).

[46] B. Paczynski, ApJ 304, 1 (1986).

[47] R.D. Blandford and R. Narayan, ApJ 310, 568 (1986).

[48] H.J. Witt, A&A 236, 311 (1990).

[49] P. Schneider, J. Ehlers and E.E. Falco, "Gravitational Lenses", Springer-Verlag (1992).

[50] M. Dominik, A&A 349, 108 (1999).

[51] V. Bozza, A&A 348, 311 (1999).

[52] V. Bozza, A&A 355, 423 (2000).

[53] V. Bozza, A&A 359, 1 (2000).

[54] J.H. An, MNRAS 356, 1409 (2005).

[55] C. Han, ApJ 638, 1080 (2006).

[56] S.-J. Chung and C.-U. Lee, MNRAS 411, 151 (2011).

[57] K. Griest and N. Safizadeh, ApJ 500, 37 (1998).

[58] A.O. Petters, H. Levine, and J. Wambsganss, "Singularity Theory and Gravitational Lensing", Birkäuser, (2001).

[59] R. Takahashi and H. Asada, ApJ 768, L16 (2013).

[60] R. Gavazzi et al., ApJ, 667, 176 (2007).

[61] H. Hoekstra and B. Jain, Annual Review of Nuclear and Particle Science, 58, 99 (2008).

[62] H. Hoekstra et al., Space Sci. Rev., 177, 75 (2013).

[63] S. Hilbert, J. Hartlap, S.D. White, and P. Schneider, A&A 449, 31 (2009).

[64] M. Kiblinger, Rep. Prog. Phys. 78, 086901 (2015).

[65] D. Jeong and F. Schmidt, Class. Quant. Grav. 32, 044001 (2015).

[66] H. G. Ellis, J. Math. Phys. 14, 104 (1973).

[67] M. S. Morris and K. S. Thorne, Am. J. Phys. 56, 395 (1988); M. S. Morris, K. S. Thorne, and U. Yurtsever, Phys. Rev. Lett. 61, 1446 (1988).

[68] N. M. Garcia and F.S.N. Lobo, Class. and Quant. Grav. 28, 085018 (2011); M. G. Richarte, Phys. Rev. D 87, 067503 (2013); T. Harko et al., Phys. Rev. D 87, 067504 (2013); M.R. Mehdizadeh, M.K. Zangeneh, and F.S.N. Lobo, Phys. Rev. D 91, 084004 (2015); F. Duplessis and D.A. Easson, Phys. Rev. D 92, 043516 (2015).

[69] H. Asada and M. Kasai, Prog. Theor. Phys. 104, 95 (2000).

[70] K. Chang and S. Refsdal, Nature 282, 561 (1979); A&A 132, 168 (1984).

[71] H. Maeda, Phys. Rev. D 79, 024030 (2009).

[72] H. Erdl and P. Schneider, A&A 268, 453 (1993).

[73] H.J. Witt, S. Mao, ApJ 447, L105 (1995).

[74] H. Asada , A&A 390, L11 (2002).

[75] G. Orban de Xivry and P. Marshall, MNRAS 399, 2 (2009).

[76] S.M. Kopeikin and G. Schäfer, Phys. Rev. D 60, 124002 (1999).

[77] N.W. Evans and M.I. Wilkinson, MNRAS 296, 800 (1998).

[78] M.C. Werner, J. An and N.W. Evans, MNRAS 391, 668 (2008).

[79] T.E. Collett and D.J. Bacon, arXiv:1510.00242.